



TECHNISCHE
UNIVERSITÄT
WIEN



MEDIZINISCHE
UNIVERSITÄT WIEN

DIPLOMARBEIT

The influence of palmitoylation on protein interaction: Investigating monoamine neurotransmitter transporters with molecular dynamics simulations

zur Erlangung des akademischen Grades

Diplom-Ingenieur

im Rahmen des Studiums

Biomedical Engineering

eingereicht von

Robert Spornraft, B.Eng.

Matrikelnummer 12227634

ausgeführt am Institut für Angewandte Physik der Fakultät für Physik der Technischen Universität Wien, in Zusammenarbeit mit dem Institut für Pharmakologie der Medizinischen Universität Wien

unter der Anleitung von
Univ.Prof. Dipl.-Ing. Dr. techn. Gerhard Schütz
Assoc.-Prof. Dr. rer. nat. Thomas Stockner

Wien, 03.02.2026

(Unterschrift Verfasser)

(Unterschrift Betreuer)

Kurzfassung

Monoamin Neurotransmitter Transporter (MATs) prägen die synaptische Signalübertragung, indem sie Dopamin, Noradrenalin und Serotonin aus dem extrazellulären Raum entfernen. Palmitoylierung kann die MAT-Funktion modulieren, unter anderem durch eine erhöhte Transportkapazität des Dopamintransporters (DAT). Zudem wurden MATs als Dimere und Oligomere beschrieben. Ein möglicher Zusammenhang ergibt sich daraus, dass die Haupt-Palmitoylierungsstelle des DAT in unmittelbarer Nähe von TM12 liegt, einer Transmembranhelix, die wiederholt als Bestandteil von MAT-Dimerinterfaces beschrieben wurde. Diese Arbeit untersucht, ob Palmitoylierung die Dimerisierung und Interface-Präferenzen des Noradrenalintransporters (NET) und des DAT verändert und wie die Membranzusammensetzung diese Effekte beeinflusst. Dazu wurden coarse-grained Molecular Dynamics MARTINI3 Simulationen von palmitoylierten und nicht-palmitoylierten NET- und DAT-Dimeren durchgeführt, ausgehend von einer durch Kryoelektronenmikroskopie (cryo-EM) entdeckten NET-Dimergeometrie in mehreren Membranmodellen. Die Dimerstabilität und Interfaces wurden mittels RMSD, 2D-Aufenthaltsdichtekarten, Analyse von Helix-Helix-Kontakten transmembraner Segmente sowie Lipidkontakt-Statistiken in der Nähe der Palmitoylierungsregion quantifiziert.

Die cryo-EM-abgeleitete Dimeranordnung war nach Aufhebung der Restraints in allen Membranmodellen instabil, was darauf hinweist, dass diese Geometrie im vorliegenden coarse-grained Setup nicht begünstigt ist. Stattdessen bildeten sich reproduzierbar alternative metastabile Dimere, deren Interfaces durch die Scaffold-Domänen-Helices und insbesondere TM12 gebildet wurden. Palmitoylierung stabilisierte die Dimere nicht generell, verschob jedoch die Verteilung der Interface-Populationen. TM12-beteiligte Interfaces nahmen bei NET zu und wurden über Replikate hinweg häufig reproduzierbarer, während DAT nach Palmitoylierung gegenteilige TM12-assozierte Trends und eine erhöhte Variabilität zeigte. Insgesamt stützen die Ergebnisse die Auffassung, dass die MAT-Dimerisierung ein Ensemble membranabhängiger Interface-Zustände darstellt, welche durch Palmitoylierung umgeformt werden kann, anstatt in einer einzelnen, stabilen Dimergeometrie vorzuliegen.

Abstract

Monoamine neurotransmitter transporters (MATs) shape synaptic signaling by clearing dopamine, norepinephrine, and serotonin from the extracellular space. Palmitoylation can modulate MAT function, including an increased transport capacity of the dopamine transporter (DAT). In parallel, MATs have been reported to form dimers and oligomers. A potential mechanistic link is suggested by the major DAT palmitoylation site being proximal to TM12, a transmembrane helix that has been repeatedly described in MAT dimer interfaces. This thesis tests whether palmitoylation alters dimerization and interface preferences of the norepinephrine transporter (NET) and DAT, and how membrane composition modulates these effects. Coarse-grained MARTINI3 molecular dynamics simulations of palmitoylated and non-palmitoylated NET and DAT dimers were initiated from a cryo electron microscopy (cryo-EM) derived NET-dimer geometry across multiple membrane models. Dimer stability and interfaces were quantified using RMSD, 2D occupancy density maps, transmembrane helix-helix contact analysis, and lipid-contact statistics near the palmitoylation region.

The cryo-EM-derived dimer arrangement was unstable after release of restraints in all membrane models, indicating this geometry is not favorable within the present coarse-grained setup. Alternative metastable dimers reproducibly formed, with interfaces enriched in scaffold-domain helices and especially TM12. Palmitoylation did not generically stabilize the dimers but shifted the interface populations. TM12-involving interfaces increased for NET and often became more reproducible across replicas, whereas DAT showed opposite TM12-associated trends and increased variability upon palmitoylation. Overall, the results support MAT dimerization as an ensemble of membrane-dependent interface states that can be reshaped by palmitoylation rather than stabilized into a single dominant dimer.

Eidesstaatliche Erklärung

Ich erkläre an Eides statt, dass die vorliegende Arbeit nach den anerkannten Grundsätzen für wissenschaftliche Abhandlungen von mir selbstständig erstellt wurde. Alle verwendeten Hilfsmittel, insbesondere die zugrunde gelegte Literatur, sind in dieser Arbeit genannt und aufgelistet. Die aus den Quellen wörtlich entnommenen Stellen, sind als solche kenntlich gemacht. Das Thema dieser Arbeit wurde von mir bisher weder im In- noch Ausland einer Beurteilerin/einem Beurteiler zur Begutachtung in irgendeiner Form als Prüfungsarbeit vorgelegt. Diese Arbeit stimmt mit der von den Begutachterinnen/Begutachtern beurteilten Arbeit überein.

Wien, 03.02.2026

Danksagung

Mit dieser Arbeit endet ein Lebensabschnitt, in welchem ich die Möglichkeit hatte, fachlich und persönlich zu reifen.

Einen besonderen Dank möchte ich meinen Eltern Silvia und Anton aussprechen. Ohne eure Unterstützung und Motivation würde ich heute nicht an diesem Punkt stehen. Auch meinen Geschwistern Bernhard und Daniela habe ich zu danken für viele Ratschläge und die Vorbildfunktion.

Zudem gebührt mein Dank Prof. Thomas Stockner und Prof. Gerhard Schütz für die Supervision. Ihre fachlichen Anregungen und konstruktive Kritik bei der Erstellung dieser Arbeit haben mir sehr geholfen.

Ich danke meinen Kolleginnen und Kollegen vom Computational Pharmacology Lab für die angenehme Arbeitsatmosphäre. Insbesondere danke ich Mounaf Al Makhlof für vertiefende Anstöße und lebhaftige Diskussionen, die mein Tagesgeschäft definitiv bereichert haben.

Ebenso würdigen will ich Ligia Zivkovic, Nadine Eichhorn, Mitar Bursać und Julius Fröhlich. Ohne die gegenseitige Unterstützung und Bibliotheksschichten mit Tischtennispausen wäre die Zeit an der TU Wien eine längere und unerfreulichere gewesen.

Zu guter letzt danke ich Dafina Thaqi für die moralische Unterstützung und stetige Erinnerung daran, dass auch Erholung zur Produktivität mitwirkt.

Contents

1. Introduction	1
2. Theoretical Background	3
2.1. Palmitoylation	3
2.1.1. Physiological and pathological impact of palmitoylation . . .	5
2.2. Monoaminetransporters	8
2.2.1. Structural aspects and basic function	8
2.2.2. Palmitoylation of Monoaminetransporters	10
2.2.3. Oligomerization of Monoaminetransporters	11
2.3. Molecular Dynamics Simulations	13
2.3.1. Coarse-grained molecular dynamics and the MARTINI force field	15
3. Methods	18
3.1. System setup and simulation design	18
3.2. Simulation protocol and parameters	21
3.3. Data Analysis	23
3.3.1. Root mean square deviation measurements	24
3.3.2. Density maps	24
3.3.3. Transmembranelix contact measurements	25
3.3.4. Lipid contact analysis at the palmitoylation site	25
4. Results	27
4.1. Root mean square deviation time series	27
4.2. Density maps of molecules of interest	31
4.3. Transmembranelix contact analysis	34
4.4. Lipid contacts with palmitoylation site	38
5. Discussion	40
5.1. Instability of the cryo-EM-derived dimer arrangement in MARTINI3	40
5.2. Alternative interface populations and membrane-composition de- pendence	41
5.3. Palmitoylation effects on interface preferences	43
5.4. General limitations in the study design and analysis methods	44

6. Conclusion	47
Bibliography	49
List of Figures	59
List of Tables	61
A. Appendix	62

1. Introduction

Communication between neurons is accomplished by neurotransmitters, which are released into the synaptic cleft and activate receptors on target cells. Efficient signaling therefore requires not only neurotransmitter release, but also rapid clearance mechanisms that terminate the signal. In monoaminergic neurons, this role is primarily fulfilled by the monoamine transporters (MATs), which include the dopamine transporter (DAT), norepinephrine transporter (NET), and serotonin transporter (SERT) [1]. Because MATs strongly shape extracellular monoamine levels, changes in transporter expression, regulation, or kinetics can contribute to disease-relevant phenotypes. Dysregulation of MATs has been implicated in neuropsychiatric disorders such as attention deficit hyperactivity disorder (ADHD) and depression, as well as in several neurodegenerative diseases [2].

Post-translational modifications are key regulators of MAT localization, turnover, and function [3]. Among these, palmitoylation, the reversible attachment of a palmitate chain to cysteine residues, has gained attention as a lipid modification that can tune transporter behavior [4, 5]. Recent work demonstrates that MATs are palmitoylated, yet the physiological role of this modification remains incompletely understood [6–8]. Functionally, DAT palmitoylation has been linked to transport kinetics, as increased palmitoylation has been associated with a higher maximal uptake velocity (V_{\max}) [6, 9].

In parallel, MATs have repeatedly been observed as dimers and higher-order oligomers in cellular experiments [10]. In addition, DAT oligomerization has been discussed as a potential therapeutic target in the context of cocaine addiction [11]. For many years, however, high-resolution structures of MAT oligomers remained absent, and most available structures and structural models were interpreted in a monomeric setting [12]. Recently, cryo electron microscopy (cryo-EM) provided direct structural evidence for a NET dimer interface that is mediated predominantly by cholesterol as well as phosphatidylinositol (PI) and phosphatidylinositol 4,5-bisphosphate (PIP₂) molecules [13]. This raises the possibility that SERT and DAT, which are highly similar in structure and sequence [14, 15] and have been observed as oligomers, yet not structurally resolved at high resolution, could also adopt the same lipid-mediated arrangement.

A key open question is whether MAT oligomerization serves a distinct biological function. Literature suggests that monomeric and oligomeric transporter populations may differ in functional properties, and that oligomerization could modulate

substrate transport and/or regulatory processes [10, 13, 16]. Computational work further supports a mechanistic link between oligomer geometry and transporter dynamics. Large-scale oligomerization simulations for DAT indicate that the bundle domain (which undergoes major conformational changes during transport) is generally avoided at dimerization interfaces, consistent with the idea that interface geometry can influence the conformational freedom required for transport [17].

Several independent observations show transmembrane helix (TM)12 as a recurring interaction surface in related transporters: leucine transporter (LeuT) crystal structures present a symmetric interface involving TM12, and self-assembly studies for DAT and SERT report possible dimer interfaces that can include TM12 [18–20]. Moreover, DAT’s major palmitoylation site is described at a site near TM12 (Cys581 in human DAT), positioning the palmitoyl chain in the immediate proximity of a helix that is frequently implicated in oligomer interfaces [9].

Central hypothesis and aim of this work. Together, these findings motivate the central hypothesis of this thesis: palmitoylation could shift MAT dimerization strength and/or interface preferences, potentially contributing to the altered transport properties observed for palmitoylated DAT (including increased V_{\max}).

The aim of this work is to investigate how palmitoylation affects dimerization of NET and DAT, and how this relationship depends on membrane composition. To access the long timescales and sampling required for dimer ensembles, coarse-grained molecular dynamics (MD) simulations are performed using the MARTINI3 force field. Different membrane models are used to probe membrane-dependent effects and to approximate more physiological conditions.

By starting from the mentioned cryo-EM resolved NET dimer arrangement and characterizing the dimer stability and interface, this thesis seeks to clarify whether palmitoylation reshapes MAT interface populations and whether this could help explain why MATs are palmitoylated and why they form oligomers in membranes. Compared with recent studies on related questions [17, 19, 20], this work additionally considers complex membrane models, uses a cryo-EM-derived oligomer starting structure with stabilizing lipids, and applies the advanced MARTINI3 force field, thereby providing a complementary perspective on MAT palmitoylation and oligomerization.

2. Theoretical Background

2.1. Palmitoylation

A common post-translational modification of proteins includes lipidation, in which proteins are covalently linked to lipids, most commonly long-chain fatty acids (myristate, palmitate), but also cholesterol and phospholipids. Fatty-acylation is dominated by N-myristoylation and S-palmitoylation, while some proteins carry both. The processes and attachment sites are quite diverse, so each modification is installed by dedicated enzyme families that recognize the lipid type and the specific attachment site [21].

S-Palmitoylation is the covalent attachment of a 16-carbon palmitic acid to protein cysteine thiols through a thio-ester bond. Unlike other lipid modifications, the thio-ester bond can be cleaved, making it a reversible modification, as illustrated in Figure 2.1 [4, 21]. Due to poor fatty acid selectivity of the enzymatic process, it

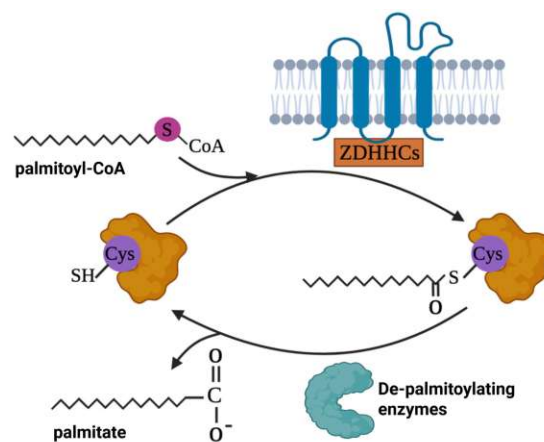


Figure 2.1.: The reversible palmitoylation cycle. Palmitoyl transferases (ZDHHCs) covalently link palmitoyl-CoA to cysteine residues of proteins, and the palmitate group is cleaved by de-palmitoylating enzymes. Adapted from [22] (Li, Zhang & Chen, *Cells* 2023, 12, 2209), CC BY 4.0 License.

is also referred to as S-Acylation [23, 24]. Less abundantly the palmitate is instead

attached to specific amino acids at the N-terminal (cysteine, lysine, glycine) via an amide bond (N-palmitoylation), as exemplified by Hedgehog proteins [21, 25]. In this work, the term palmitoylation will be used to describe the general process of S-acylation.

Protein palmitoylation is catalyzed by DHHC protein acyltransferases (PATs), a family of 23 human transmembrane enzymes characterized by a conserved Asp-His-His-Cys (DHHC) motif [26]. These enzymes are also referred to as ZDHHCs, reflecting the presence of two zinc ions in the active center, which are required for structural stability [27, 28]. DHHC enzymes localize predominantly to the Golgi apparatus and endoplasmic reticulum, with additional, though less abundant, localization at the plasma membrane, mitochondria, and perinuclear membrane regions [4].

The prevailing enzymatic model is a two-step, so-called ping-pong mechanism: the active-site cysteine first undergoes autoacylation by palmitoyl-CoA, followed by transfer of the palmitoyl chain to a cysteine residue within the substrate protein (Figure 2.2) [23]. Although this mechanism is generally supported, direct experimental evidence for autoacylation has not been demonstrated for all DHHC family members, including DHHC13, DHHC17, and DHHC19 [4].

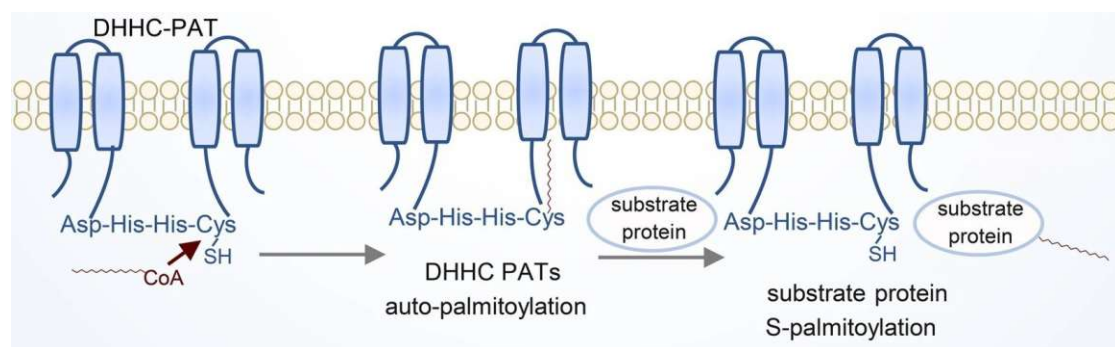


Figure 2.2.: Two-step ping-pong mechanism proposed for DHHC-mediated palmitoylation. First, the DHHC palmitoyl acyltransferase undergoes autopalmitoylation by transferring the palmitoyl group from palmitoyl-CoA to the cysteine in its active site with subsequent transfer of the palmitoyl group to the cysteine residue of the substrate protein. Adapted from [4] (Yuan et al., *Signal Transduction and Targeted Therapy* 2024, 9:60), CC BY 4.0 License.

Typically, palmitoylation is transient with a half-life in the range of hours due to the action of depalmitoylating enzymes that hydrolyze the thioester bond [29]. These enzymes are serine hydrolases and can be grouped into three major classes: acyl-protein thioesterases (APT1/2), palmitoyl-protein thioesterases (PPT1/2),

and members of the α/β -hydrolase domain family (ABHD10/12/17). They are substrate-specific and operate in different compartments. APTs are largely cytosolic or membrane-associated and undergo dynamic palmitoylation themselves, enabling cycling between the Golgi and cytosol, PPTs function within the lysosomal lumen and are primarily linked to protein degradation and ABHD proteins constitute a diverse group, with e.g. ABHD17A/B/C which are enriched at the plasma membrane or post-synaptic sites, where they mainly depalmitoylate membrane-associated proteins [4].

2.1.1. Physiological and pathological impact of palmitoylation

Palmitoylation has diverse consequences on proteins and membranes, which can be organized into three hierarchical tiers following Mesquita et al. [5]: primary effects, which act directly on the modified protein, secondary effects, which emerge from altered membrane partitioning or interaction profiles and tertiary effects, which follow as downstream cellular outcomes.

Primary effects. The covalent attachment of the hydrophobic palmitoyl chain directly increases membrane affinity (Figure 2.3a). Soluble proteins become membrane-tethered and transmembrane proteins experience repositioning of cytosolic domains toward the bilayer. Palmitoylation near or within transmembrane segments can alter lipid preference toward ordered, cholesterol- and sphingolipid-rich nanodomains. Secondly, palmitoylation may influence protein conformation (Figure 2.3b). The hydrophobic tail can tilt the whole protein or lead to structural adjustments of the protein or its transmembrane helices [5].

Secondary effects. These direct biophysical alterations cause proteins to diffuse into membrane regions of distinct thickness and curvature (Figure 2.3c). Also, protein-protein interaction profiles may change by modulating proximity and binding at the membrane interface (Figure 2.3d) [5].

Tertiary effects. As downstream consequences of these relocation and interaction changes, palmitoylation can bias vesicular trafficking and budding (Figure 2.3e), promote or destabilize multiprotein assemblies (Figure 2.3f), and ultimately activate or inhibit protein function (Figure 2.3g) [5]. Moreover, palmitoylation can affect protein turnover by altering stability and degradation rates [4].

Palmitoylation therefore represents a versatile regulatory mechanism capable of modifying diverse cell-physiological functions. Dysregulation of this process con-

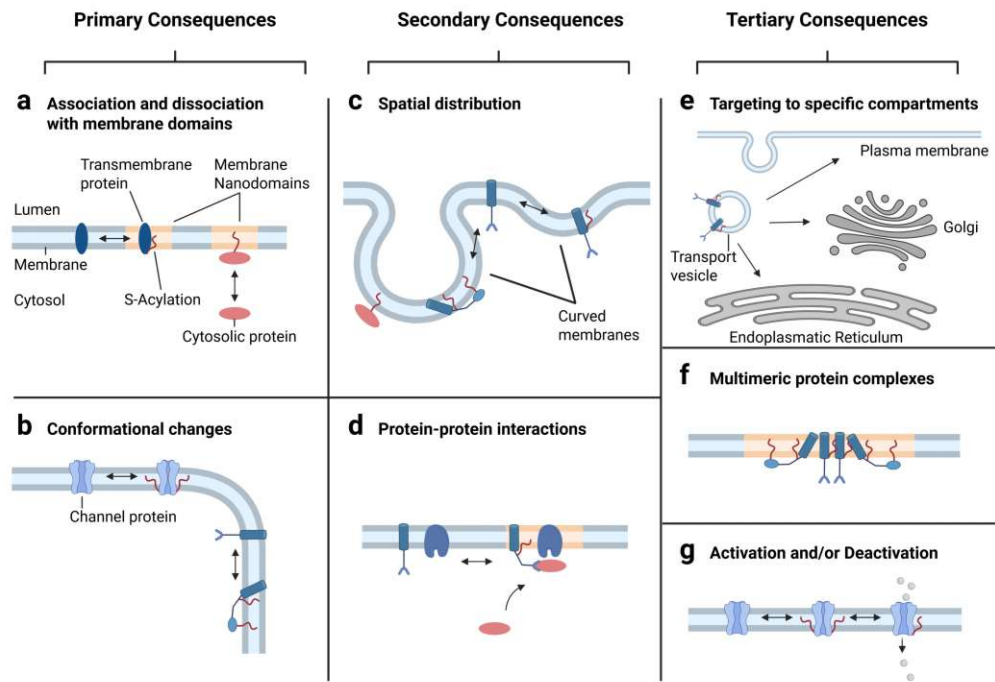


Figure 2.3.: Consequences of palmitoylation summarized in three hierarchical tiers (primary, secondary, tertiary). (a) Palmitoylation can target transmembrane proteins to specific membrane domains and recruit soluble cytosolic proteins to membranes and/or nanodomains. (b) Palmitoylation may induce conformational changes or alter protein tilt in the membrane. (c,d) These primary effects can promote localization to regions of different membrane curvature (c) and modulate protein-protein interactions via altered proximity and/or conformation (d). (e-g) Downstream consequences include changes in vesicular trafficking and subcellular localization (e), assembly into multimeric complexes (f), and modulation of protein activity and function (g). Figure recreated with BioRender based on [5].

tributes to a broad spectrum of pathological states, many of which have now been identified [4, 22, 30, 31]. A strong association exists between palmitoylation and tumor biology. In a recent proteomic analysis of 299 tumor-driving proteins in humans, 132 were found to be palmitoylated [32]. Palmitoylation can either promote or suppress tumor progression. Many oncogenic proteins depend on palmitoylation for proper trafficking and plasma membrane localisation, whereas in other contexts palmitoylation activates tumor-suppressive signaling pathways or inhibits oncogenic ones. Tumors in which palmitoylation exerts a suppressive function often exhibit a dysfunctional palmitoylation machinery [4]. Palmitoylation also plays a crucial role in neurobiology. In Alzheimer's disease, both the neurotoxic β -amyloid aggregation and the formation of intracellular neurofibrillary tangles are linked to dysregulated palmitoylation, representing two major pathological hallmarks of the disease [31, 33, 34]. In Huntington's disease, mutant huntingtin exhibits reduced palmitoylation and increased toxicity [31, 35]. For schizophrenia, reduced protein palmitoylation has been reported in the dorsolateral prefrontal cortex of affected individuals [31, 36]. Variants in the zDHHC8 gene have been associated with alterations in cortical volume, and additional palmitoylating enzymes have been implicated, although their mechanistic contributions remain insufficiently explored [31, 37]. In ADHD, dopamine imbalance is central to disease etiology. Two key regulators of dopaminergic homeostasis, the DAT and certain dopamine receptors are palmitoylated [31, 38]. For DAT, studies reported palmitoylation increases V_{\max} and enhances transporter stability by reducing degradation [6, 9]. Furthermore, knockout of zDHHC15 in mice lead to increased novelty-induced locomotion, a phenotype that similar to ADHD-like behaviors. The findings suggest that impaired dopamine reuptake underlies the observed behavior, providing strong in vivo support for palmitoylation-dependent regulation of dopamine homeostasis [39]. In cardiac physiology, palmitoylation modulates ion channel function and thereby influences excitability of cardiomyocytes. For instance, palmitoylation of the voltage-gated sodium channel Nav1.5 enhances cardiac excitability and may predispose to arrhythmia [4]. Palmitoylation also contributes to the pathogenesis of certain infectious diseases. The SARS-CoV-2 spike protein, a trimer which contains ten palmitoylation sites per protomer, shows increased fusogenicity when palmitoylated and therefore enhanced infectivity [40].

The variety of palmitoylation-associated diseases emphasizes the importance of exploring the underlying mechanisms and functional consequences of this modification. Potential therapeutic strategies may involve enhancing PAT activity or inhibiting depalmitoylases, while improved understanding could also support the development of diagnostic biomarkers across diverse pathological contexts.

2.2. Monoaminetransporters

MATs are members of the solute carrier 6 (SLC6) family of neurotransmitter sodium symporters and comprise **NET**, **DAT**, and **SERT**. They are integral membrane proteins localized to the plasma membrane of monoaminergic neurons and serve the primary function of terminating neurotransmission by reuptaking dopamine, norepinephrine, and serotonin from the synaptic cleft into the presynaptic neuron, where the neurotransmitters are either recycled or degraded [1].

The physiological relevance of MATs lies in their role as key regulators of both the signal amplitude and duration of monoaminergic neurotransmission. Through this function, they critically influence a wide range of central and sympathetic nervous system processes, including attention, sleep, learning, mood, and reward [2, 41]. In addition, MATs are targets of psychostimulants and drugs of abuse such as cocaine, methamphetamine, and 3,4-methylenedioxymethamphetamine (MDMA), which block or reverse neurotransmitter transport and thereby increase synaptic monoamine levels, resulting in stimulatory effects [41]. Dysregulation of transporter expression or function has been implicated in numerous neuropsychiatric and neurodegenerative disorders, including depression, anxiety disorders, ADHD, addiction, and several neurodegenerative diseases [2].

2.2.1. Structural aspects and basic function

From a structural perspective, all MATs share a conserved core architecture composed of twelve hydrophobic α -helical TM segments, as schematically shown in Figure 2.4a. Both the N- and C-termini extend largely into the cytosol and represent the most divergent regions among MATs, whereas the remaining structural elements are highly conserved across DAT, NET, and SERT [41, 42].

A distinguished structural motif of MATs is the so-called LeuT fold, named after the bacterial leucine transporter LeuT, whose crystal structure was the first to reveal this conserved architecture among secondary active transporters. The LeuT fold comprises ten TM helices (TM1-TM10) arranged as five pairs of inverted repeats with respect to the membrane plane [45]. These helices are functionally subdivided into two major domains: the larger scaffold domain (TM3, TM4, TM5, TM8, TM9, and TM10), which fixes the transporter within the membrane, and the bundle domain (TM1, TM2, TM6, and TM7), which moves around the scaffold domain during substrate transport [16, 46]. Figure 2.4b shows a 3D representation of outward-open NET from extracellular view, with Figure 2.4c details the respective TM helices of scaffold and bundle domain.

Within the bundle domain, TM1 and TM6 contain conserved unwound segments at their midpoint, further subdividing them to subhelices TM1a/TM1b and TM6a/TM6b [42]. These structural disruptions are functionally critical: together

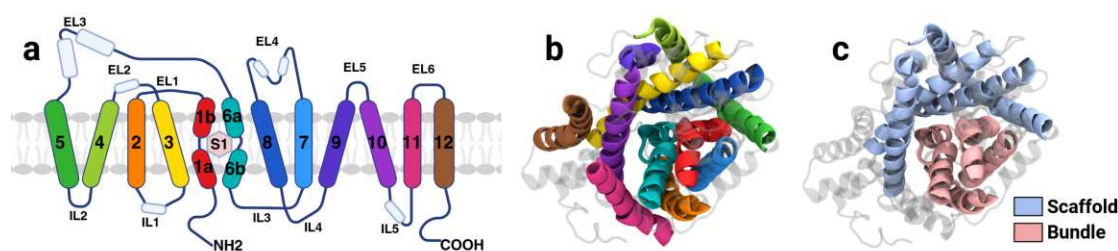


Figure 2.4.: Schematic topology and representative 3D structure of monoamine transporters (MATs), shown from an extracellular viewpoint (example: NET). (a) Topological diagram of the conserved 12 transmembrane helices (TM1-TM12) shared by SLC6 MATs, including the central substrate-binding site (S1) and intra- and extracellular loops (IL/EL). Recreated with BioRender based on Ref. [43]. (b,c) 3D representation of NET derived from PDB 8YR2 [44]: top view with TM helices colored according to the topology scheme (b) or according to bundle versus scaffold domain assignment (c).

with TM3 and TM8, they form the primary substrate-binding site (S1), which is located approximately halfway across the membrane. The remaining helices, TM11 and TM12, are positioned peripherally to the LeuT fold [2, 42]. These peripheral helices have been implicated in intermolecular interactions and oligomer formation, with a characteristic kink in TM12 representing a distinct feature from the LeuT structure [10, 42].

Human DAT, NET, and SERT consist of approximately 600-630 amino acids with high sequence conservation. DAT and NET are the most closely related, sharing roughly 80% amino acid identity, whereas DAT and SERT exhibit lower similarity, with approximately 52% identity within the transmembrane core. In contrast, the cytosolic N- and C-terminal regions show markedly reduced conservation, with sequence identities of about 17% and 27%, respectively [14, 15].

Functionally, MATs operate as secondary active symporters, coupling neurotransmitter uptake to the electrochemical gradients of sodium and chloride ions across the plasma membrane [2]. The transport is not directly ATP-driven, however, it depends indirectly on ATP through the activity of the Na^+/K^+ -ATPase, which maintains the transmembrane sodium gradient required for transporter function [47]. All MATs bind and co-transport at least one Na^+ and one Cl^- ion, and are therefore commonly referred to as Na^+/Cl^- -dependent symporters [41].

The substrate transport follows an alternating-access mechanism [42]. In the outward-facing open conformation, which represents the predominant resting state, the transporter exposes the S1 site to the extracellular space, allowing binding of

ions and substrate. Subsequent ligand binding induces a conformational transition to an occluded state, in which substrate and ions are shielded from both sides of the membrane. This is followed by a transition to the inward-facing open state, enabling release of substrate and ions into the cytoplasm. Upon dissociation, the transporter resets to the outward-facing conformation, completing the transport cycle. This mechanism ensures efficient neurotransmitter uptake while preventing uncontrolled ion or substrate leakage across the membrane [42].

2.2.2. Palmitoylation of Monoaminetransporters

In Section 2.1, the post-translational modification palmitoylation was introduced. Notably, all three monoamine transporters DAT, NET, and SERT have been shown to undergo palmitoylation, although at distinct sites and with transporter specific functional consequences [6–8].

In the case of DAT, palmitoylation has been demonstrated in the kidney cell lines LLC-PK1 and HEK293 cells and in rat brain synaptosomes [6, 9]. Mutation of Cys581 resulted in an approximately 60% reduction in overall palmitoylation, indicating that DAT contains multiple palmitoylation sites, with Cys581 representing the predominant site. Additional accessible cysteine residues include Cys6, Cys135, Cys342, and Cys523 [38]. Functionally, DAT palmitoylation enhances dopamine uptake capacity by increasing V_{\max} without altering transporter surface expression, indicating that DAT’s kinetics are regulated by palmitoylation [38]. Although the precise molecular basis remains unresolved, several hypotheses have been proposed. These include a reduction in hydrophobic mismatch through direct tilting of transmembrane segments or redistribution into lipid domains with a bilayer thickness better matched to the protein, as well as modulation of dimer formation, which may exhibit distinct transport characteristics or membrane localization preferences [38].

For SERT, palmitoylation has been shown in the same cell models (LLC-PK1/HEK293) [7, 48]. One study reported palmitoylation at Cys147 and Cys155 of immature SERT (prior to its delivery to the plasma membrane) [48]. The authors proposed that palmitoylation at these sites enhances SERT cell-surface expression by inducing conformational changes in transmembrane helices TM2 and TM3, thereby improving endoplasmic reticulum export and promoting proper protein folding. Interestingly, the study found that mutation only of Cys147 led to a reduction in V_{\max} without a corresponding decrease in cell-surface expression of SERT [48], while another study reported the same effect by inhibiting PATs [7]. Together, these findings indicate a direct kinetic effect of palmitoylation on SERT function, independent of changes in transporter abundance at the plasma membrane [7, 48].

Regarding the palmitoylation of NET, a recent study found the modification

also in rat brain synaptosomes and in the previously mentioned cell lines (LLC-PK1/HEK293) [8]. Using cysteine mutagenesis, Cys44 was identified as a palmitoylation site. In contrast to DAT and SERT, inhibition of palmitoylation reduced total NET surface expression but did not affect V_{\max} , indicating that palmitoylation primarily regulates NET trafficking rather than transport kinetics [8].

Taken together, these findings demonstrate that although palmitoylation modulates monoamine transporter function, it does so in a transporter-specific manner. DAT and SERT exhibit palmitoylation-dependent changes in V_{\max} , whereas NET primarily shows altered trafficking and surface expression without kinetic modulation. These differences likely arise from variation in the number and location of palmitoylation sites, the specific DHHC enzymes involved, and the subcellular context in which palmitoylation occurs [8]. Moreover, palmitoylation may exert distinct effects at different maturation stages of MATs, as suggested for immature SERT [48].

2.2.3. Oligomerization of Monoaminetransporters

The formation of quaternary structures by transmembrane proteins is a well-established phenomenon [49]. Early studies already reported the presence of MATs in oligomeric assemblies [50, 51]. Since then, a wide range of biochemical, imaging-based, and computational approaches have been employed to characterize MAT oligomerization, as summarized in several comprehensive reviews [10, 16]. The current experimental evidence for oligomerization of SERT, DAT and NET is briefly outlined below.

For SERT, multiple oligomeric states have been reported, including monomers, dimers, tetramers in the form of pairs of dimers, and pentamers [10]. Anderluh et al. utilized the thinning out clusters while conserving stoichiometry of labeling (TOCCSL) method, a single-molecule brightness analysis technique that enables quantification of labeled protein densities below the optical resolution limit [52]. Using this approach, the authors observed a decreasing abundance with increasing oligomeric order. Elevated SERT expression levels were associated with increased oligomerization in the endoplasmic reticulum, while oligomer levels at the plasma membrane remained largely unaffected [16, 53]. Consistent with these findings, a molecular dynamics self-assembly study demonstrated that SERT is capable of forming dimers and higher-order oligomers in a membrane environment. Several preferred dimer interfaces were identified, including a particularly stable symmetric dimer involving TM12 [10, 19].

Similar to SERT, DAT has been reported to exist in multiple oligomeric states, including monomers, dimers, and tetramers [10]. Using the TOCCSL approach, Das et al. quantified approximately 55% monomeric and 35% dimeric DAT populations, with a smaller fraction of higher-order oligomers. Importantly, DAT

dimers were shown to be stable over timescales of several minutes, indicating that oligomerization is not a transient phenomenon [10, 54].

For NET, Luethi et al. investigated oligomerization using the same TOCCSL methodology [55]. Their analysis revealed approximately 60% monomeric and 40% dimeric NET species. Their results indicated that the dimers are stable on the order of minutes, based on the observed exchange between molecules in monomeric and dimeric state [10]. More recently, strong structural evidence for NET oligomerization was provided by Zhang et al., who found high-resolution cryo-electron microscopy structures of NET homodimers in both apo and substrate-bound states [13]. These structures revealed symmetric dimers with PI, PIP₂, and cholesterol molecules located at the dimer interface, suggesting that these specific lipids contribute to stabilizing the oligomeric assembly [13].

Collectively, these studies demonstrate that MATs can form stable oligomeric assemblies under various experimental conditions. However, the functional consequences of oligomerization are not yet fully understood. Jayaraman et al. proposed that the specific location of the oligomer interface may critically influence transport activity [16]. Because substrate transport involves movement of the bundle domain relative to the scaffold domain, transport may be favored when oligomer interfaces are formed primarily through the scaffold domain, allowing the bundle domain to retain conformational freedom. Conversely, involvement of the bundle domain in oligomer interfaces could restrict conformational changes and impair transport efficiency [16]. Notably, the NET dimer interface resolved by cryo-EM consists exclusively of scaffold-domain helices, lending structural support to this hypothesis [13]. A schematic representation of the proposed relationship between oligomer interface location and transport dynamics is shown in Figure 2.5. Depending on the interface geometry, oligomerization may therefore either enhance or slow substrate transport [13, 16].

Despite these advances, cryo-EM structures of MAT oligomers are currently available only for NET. Consequently, the pathways and lipid environments controlling oligomer formation and its functional relevance across the MAT family remain incompletely understood. Further experimental and computational studies will be required to explain the mechanisms, regulation, and physiological consequences of MAT oligomerization.

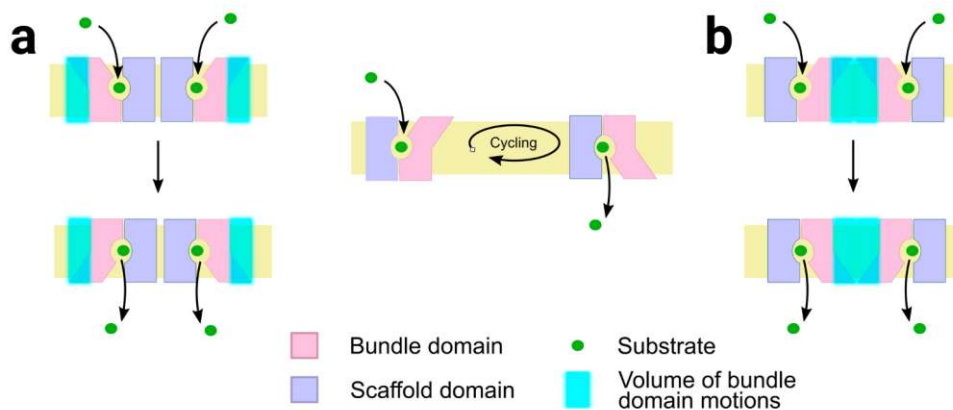


Figure 2.5.: Proposed influence of MAT oligomerization interfaces on substrate transport. The center illustrates the alternating-access mechanism, with the bundle domain moving relative to the scaffold domain. (a) Oligomerization within the scaffold domain allows bundle-domain motion. (b) Oligomerization within the bundle domain may oppose transport because additional energy is required to disrupt existing protomer interactions. Reproduced from [16] (Jayaraman et al., *Journal of Neurochemistry* 2021, 157:919-929), CC BY 4.0 License.

2.3. Molecular Dynamics Simulations

Certain scientific questions are difficult or impossible to answer by using experimental techniques alone, due to limitations in spatial or temporal resolution, the impracticality of performing the required number of repetitions for statistical significance, or the inherently non-physiological nature of the experimental setup. To overcome these limitations in the life sciences, MD simulations have emerged as a powerful complementary approach.

MD simulations are a computational method used to study biological molecules by explicitly modeling the movement of their constituent atoms over time. They are widely used in biophysics, chemical physics, and materials science [56]. Most MD approaches rely on the Born-Oppenheimer approximation, which assumes that atomic nuclei motions can be treated independently of the electrons, allowing the **potential energy** of the system to be expressed solely as a function of the nuclear coordinates [57]. Within this framework, nuclei are treated as classical particles that move according to Newton's equations of motion under forces derived from the gradient of the potential energy function [58, 59].

Direct quantum mechanical evaluation of the electronic potential energy sur-

face at every simulation step is computationally too expensive, especially for large biomolecular systems. Instead, molecular mechanics force fields are employed as empirical approximations of the potential energy function, enabling simulations on biologically relevant length and time scales [58]. Their specific force-field parameters are typically derived from experimental and quantum mechanical studies on small molecules of interest [60]. Most modern force fields describe the total potential energy as the sum of bonded and non-bonded interaction terms. While more advanced force fields may include additional terms, these core components form the basis of most MD simulations [58].

The total potential energy \mathcal{V} of the system can be expressed as [58, 60]:

$$\mathcal{V} = \underbrace{\sum_{\text{bonds}} \frac{k_b}{2} (l_i - l_{i,0})^2 + \sum_{\text{angles}} \frac{k_\theta}{2} (\theta_i - \theta_{i,0})^2 + \sum_{\text{torsions}} \frac{V_n}{2} (1 + \cos(n\omega - \gamma))}_{\text{bonded interactions}} + \underbrace{\sum_{\text{non-bonded pairs } ij} \left(4\varepsilon_{ij} \left[\left(\frac{\sigma_{ij}}{r_{ij}} \right)^{12} - \left(\frac{\sigma_{ij}}{r_{ij}} \right)^6 \right] + \frac{q_i q_j}{4\pi\varepsilon_0 r_{ij}} \right)}_{\text{non-bonded interactions}} \quad (2.1)$$

The bonded interaction terms account for deviations of bond lengths l_i from their equilibrium values $l_{i,0}$ and bond angles θ_i from reference angles $\theta_{i,0}$, both modeled using harmonic potentials. Torsional interactions describe rotation about bonds and are represented by a cosine series, where ω denotes the dihedral angle, n the multiplicity, and γ the phase shift. The non-bonded interactions comprise van der Waals forces, modeled using a Lennard-Jones potential with parameters σ_{ij} and ε_{ij} , and electrostatic interactions described by a Coulomb potential, scaled by the partial charges q_i and q_j of the interacting atoms. The force constants k_b , k_θ , and V_n define the stiffness of the respective interactions [58, 60].

Once the potential energy function is defined, forces acting on each atom are obtained as the negative gradient of \mathcal{V} with respect to atomic positions [60]. These forces are then used to numerically integrate Newton's equations of motion, yielding updated atomic positions and velocities at each time step. Repeated evaluation of forces and integration over time results in a continuous trajectory, representing the dynamical evolution of the simulated system [58]. A schematic overview of a basic MD simulation workflow is shown in Figure 2.6 [61].

Because simulations are necessarily performed on finite systems (the simulation box), boundary effects must be carefully addressed. To avoid artificial surface artifacts, periodic boundary conditions (PBCs) are commonly applied, in which the simulation box is replicated in all directions, allowing particles that exit one side of the box to re-enter from the opposite side [60].

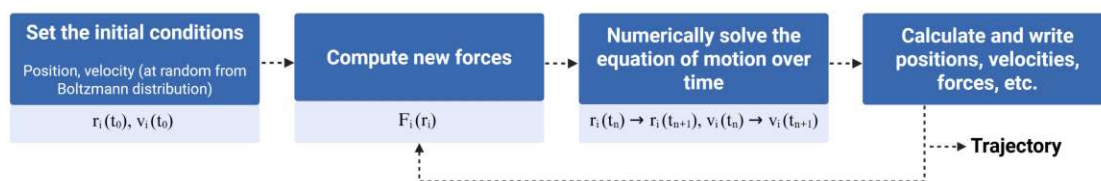


Figure 2.6.: Flowchart of a basic molecular dynamics (MD) simulation algorithm. Abbreviations: time (t), position (\mathbf{r}), velocity (\mathbf{v}), and force (\mathbf{F}). Figure recreated based on [61].

For protein or enzyme simulations, initial coordinates are typically obtained from experimentally determined structures deposited in the Protein Data Bank (PDB) [62]. These structures are embedded in an environment that reflects the biological context of interest, such as aqueous solvent or lipid membranes [60, 61]. Since experimentally derived structures are generally not in thermodynamic equilibrium under simulation conditions, a standard simulation protocol involves several preparatory steps. First, energy minimization is performed to relieve unfavorable steric contacts and bring the system to a local minimum on the potential energy surface. This is commonly achieved using steepest descent algorithms that follow the energy gradient with respect to atomic positions [60].

Subsequently, the system is gradually heated by assigning velocities consistent with increasing temperatures until the desired target temperature is reached. This is followed by an equilibration phase, during which the system evolves under controlled temperature and pressure conditions, typically using the isothermal-isobaric (NPT) ensemble, to allow system stabilization and redistribution of kinetic and potential energy [60]. Finally, a production phase is conducted, during which trajectories are recorded and considered suitable for data analysis [63].

2.3.1. Coarse-grained molecular dynamics and the MARTINI force field

In the previous section, MD simulations were introduced for systems in which atoms interact via a molecular mechanics potential. The same fundamental principles, however, apply to any system of interacting particles: as long as a potential energy function is defined, particle motion can be propagated by numerically integrating Newton's equations of motion. coarse-graining (CG) exploits this concept by replacing groups of atoms with effective interaction sites, thereby enabling simulations on extended spatial and temporal scales, as outlined below.

The primary motivation for employing coarse-grained models lies in practical

considerations. Atomistic molecular dynamics simulations suffer from high computational cost, as all bonded and non-bonded interactions must be evaluated at every integration step. This rapidly becomes a limiting factor for large systems or long simulation times. CG approaches can reduce the computational cost by two to three orders of magnitude relative to atomistic simulations, while keeping sufficient reliability [64]. The central idea of CG is to reduce the number of particles by grouping multiple atoms into single beads. Interactions between these beads are described by effective potentials that are parameterized to reproduce the structural and thermodynamic of the underlying atomistic system [65]. In its simplest form, the numerical integration scheme remains unchanged from atomistic MD as described in the previous section. However, beads rather than atoms serve as the interacting particles, and the interaction parameters are adapted accordingly [66]. In addition to the reduced particle number, CG models exhibit a smoother potential energy surface, which permits the use of larger integration time steps compared to atomistic simulations. This further extends the accessible simulation timescales and enables the study of slower processes at longer timescales [65]. The inherent trade-off of CG is (besides the smoother energy surface) the loss of atomistic detail, as motions within a bead are no longer resolved. Consequently, the choice between atomistic and CG simulations strongly depends on the specific research question being addressed [64].

For simulations of biological systems, the MARTINI force field [67] has evolved to the most popular [64]. The original force field uses 18 different bead types, which are categorized into charged, polar, nonpolar and apolar beads [64]. MARTINI usually follows a 4-to-1 mapping scheme, in which approximately four heavy atoms with their associated hydrogens are represented by one bead of the same size (regular) [67]. In the newest version, MARTINI3, the bead repertoire has been expanded to include small and tiny beads, enabling improved representation of the biophysical properties of aromatic structures or nucleotides [68]. An example of the mapping of an all-atomistic cholesterol to its corresponding MARTINI3 CG representation is shown in Figure 2.7.

Regarding the potential energy function within MARTINI, non-bonded interactions are modeled using Lennard-Jones potentials with bead-type-dependent interaction strengths, while electrostatic interactions are represented by a distance-dependent Coulomb potential. Bonded interactions are treated in a similar manner as in all-atomistic force fields [64]. A known challenge in CG protein simulations is the limited ability of the force field to preserve secondary and tertiary structure. To address this, elastic network models (ELNEDIN) [70] are commonly employed in MARTINI simulations to maintain the overall protein structure [64].

Together, these developments make coarse-grained molecular dynamics, particularly within the MARTINI framework, a powerful and accessible approach for

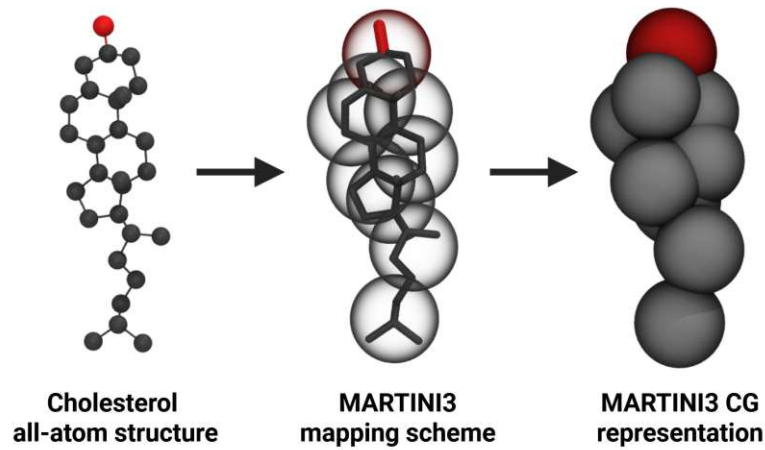


Figure 2.7.: MARTINI3 mapping scheme illustrated for cholesterol. The all-atom representation shows heavy atoms (carbon in black, oxygen in red). Applying the MARTINI3 4-to-1 mapping [69] yields the coarse-grained representation, with beads shown in the same color scheme (the ROH bead in red).

investigating large-scale, long-timescale phenomena in biomolecular systems.

3. Methods

This chapter describes the methodological workflow used to address the research question using a MD simulation pipeline. It covers (i) the system setup and the strategy to probe influential parameters by constructing different simulation systems, (ii) the simulation protocol and key parameters, and (iii) the trajectory analysis approach aimed at quantifying dimerization-related phenomena.

3.1. System setup and simulation design

As the starting structure for all NET simulations, the cryo-EM NET dimer reported by Zhang et al. [13] was used in the outward-open state at 2.89Å resolution (PDB: 8YR2) [44]. This structure contains the two NET protomers as symmetric homo-dimer arrangement with additional co-resolved components, including lipids (cholesterol, PI and PIP₂), water molecules, ions, and nisoxetine. For the subsequent preparation steps, only the protein dimer was retained, whereas the lipids and ions were re-inserted later in the workflow, as described at the end of this chapter. For DAT simulations, a cryo-EM monomer structure from Nielsen et al. [71] in the outward-open state (2.66Å, PDB: 9EO4) [72] served as the template. The DAT monomer was aligned to the protomer positions of the NET dimer, thereby generating a DAT dimer with the NET-derived interface geometry for all DAT simulation systems.

The initial orientation of the protein with respect to the membrane was obtained using the PPM 3.0 Web Server [73] with default settings, ensuring a physically plausible insertion depth and tilt.

Next, the all-atom protein structure was converted to a coarse-grained (CG) MARTINI3 representation using martinize2 with vermouth 0.13.1.dev140 [74, 75]. MARTINI3 protein mapping was applied to both protomers [68]. To maintain the structural integrity of the protomers in the CG model, the ELNEDIN elastic network approach was employed [70]. An elastic bond force constant of 700 kJ mol⁻¹ nm⁻² was used, with a lower cutoff of 0.5 nm and an upper cutoff of 0.9 nm for bond formation. In addition, both N- and C-termini of the protomers were neutralized.

All membrane models were built and the protein was embedded using the INSANE workflow [76]. The systems were solvated with water, and Na⁺/Cl⁻ ions were added to reach a salt concentration of 0.15 M. All remaining INSANE parameters

were kept as default values.

To explore the influence of membrane environment, different lipid compositions were simulated. Specifically, a simple, symmetric membrane (Simp) consisting only of 1-Palmitoyl-2-oleoyl-glycero-3-phosphocholine (POPC) and cholesterol was compared to complex, asymmetric membranes derived from Ingólfsson et al. [77]: an average human plasma membrane (Avg) and an average neuronal plasma membrane (Neuron). Because the proposed neuronal membrane includes glycolipids whose headgroups are not yet parameterized in MARTINI3, the script lipid-itp-generator-Martini3-01.py [78] was used to generate an alternative lipid topology. In this modified topology, the glycolipid headgroup was replaced by an phosphoinositol headgroup to preserve similar biophysical characteristics while keeping the remaining lipid structure consistent with the published composition. Preserving the interfacial cholesterol, PI, and PIP₂ molecules observed in the cryo-EM structure was considered essential, as these components were suggested to contribute to dimer stabilization [13]. Therefore, these all-atom lipids were transferred into the CG membrane-protein model by fitting their coordinates relative to the protein backbone such that their positions and orientations within the dimer interface were retained. In the cryo-EM structure, PI and PIP₂ were modeled with fatty-acid chains of only eight carbons. To avoid potential bias from this likely experimental-modeling limitation, the acyl chains were elongated in silico using PyMOL [79] by adding carbon atoms into available vacuum space to minimize steric clashes. The chain extension was continued until the acyl-chain length matched that of the MARTINI3 PIP₂ model SAP6 [80], yielding PI/PIP₂ variants consistent with the SAP6-length lipids present in the bulk membrane (and analogously for PI). Subsequently, cholesterol, PI/PIP₂, and the protein-internal ions resolved in the cryo-EM (two sodium and one chloride ion per protomer) were mapped to their MARTINI representations using custom scripts based on the respective MARTINI literature [68, 69, 80]. In addition, one system was constructed in the average membrane environment without the reinserted PI/PIP₂ molecules to test their potential contribution to dimer stability. Notably, due to the decreased number of PI/PIP₂ molecules this variant has an altered membrane composition and is referred to as "Avg (no interface-PI)".

The exact lipid compositions of all membrane environments are summarized in Table 3.1. Note that the mol% values can deviate slightly from the original literature compositions due to the additional insertion of cholesterol and/or PI/PIP₂ molecules originating from the cryo-EM structure.

To generate the palmitoylated dimer, the membrane-oriented all-atom structure obtained from PPM 3.0 served as input for in-silico mutation using the CHARMM-GUI [81] PDB Manipulator [82] with default settings. Leucine 578 was mutated to cysteine (Cys578), a residue located near TM12 and corresponding to Cys581

Table 3.1.: Leaflet compositions (mol%) for the four membrane models used in this work, derived from the membrane compositions reported by Ingólfsson et al. [77]. Full lipid names are defined in Appendix A.2.

Lipid (mol%)	Simp		Avg		Avg (no interface-PI)		Neuron	
	Extracellular	Cytosolic	Extracellular	Cytosolic	Extracellular	Cytosolic	Extracellular	Cytosolic
CHOL	32.4	32.4	36.1	27.5	36.3	27.9	45.6	45.9
POPC	67.6	67.6	22.4	13.8	22.6	13.9	17.3	13.9
PIP ₂	-	-	-	2.7	-	2.0	-	1.7
PI	-	-	0.7	0.7	-	-	0.4	0.4
SSM	-	-	22.4	10.7	22.6	10.9	10.2	2.2
PAPC	-	-	11.2	7.4	11.3	7.5	6.0	-
PAPS	-	-	-	16.1	-	16.3	-	14.9
DLPE	-	-	5.4	16.1	5.5	16.3	-	-
POPE	-	-	1.7	5.0	1.7	5.1	-	-
PAPE	-	-	-	-	-	-	9.3	21.0
PNPI	-	-	-	-	-	-	11.2	-

in human DAT, as identified by structural alignment of the protein backbone. Palmitoylation was then introduced at Cys578 by attaching a 16-carbon chain oriented towards the membrane. The resulting structure was then mapped to MARTINI3 and embedded into the membrane using the same protocol applied for the non-palmitoylated systems. Parameters for the palmitoylation modification were taken from the recent MARTINI3 parameterization by Koukos et al. [83].

DAT systems were prepared analogously to the NET setups described above. In contrast to NET, palmitoylation was attached at the native site Cys581. Because the DAT cryo-EM structure contains an unmodelled loop segment, this region was reconstructed using the loop modeling module of MODELLER [84]. In total, 100 loop conformations were generated and the model with the lowest DOPE score was selected for subsequent processing. Notably, DAT was only simulated in the Avg membrane, and the batch is referred to as "Avg (DAT)".

For the NET dimer in the four membrane environments, 8 independent replicas were generated for each condition (nonpalm/palm). Replicas were identical in the system preparation workflow. Additionally, a set of 8 replicas per condition (non-palm/palm) was prepared for DAT in the average membrane model, as described above. An overview of all simulated systems and their distinguishing features is provided in Table 3.2.

Notably, production simulations were run for 25 μ s per replica for all systems, except for NET in the simple membrane, which was simulated for 10 μ s after weighing expected informational gain against computational cost. All systems were constructed in a 15 \times 15 \times 10nm simulation box, except for NET in the neuronal membrane, which used a larger box of 18 \times 18 \times 10nm. The increased lateral box

Table 3.2.: Overview of all simulated systems, including the simulated protein, palmitoylation state, number of repeats, production time, and simulation box size.

System	Protein	Membrane model	Palmitoylation	Repeats	Production time (μs)	Box size (nm)
(1) Simp nonpalm	NET	Simple	No	8	10	$15 \times 15 \times 10$
(1) Simp palm	NET	Simple	Yes	8	10	$15 \times 15 \times 10$
(2) Avg nonpalm	NET	Average	No	8	25	$15 \times 15 \times 10$
(2) Avg palm	NET	Average	Yes	8	25	$15 \times 15 \times 10$
(3) Neuron nonpalm	NET	Neuronal	No	8	25	$18 \times 18 \times 10$
(3) Neuron palm	NET	Neuronal	Yes	8	25	$18 \times 18 \times 10$
(4) Avg (no interface-PI) nonpalm	NET	Average	No	8	25	$15 \times 15 \times 10$
(4) Avg (no interface-PI) palm	NET	Average	Yes	8	25	$15 \times 15 \times 10$
(5) Avg (DAT) nonpalm	DAT	Average	No	8	25	$15 \times 15 \times 10$
(5) Avg (DAT) palm	DAT	Average	Yes	8	25	$15 \times 15 \times 10$

dimensions in this case were chosen to support stable maintenance of the dimer within the more complex neuronal membrane environment.

3.2. Simulation protocol and parameters

Following system assembly, all systems were simulated using an identical multi-stage MD protocol comprising minimization, restrained equilibration, pre-production relaxation, and production sampling, outlined in Figure 3.1.

All simulations were carried out with GROMACS 2024.4 [85, 86] and the most recent release of the MARTINI3 force field [68, 78, 87]. Simulations were executed on the VSC5 supercomputer operated within the Austrian Scientific Computing infrastructure.

All systems were prepared and equilibrated in a multi-stage workflow prior to data collection in the production phase. Starting from the assembled systems (Section 3.1), each system underwent energy minimization, stepwise equilibration under semi-isotropic NPT conditions, pre-production relaxation phase, and finally the unrestrained production simulation used for analysis. Throughout energy minimization and equilibration, the dimer interface (including the interface cholesterol/PI/PIP₂ molecules and structural ions) was restrained to its initial configuration using a force constant of 1000 kJ mol⁻¹ nm⁻². During pre-production, restraints were reduced to 100 kJ mol⁻¹ nm⁻² to allow further relaxation while maintaining the overall interface geometry.

Energy minimization. Each system was minimized using the steepest-descent algorithm until the maximum force fell below 10 kJ mol⁻¹ nm⁻¹. Minimization was performed with a step size of 0.01 nm and a maximum of 75 steps. To robustly

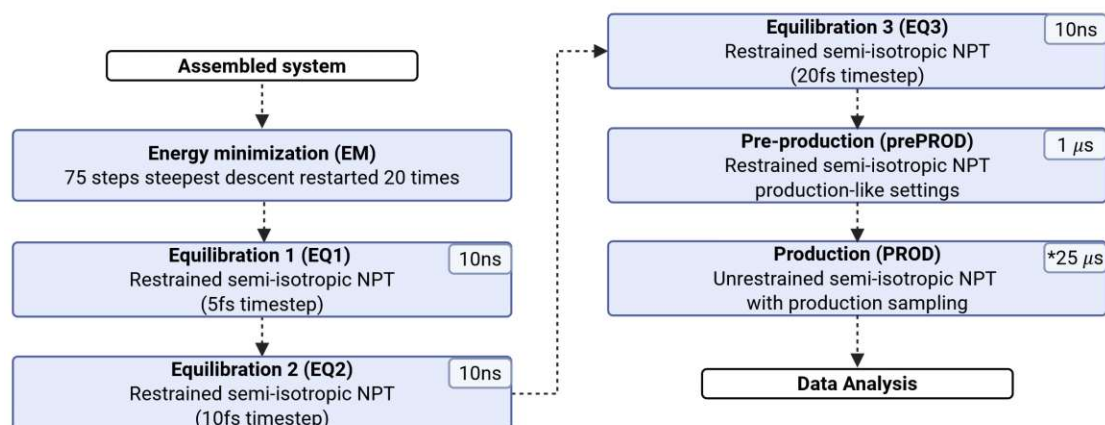


Figure 3.1.: Simulation protocol applied to all systems, comprising restrained energy minimization, three restrained equilibration stages, a less-restrained pre-production phase, and an unrestrained production phase used for trajectory sampling. *Production was 25 μs for all systems except the Simp systems (10 μs).

remove steric clashes and avoid local energy minima, the minimization procedure was restarted and repeated 20 times.

Equilibration runs. Three consecutive equilibration simulations under semi-isotropic NPT conditions were performed, each with a duration of 10 ns, while progressively increasing the integration time step and relaxing the temperature- and pressure-coupling. The time step was increased from 5 fs to 10 fs to 20 fs across EQUIL1-EQUIL3. The first two equilibration stages employed the Berendsen thermostat and Berendsen semi-isotropic barostat, whereas in the third equilibration stage the coupling scheme was switched to the v-rescale thermostat and the c-rescale semi-isotropic barostat.

Pre-production. To further relax the membrane environment, the pre-production phase was simulated for 1 μs under the same v-rescale/c-rescale semi-isotropic NPT conditions with a 20 fs time step and random initial velocities were generated according to a Maxwell distribution at 310 K.

Production with data sampling. Production simulation was performed for 25 μs (only exception: simp system for 10 μs) under the same conditions and initial velocity generation as pre-production. As mentioned before, during production all

force restraints were released, making the resulting trajectory valuable for data analysis and result interpretation.

All MD simulations used the GROMACS-implemented potential-shift Verlet scheme for non-bonded interactions with a cutoff of 1.1 nm for both van der Waals and electrostatic interactions. Electrostatics were treated with the reaction-field method using a dielectric constant of 15, and Lennard-Jones interactions were shifted with no dispersion correction. In all stages after energy minimization, semi-isotropic pressure coupling to 1 bar was applied (Berendsen or *c*-rescale as specified above) using a compressibility of $3 \times 10^{-4} \text{ bar}^{-1}$ in both the *xy* plane and the *z* direction. The barostat coupling time constant was 3 ps for EQUIL1 and EQUIL2, and was set to 4 ps from EQUIL3 onwards. Temperature coupling was applied separately to the groups protein, membrane, and solvent, each coupled to 310 K using either the Berendsen thermostat (EQUIL1/EQUIL2) or the *v*-rescale thermostat (EQUIL3 onwards) with a coupling constant of 1 ps. Temperature coupling was applied every 20 simulation steps. Periodic boundary conditions were applied in all three dimensions throughout equilibration and production.

For the DAT systems, an additional short equilibration stage (EQUIL0) was required for simulation stability prior to EQUIL1. This short-term "EQUIL0" was run for 5 ps with a 1 fs time step, using the same positional restraints ($1000 \text{ kJ mol}^{-1} \text{ nm}^{-2}$) and Berendsen coupling, with a coupling time constant of 10 ps.

A full overview of the parameters used for the GROMACS simulation stages is provided in Appendix A.1.

3.3. Data Analysis

This section describes the analysis workflow used to address the research question on how palmitoylation influences MAT dimerization. Unless stated otherwise, all analyses were performed on trajectory data from the production phase only. Trajectories were written at 100 ps intervals and subsequently downsampled to 1 ns to reduce computational cost.

Analyses were performed using either GROMACS tools (*gmx*) or the MDAnalysis Python package [88], as indicated for each step. Standard Python 3 libraries were used for post-processing (NumPy, SciPy, pandas) and visualization (Matplotlib, seaborn). To provide a consistent reference frame for comparing dimer conformations, the downsampled trajectories were transformed such that one protomer of the dimer was kept fixed in the center of the simulation box. This was achieved by translating and rotating all coordinates in the *xy* plane relative to the selected protomer using *gmx trjconv* with `-fit rotxy+transxy`. All subsequent analyses used these fitted trajectories unless noted otherwise.

3.3.1. Root mean square deviation measurements

Root mean square deviation (RMSD) was computed for key components of the cryo-EM-derived interface, namely the non-fixed protomer, the interface cholesterol molecules, and the PI and PIP₂ molecules. For each trajectory, the reference structure was defined as the first frame of the production phase. RMSD calculations were performed on the fitted trajectories described above.

For each molecule, bead-wise displacement vectors relative to the reference coordinates were computed using `MDAAnalysis.lib.distances.minimize_vectors()`, which returns the minimum-image displacement and therefore accounts for periodic boundary conditions. For the protein, RMSD was calculated using all backbone beads. For PI and PIP₂, only headgroup beads were included (i.e., excluding lipid tails and glycerol linkers). For cholesterol, all beads were included. RMSD was computed as

$$\text{RMSD} = \sqrt{\frac{1}{N} \sum_{i=1}^N \|\Delta \mathbf{r}_i\|^2}, \quad (3.1)$$

where N is the number of selected beads and $\Delta \mathbf{r}_i$ is the minimum-image displacement vector of bead i relative to the reference frame.

3.3.2. Density maps

Two-dimensional density maps were generated from an extracellular top-view projection along the membrane normal (z axis). Density calculations were performed with `gmx densmap` using the option `-unit count` to obtain raw bead counts per grid bin. In `gmx densmap`, counts are reported as per-frame values, which enables direct comparison between simulations with different lengths (i.e., different numbers of frames). Density maps were computed for (i) the non-fixed protomer (referred to as the flexible protomer), (ii) PI, (iii) PIP₂ and (iv) cholesterol molecules. For each selected group, the value assigned to a grid bin (x, y) corresponds to the number of beads (or molecules, depending on the index selection) falling into that bin, averaged over all frames:

$$\rho(x, y) = \frac{1}{T} \sum_{t=1}^T n_t(x, y), \quad (3.2)$$

where T is the number of analyzed frames and $n_t(x, y)$ is the count in bin (x, y) at frame t as returned by `gmx densmap`.

3.3.3. Transmembranehelix contact measurements

While the density maps capture the relative orientation of the protomers relative to the fixed one, they do not directly resolve the specific transmembrane (TM) helix contacts defining the dimer interface. Therefore, an additional interface analysis was performed by quantifying inter-helix distances between TM1-TM12 in a matrix-based representation. The overall approach was conceptually based on the method described by Zeppelin et al. [20], with adjustments as detailed below.

Index groups for each TM helix were defined according to the helix boundaries reported in the sequence annotation of the corresponding PDB entries for NET (8YR2 [44]) and DAT (9EO4 [72]). Inter-helix distances were computed using `gmx mindist`, which reports the minimum distance between two index groups (i.e., the closest distance between any beads belonging to the respective helices). Thus, for each helix pair, a single minimum-distance value was obtained per frame.

For downstream quantification, a helix pair was classified as *contact* in a given frame if the minimum distance was below 1.0 nm. This cutoff differs from the 0.6 nm threshold used by Zeppelin et al. [20], because here also lipid-mediated interfaces were intended to be captured, which can exhibit larger characteristic separations. For each helix pair (i, j) , contacts per frame were computed as

$$c_{ij}(t) = \begin{cases} 1, & \text{if } d_{ij}(t) < 1.0 \text{ nm} \\ 0, & \text{otherwise} \end{cases} \quad \text{and} \quad C_{ij} = \frac{1}{T} \sum_{t=1}^T c_{ij}(t). \quad (3.3)$$

where T is the number of analyzed frames, $d_{ij}(t)$ is the `gmx mindist`-reported minimum distance for helix pair (i, j) at frame t .

To remove any dependence on protomer labeling, each per-replica TM contact matrix was symmetrized by averaging it with its transpose (i.e. C_{ij} with C_{ji}), such that the reported contact frequency for a helix pair is identical regardless of which protomer contributes which helix. To assess significant differences between non-palmitoylated and palmitoylated conditions within each membrane environment, Welch's t-test [89] was applied to the replica-wise contact measurements (Contacts per frame C_{ij}) for each helix pair. Welch's t-test is a two-sample t -test that does not assume equal variances between groups, in contrast to Student's t -test. The test assumes independence between observations (here: independent simulation replicas in the nonpalm vs. palm batches) and an approximately normal distribution of the observations. Test statistics t and p -values were computed using SciPy's `ttest_ind()` with `equal_var=False`.

3.3.4. Lipid contact analysis at the palmitoylation site

To further investigate the influence of palmitoylation on the local membrane environment, lipid contact counts were quantified around the palmitoylation site.

A lipid was counted as being in contact in a given frame if any headgroup bead of that lipid was within 1.2 nm of the target residue. For cholesterol molecules, all beads were considered. A cutoff of 1.2 nm was chosen to capture the broader local lipid environment around the site, rather than only strict, direct residue-lipid interactions.

For NET, the target residue was 578Leu in the non-palmitoylated systems and 578Cys in the palmitoylated systems, whereas for DAT the native site 581Cys was used in both conditions. Distances were evaluated using only the backbone bead of the respective residue as the reference point. Headgroup beads were defined as "NC3 P04 GL1 GL2 NH3 CNO AM1 AM2 C1 C2 C3 C4 C5 C6 P1 P2 P3 ROH R1 R2 R3 R4 R5 R6", corresponding to the headgroup bead names of the CG lipid species present in the systems. Per-frame contacts were computed using `MDAnalysis.lib.distances.capped_distance`.

Because lipid compositions and concentrations differed between membrane models, raw contact counts were scaled by lipid concentration in the lower leaflet to enable comparison across systems. Specifically, scaling used the total number of lipids in the lower leaflet and the lateral box dimensions at the start of the production phase (lipids per xy box area), thereby approximating the expected "encounter" frequency under a uniform lipid distribution. Under this assumption, a higher scaled signal corresponds to an enrichment of the respective lipid species around the palmitoylation site relative to a uniform distribution. Scaled contact counts were computed as

$$S = T \cdot \left(\frac{N_{\text{lip}}}{A} \right), \quad (3.4)$$

$$C_{\ell}^{\text{scaled}} = \frac{C_{\ell}}{S}, \quad (3.5)$$

where T is the number of analyzed frames, N_{lip} is the total number of lipids in the lower leaflet, A is the membrane area derived from the box dimensions (i.e., the xy box area at the beginning of production), and C_{ℓ} is the total (raw) contact count for lipid species ℓ accumulated over all frames.

4. Results

The simulations described in Chapter 3 yielded 80 independent production trajectories across the different membrane environments and palmitoylation states. This chapter presents the corresponding analysis results and addresses the research question of how MAT palmitoylation influences dimerization in a stepwise manner. First, the dynamics of the inter-protomer arrangement are assessed using RMSD time series (Section 4.1). Next, preferred configurations and spatial distributions are visualized using two-dimensional density maps (Section 4.2) and interface preferences are quantified directly via TM-TM contact analysis (Section 4.3). Finally, potential palmitoylation-dependent changes in the local lipid environment are evaluated by lipid contact analysis around the palmitoylation site (Section 4.4).

4.1. Root mean square deviation time series

To quantify deviations from the initial dimer interface, RMSD time series were computed with respect to the first frame of the production phase. Because one protomer was used as a fixed reference frame (rotational and translational alignment in the xy plane), the RMSD of the second (flexible) protomer reports changes in the relative dimer geometry compared to the starting configuration. If the cryo-EM-derived interface were preserved, the RMSD would remain low. Therefore, an increase in RMSD indicates rearrangement away from the initial interface geometry, but not necessarily complete dissociation.

Figure 4.1 shows the RMSD over time for the flexible protomer across all membrane models and both conditions (nonpalm and palm). Individual traces correspond to the independent replicas. In all systems, the flexible protomer departs from the initial configuration, and no trajectory maintains an RMSD below 1.0 nm over the full simulation time. While some replicas remain close to the initial arrangement during early simulation time (e.g., Avg-palm-rep8, Neuron-nonpalm-rep8, Neuron-nonpalm-rep1), none remains stable beyond approximately 10 μ s. Most trajectories deviate rapidly from the starting geometry and do not return to it. In several systems, RMSD plateaus are observed, which suggest metastable interface geometries. This behavior is particularly apparent in Avg (no interface-PI)-palm and Neuron-palm.

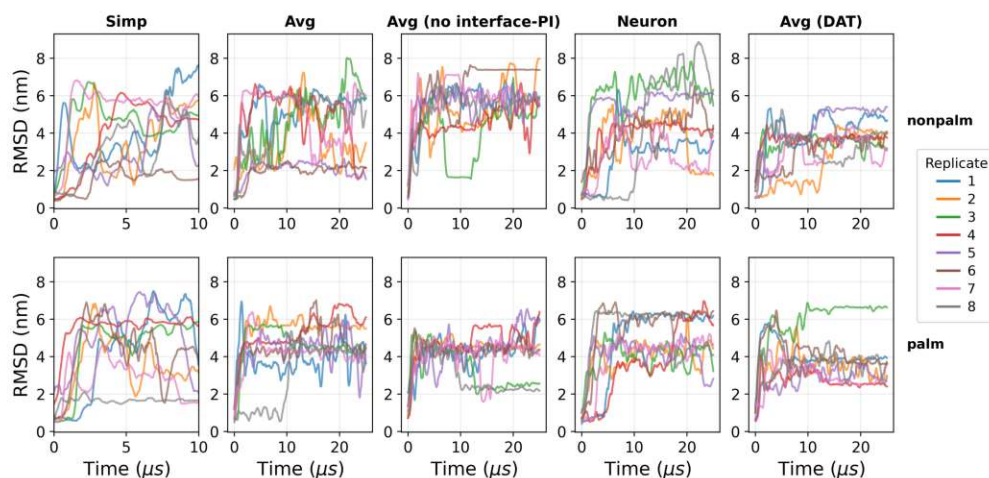


Figure 4.1.: RMSD of the flexible protomer relative to the first production frame for all systems. A moving average with a window size of 500 frames was applied.

RMSD was also computed for interface-associated cholesterol and PI/PIP₂ molecules originating from the cryo-EM structure. Figure 4.2 illustrates the cholesterol RMSD for the Neuron-nonpalm system as a showcase. For this simulation batch, all eight replicas are shown, and each trace within a replica represents an individual cholesterol molecule. All of them diffuse away from their initial positions over time, and this behavior is consistently observed across systems and conditions (additional traces are provided in Appendix A.3.1).

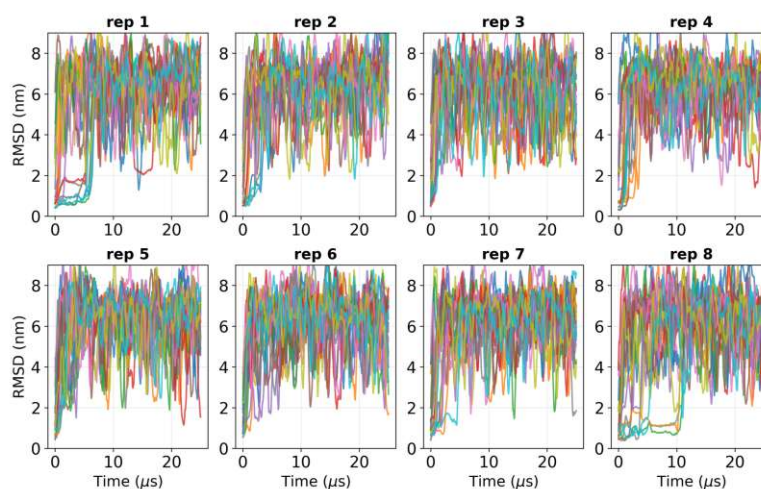


Figure 4.2.: RMSD of the cryo-EM-derived interface cholesterol molecules relative to the first production frame, shown for the Neuron-nonpalm system. Individual cholesterol molecules are shown as separate traces in different colors. A moving average with a window size of 500 frames was applied. Corresponding plots for all other systems are provided in Appendix.

Figure 4.3 shows the RMSD of the cryo-EM-derived PIP₂ molecules for the Avg-nonpalm system as a showcase. While transient binding and plateau-like behavior are observed for individual molecules (e.g. in rep 8), the interpretation depends on which protomer the lipid associates with. Similar behavior can be observed for the cryo-EM-derived PI molecules in the system Neuron-nonpalm in Figure 4.4, with less transient binding, most dominantly the orange trace in rep 7. As the RMSD is computed relative to the fixed protomer, lipids bound to the flexible protomer will exhibit RMSD changes correlated with protomer motion even if the lipid remains bound. Thus, plateaus most strongly indicate association with binding sites on the fixed protomer. Nevertheless, PI/PIP₂ molecules do not remain collectively fixed at their initial interface positions, similar to cholesterol. Corresponding PI/PIP₂ RMSD traces for all systems are shown in Appendix A.3.2, A.3.3.

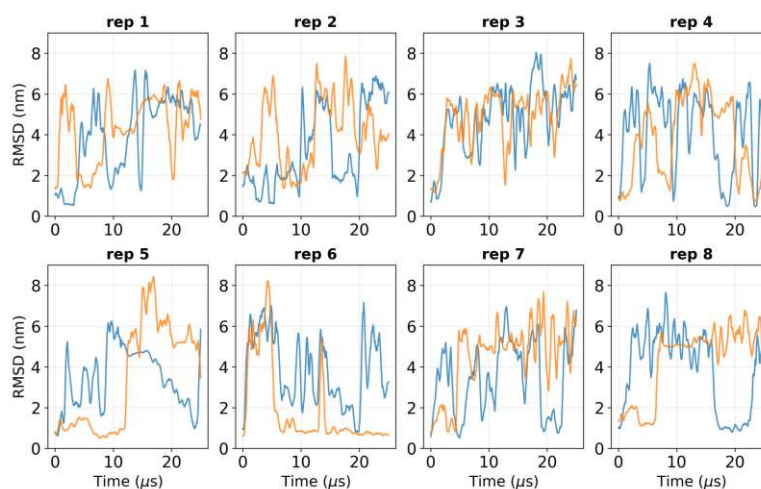


Figure 4.3.: RMSD of the cryo-EM-derived PIP₂ molecules relative to the first production frame, shown for the Avg-nonpalm system. The two PIP₂ molecules are shown in separate colors. A moving average with a window size of 500 frames was applied. Corresponding plots for all other systems are provided in Appendix.

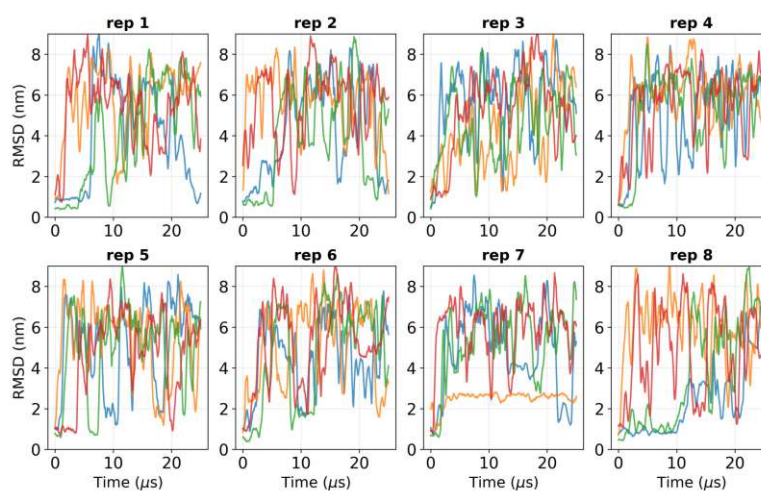


Figure 4.4.: RMSD of the cryo-EM-derived PI molecules relative to the first production frame, shown for the Neuron-nonpalm system. The four PI molecules are shown in separate colors. A moving average with a window size of 500 frames was applied. Corresponding plots for all other systems are provided in Appendix.

4.2. Density maps of molecules of interest

To visualize preferred relative configurations of the dimer components, two-dimensional density maps were computed for the flexible protomer as well as for selected lipid species (PIP₂ and PI). The maps report the average occupancy in the x - y plane (extracellular top view) relative to the fixed protomer, which provides a stable reference frame across trajectories. Unless stated otherwise, density maps are shown as per-frame normalized bead counts per grid bin averaged over time and over the 8 replicas for each system and condition.

Figure 4.5 shows the density of the flexible protomer for all simulated systems (averaged over 8 replicas), separated by nonpalm and palm conditions. The outline of the initial cryo-EM dimer configuration is overlaid in gray, with the fixed protomer centered and the flexible protomer initially positioned on the right. Across all systems, no dominant occupancy maximum coincides with the initial cryo-EM interface region, consistent with the RMSD results in Section 4.1. In the simple membrane (Simp), both nonpalm and palm conditions show broad, dispersed occupancies, indicating substantial variability across replicas without a single highly preferred relative position. In the NET systems with complex membranes, distinct hotspots are observed, typically comprising two dominant regions, suggesting preferred relative positions of the flexible protomer. Because these maps do not encode the rotational orientation of the protomer around its own axis, distinct hotspots can in principle arise from different helix-helix interfaces or from similar interfaces realized at different relative rotations of the fixed protomer towards the flexible one. Therefore, the specific TM-TM interface is quantified explicitly in the contact matrix analysis (Section 4.3). A modest shift in the preferred relative position/orientation is apparent between nonpalm and palm conditions in the Avg and Avg (no interface-PI) systems, whereas the Neuron system shows less pronounced differences. In the Avg (DAT) systems, the strongest and most localized protein-density signal is observed, with the nonpalm condition exhibiting a more concentrated occupancy than the palmitoylated condition.

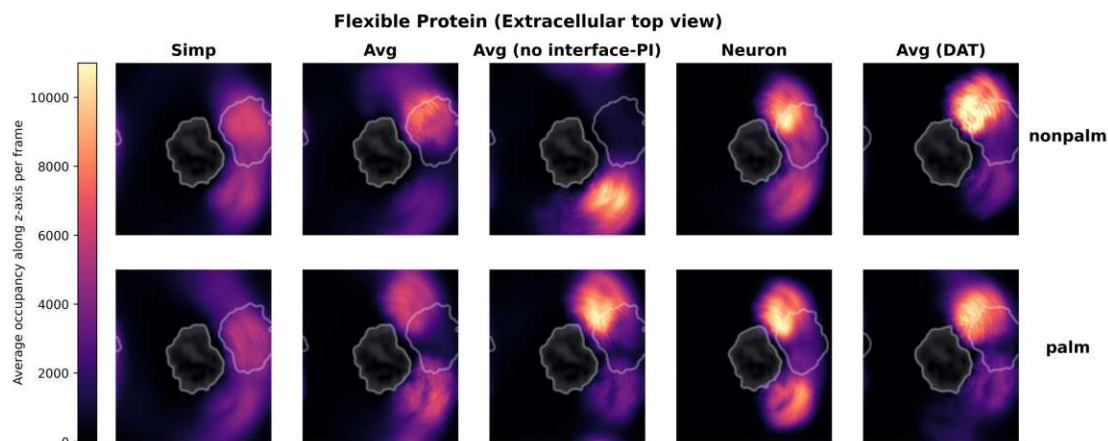


Figure 4.5.: Density map of the flexible protomer in the x - y plane (extracellular top view) for each system, averaged over all repeats. The signal reflects the per-frame-averaged occupancy (bead counts per bin) over time. The initial cryo-EM configuration is shown as a gray outline. Note that the Neuron systems appear smaller due to the larger simulation box size.

Figure 4.6 shows the corresponding density maps for PIP₂ (all PIP₂ molecules in the system), for the systems in which PIP₂ was present (Avg, Neuron, Avg (DAT), and Avg (no interface-PI)). The density maps highlight regions of frequent PIP₂ occurrence relative to the transporter. Several PIP₂ hotspots localize near the dimer-interface region, compared to the dominant protein-density states (Figure 4.5). A small bias toward the initial interface region is expected because the cryo-EM-derived interface lipids were restrained until the start of the production phase. This bias is not present in the Avg (no interface-PI) system where no interface PI/PIP₂ molecules were inserted. Notably, in Avg (no interface-PI) the palm condition exhibits a clear hotspot at the upper side of the protomer that lies between the dominant protein-density states, whereas the corresponding nonpalm condition shows a distinct preference for a lower region of the protomer. In the Avg (DAT) systems, PIP₂ hotspots occur at different locations compared to NET, and do not correlate with the dominant protein-density interface regions, indicating a different relationship between PIP₂ localization and preferred relative rprotomer positions.

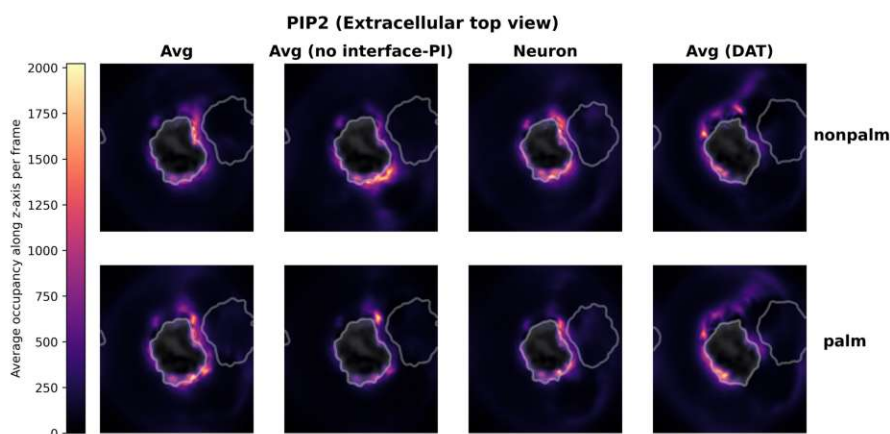


Figure 4.6.: Density map of all PIP₂ molecules in the x - y plane (extracellular top view) for each system containing PIP₂, averaged over all repeats. The signal reflects the per-frame-averaged occupancy (bead counts per bin) over time. The initial cryo-EM configuration is shown as a gray outline. Note that the Neuron systems appear smaller due to the larger simulation box size.

Figure 4.7 shows density maps for PI molecules originating from the cryo-EM structure (included only in the Avg, Neuron, and Avg (DAT) systems). Compared to PIP₂, PI occupancy is more broadly distributed with weaker hotspot intensities, indicating weaker binding with the transporter. Overlap between PI and PIP₂ hotspot regions suggests that both lipids can populate similar regions near the protein, indicating potential competition for binding sites.

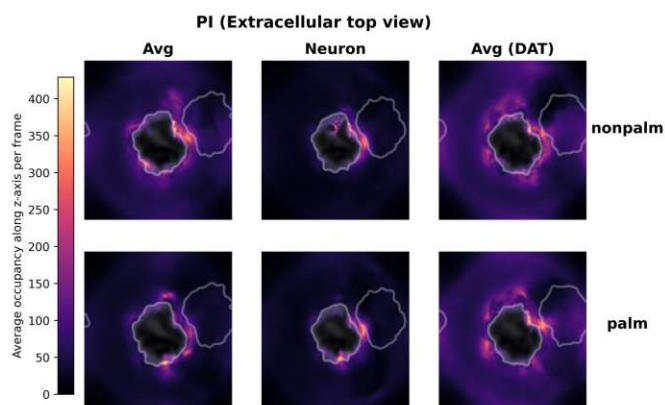


Figure 4.7.: Density map of PI molecules in the x - y plane (extracellular top view) for each system containing PI, averaged over all repeats. The signal reflects the per-frame-averaged occupancy (bead counts per bin) over time. The initial cryo-EM configuration is shown as a gray outline. Note that the Neuron systems appear smaller due to the larger simulation box size.

Density maps were also generated for cholesterol. As no distinct features were observed, these maps are provided in Appendix A.6.

4.3. Transmembranehelix contact analysis

To characterize preferred dimer interfaces and quantify differences between non-palm and palm conditions, the relative orientation of the protomers was analyzed in terms of TM-TM contacts. As a reference, Figure 4.8 shows the TM contact matrix of the initial cryo-EM-derived NET dimer configuration computed from a single frame. In this starting configuration, contacts are detected between TM4/TM12, TM9/TM12, and TM9/TM9 (cutoff: 1.0 nm).

Figure 4.9 summarizes the mean TM-TM contact frequencies (contacts per frame) for each system and condition. For each replica, the contact frequency C_{ij} was computed as a time average over the production frames with the matrices showing the mean across the 8 replicas. In the NET systems, the initial cryo-EM interface pattern (TM4/TM12, TM9/TM9, TM9/TM12) remains detectable but with reduced intensity, consistent with the structural rearrangements observed by RMSD and density maps. Across systems, additional contact signals are observed involving TM3/TM12 and TM8/TM12. Contacts involving the bundle-domain helices (TM1, TM2, TM6, TM7) are almost nonexistent, whereas contacts are enriched among helices associated with the scaffold domain and TM12. Additional

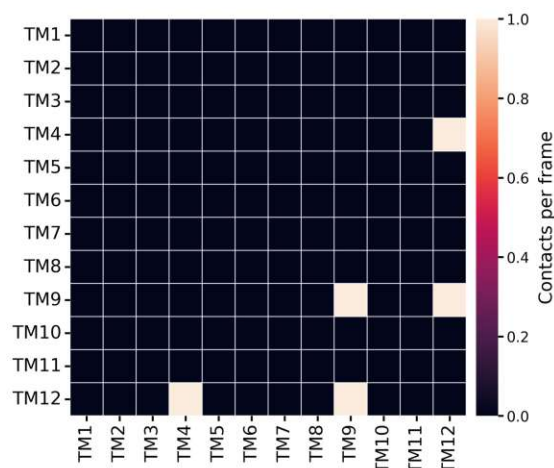


Figure 4.8.: TM contact matrix of the initial NET dimer configuration computed from a single frame (cutoff: 1.0 nm).

interface patterns include contacts between TM3,4 and TM9,10 as well as TM3,4 and TM4.

The strongest mean contact frequency was observed for TM4/TM12 in Avg (DAT) nonpalm (0.56 ± 0.18 contacts per frame) and for Neuron palm (0.51 ± 0.049 contacts per frame). In the Avg (no interface-PI) nonpalm system, a distinct interface pattern was observed, with comparatively strong TM4/TM4 and TM4/TM5 contacts (0.41 ± 0.26 and 0.43 ± 0.31 contacts per frame, respectively). A list of all mean and standard deviation values for all helix pairs is reported in Appendix A.4.

To visualize palmitoylation-dependent changes, Figure 4.10 shows the difference between palm and nonpalm contact frequencies (palm – nonpalm). Here, red indicates enrichment in the palmitoylated condition and blue indicates depletion (relative to nonpalm). The Simp systems show only minor differences between conditions. In contrast, Avg, Avg (no interface-PI), and Neuron exhibit enrichment of TM3/TM12, TM4/TM12, and TM8/TM12 contacts in the palm condition, with the largest effect in Avg (no interface-PI). In this system, depletion of TM4,5,8/TM4 contacts is also apparent, whereas this effect is weaker in Simp, Avg, and Neuron. For Avg (DAT), the trend is reversed for several interfaces, with reduced TM4/TM12 contacts in the palm condition and increased TM4/TM4 contacts. Moreover, contacts of TM9/TM12 show a decrease in the palm DAT system, distinguishing it from the NET systems, in which this interhelix contact remains unchanged.

Because contact patterns vary between replicas and systems, palmitoylation effects were assessed statistically using Welch’s t-test on replica-wise time-averaged

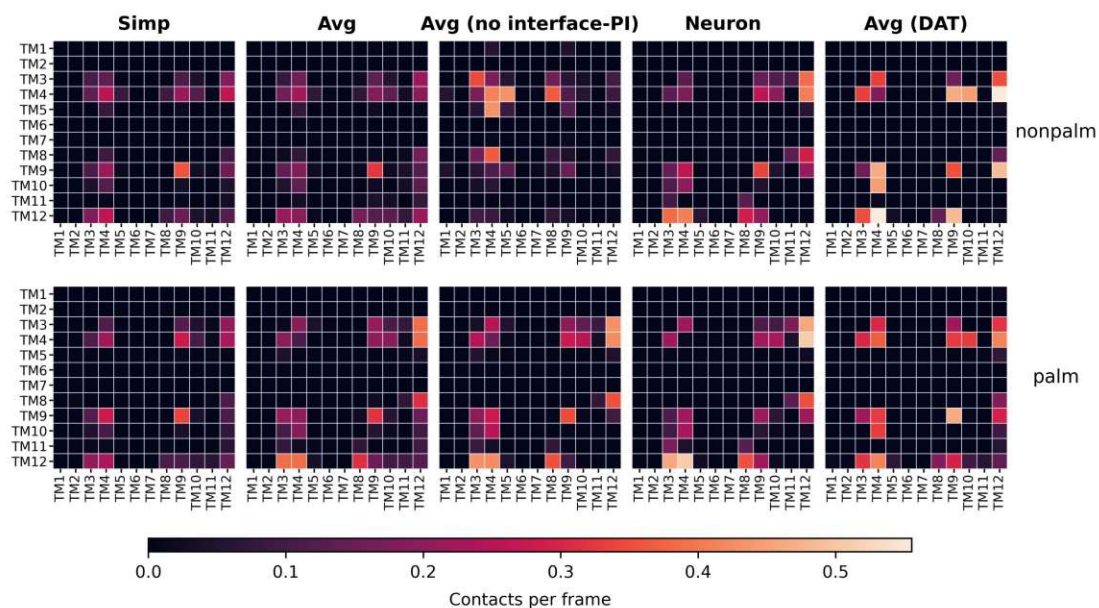


Figure 4.9.: TM contact matrices (contacts per frame with a cutoff of 1.0 nm) for all systems, shown as the mean across the 8 replicas for each condition.

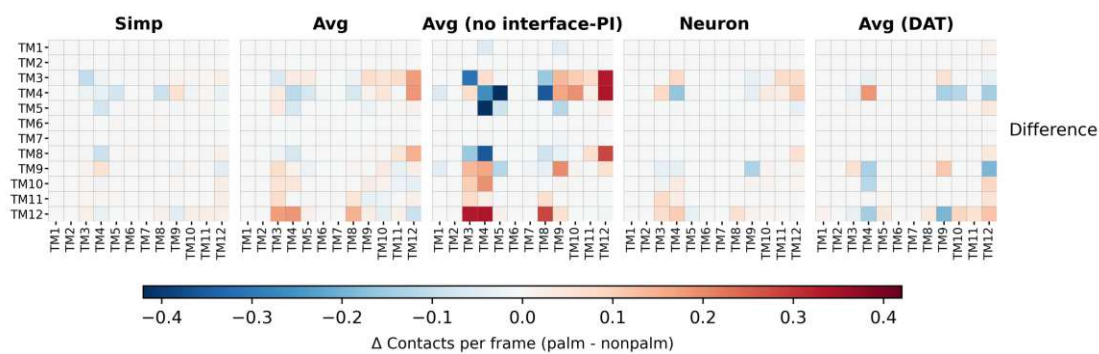


Figure 4.10.: Difference of TM contact matrices (palm - nonpalm) for each system (cutoff: 1.0 nm). Colors indicate enrichment (red color scale) or depletion (blue color scale) in the palm condition relative to the nonpalm condition.

contact frequencies. Figure 4.11 shows box-whisker plots for selected helix pairs chosen based on high abundance and/or strong differences in the mean contact matrices. Each distribution reflects the 8 independent replicas per condition within a given system.

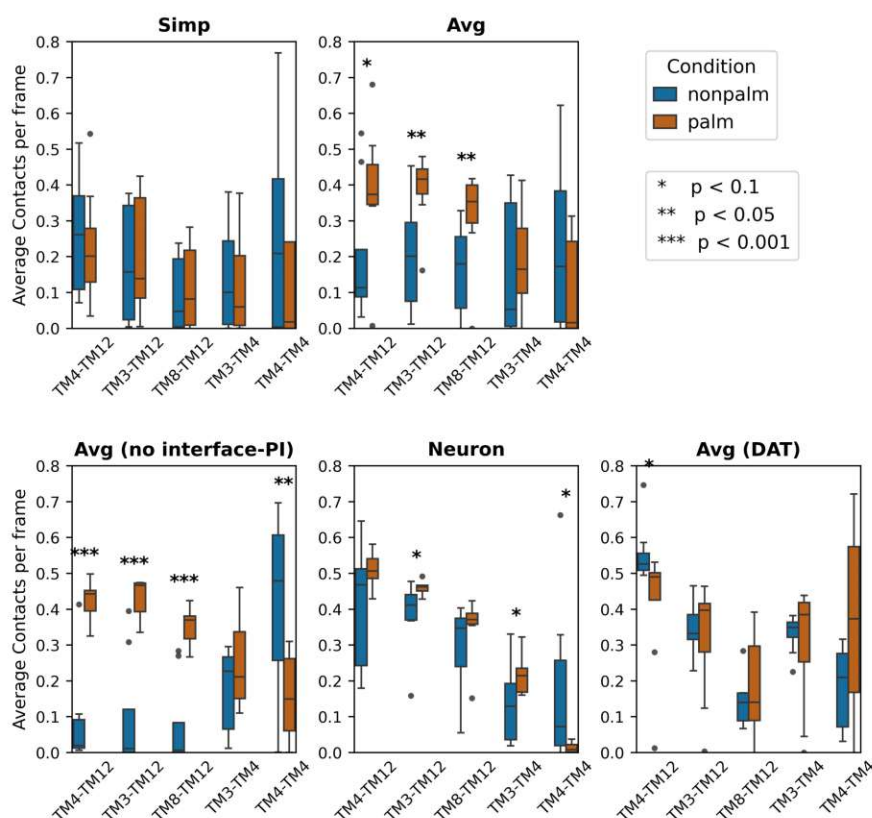


Figure 4.11.: Box-whisker plots comparing nonpalm and palm replica-wise contact frequencies for selected TM interfaces across all systems (cutoff: 1.0 nm).

Consistent with the contact matrices, TM3/TM12, TM4/TM12, and TM8/TM12 contacts were significantly increased in the palmitoylated condition for Avg (no interface-PI) ($p < 0.001$). The same directional trend was observed for Avg and Neuron, although with weaker statistical support. For Neuron, the TM4/TM12 difference did not reach the chosen significance threshold, but a similar directional trend could be observed. No significant differences between conditions were observed for the Simp system. Across NET systems (excluding Simp), replica-to-replica variability was generally lower in the palm replicas compared to the nonpalm regarding the interfaces shown. In NET, TM4/TM4 contacts tended

to be higher in the nonpalm condition, most prominently in Avg (no interface-PI). In contrast, the Avg (DAT) system showed a different trend for TM4/TM12 with weak statistical significance of palm being increased within this interface. No other tested interfaces for DAT differed significantly between conditions. Notably, variance across replicas was higher in the palm DAT system than in the nonpalm condition, which is opposite to the trend observed for the NET systems. Complete statistics (test statistics, p -values) are reported in Appendix A.5.

4.4. Lipid contacts with palmitoylation site

To assess whether palmitoylation alters the local lipid environment, we quantified contacts between the palmitoylation site (578Leu/578Cys for NET and 581Cys for DAT) and lipid headgroups within 1.2 nm. The non-palmitoylated condition serves as the reference. Figure 4.12 summarizes concentration-scaled contact counts across replicas, with each point representing one simulation replicate.

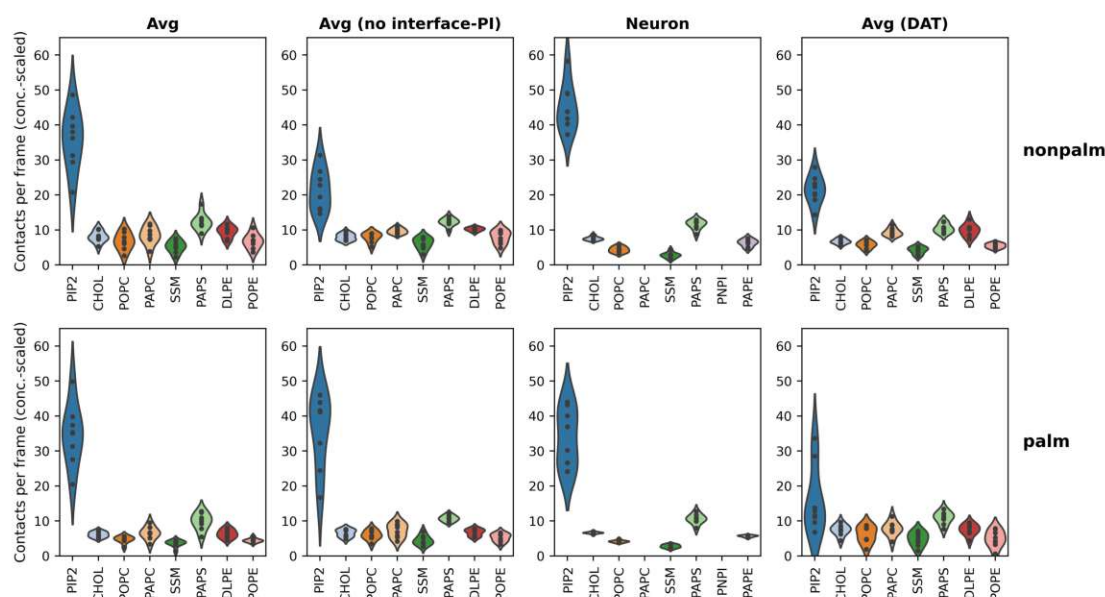


Figure 4.12.: Scaled lipid headgroup contacts at the palmitoylation site shown as violin plots across replicas for each system and condition. Points indicate the time-averaged, concentration-scaled value per replica. Contact cutoff: < 1.2 nm.

Across systems, PIP₂ exhibits the largest scaled contact signal in most cases. In contrast, in Avg (DAT) palm the PIP₂ contact signal is comparable to that of

other lipid species, aside from a small number of outliers. Comparing palm and nonpalm conditions within each membrane environment, PIP₂ contacts show no consistent directional trend across NET systems: Avg shows little change, Avg (no interface-PI) displays increased PIP₂ contacts in palm, whereas in Neuron the nonpalm condition shows higher PIP₂ contacts than the palmitoylated condition. Overall, PIP₂ contacts are lower in the DAT systems than in the NET systems. For other lipid species, scaled contact levels are generally lower and differences between palm and nonpalm conditions are comparatively small. The contact analysis for the simplified system is provided in Appendix A.7, as no notable deviations or trends were observed.

5. Discussion

5.1. Instability of the cryo-EM-derived dimer arrangement in MARTINI3

Across all membrane environments, the cryo-EM-derived NET dimer arrangement (PDB: 8YR2 [44]) did not persist in all simulations. Independent of palmitoylation state, the flexible protomer predominantly departed from the initial dimer geometry within the first microseconds as reflected by the RMSD traces, and none of the replicas maintained the starting configuration over the full production time. Consistently, the cryo-EM-derived interface lipids (Cholesterols, PI/PIP₂ molecules) did not remain in their initial positions once restraints were released. The densi-tymap analysis supported this interpretation by showing that the dominant occupancy hotspots of the flexible protomer were displaced from the initial cryo-EM configuration. Finally, the TM-TM contact matrices supported these observations on interface-defining level, as the initial cryo-EM interface contact signal was decreased, while other helix combinations became more prominent across systems.

Importantly, this finding should be interpreted as a statement about the behavior of the cryo-EM-derived arrangement within the present CG model and simulation protocol, rather than a definitive rejection of the cryo-EM interface at physiological state. The cryo-EM structure of NET suggests a lipid-mediated interface [13], where those specific cholesterol/PI/PIP₂ interactions contribute substantially to stabilization. Capturing such interfaces may require a particularly accurate description of e.g. the lipid headgroup electrostatics or specific binding geometries, which are not represented by the MARTINI3 force field. Contrary, the overestimation of generic protein-protein attraction is well documented for MARTINI2 [90]. A recent study reports MARTINI3 being still "too sticky" among proteins, while it has improved compared to MARTINI2 [91]. Therefore, our simulation environment would be expected to stabilize protein association in general, especially as the protomers are already in contact at the beginning of production phase. Consequently, the observation that the cryo-EM arrangement is not stable does not necessarily have to be only a phenomena of poor force field interactions, as the force field should actually over-stabilize the initial dimer geometry.

A second, related consideration is the experimental context of the cryo-EM structure, in particular the nanodisc environment. The interface could be stabilized by

nanodisc-specific properties such as altered lipid packing and local curvature. In such a scenario, the interface may be enriched in nanodiscs even if it represents only one of several possible dimer arrangements or a transient state in a physiological membrane. A direct way to probe this hypothesis computationally is to simulate the dimer in a nanodisc-like environment under comparable CG conditions, which has been shown to be feasible for membrane proteins [92]. If the cryo-EM arrangement remains stable in a nanodisc simulation using the same CG force field, this would suggest that the observed instability in extended bilayer simulations is driven primarily by the nanodisc-specific environment rather than by an intrinsic inability of MARTINI3 to support that arrangement.

Another strategy to assess the stability of the cryo-EM geometry is to use a more detailed all-atom force field. A promising starting configuration would be a backmapped structure taken immediately after the pre-production phase, when the membrane is assumed to be equilibrated but the cryo-EM arrangement is still maintained by restraints. Because our results show that most systems depart from the initial arrangement within less than one microsecond after restraints are released, testing whether lipid-mediated stabilization emerges at atomistic resolution should be feasible on accessible all-atom timescales. In addition, selected high-occupancy CG interface states observed during production could be backmapped and tested for persistence at atomistic resolution. These states could also be characterized via estimating the binding free-energy calculations in comparison to the cryo-EM-derived arrangement. Together, these follow-ups would help to discriminate whether the observed instability primarily reflects CG force-field limitations or instead results from differences between nanodiscs and physiological membranes.

5.2. Alternative interface populations and membrane-composition dependence

Although the cryo-EM-derived dimer arrangement did not persist in our MARTINI3 simulations, the trajectories consistently relaxed into alternative, metastable dimer configurations. This was demonstrated by RMSD plateaus of the flexible protomer and discrete hotspots in the protein density maps. Importantly, these alternative interfaces were not uniformly distributed across the protein surface: across all systems, contacts among the bundle-domain helices (TM1, TM2, TM6, TM7) were rare, whereas interfaces predominantly involved scaffold-domain-helices and TM12 (notably TM3/4, TM8/9/10, and TM12). This qualitative observation is consistent with earlier unbiased oligomerization studies of DAT which reported that dimerization primarily involves the scaffold domain while sparing the bundle domain [17]. In contrast to our study, this study used a large-scale unbiased MD

simulation approach, particularly by placing the protomers in different orientations towards each other in the membrane.

Relationship to previously reported MAT interfaces. Prior computational studies of DAT provide a useful reference frame for interpreting the interface families observed here. Zeppelin et al. reported that DAT dimer conformations in CG self-assembly simulations predominantly involve TM9 and/or TM11 and/or TM12 at the interface, and further showed that palmitoylation on TM12 can alter the free-energy landscape for separation of TM12-containing interfaces [20]. In our simulations, TM12-centered interfaces also emerged as prominent populations, but the dominant partners for TM12 differed depending on membrane model and transporter. In particular, contacts involving TM3/4-TM12 and TM8/9-TM12 were frequently observed for NET and DAT, and TM4/TM12 was especially strong in some systems. In contrast, TM9/TM11-driven interfaces reported for DAT in the self-assembly literature were hardly present in our NET and DAT systems, and TM11 and TM2 contacts were absent in our dataset. Differences are not unexpected given the distinct study designs (assembled two-protomer systems versus multi-protomer self-assembly), different membrane compositions, the transition from MARTINI2 to MARTINI3. Furthermore, that study used a DAT structure derived from *Drosophila* and refined by homology modeling, whereas our simulations were based on human NET and human DAT structures [20]. Evidence that TM12 (alone or in combination with TM9) is a recurring oligomerization element across SLC6 transporters also comes from SERT simulations and experiments discussed in the SERT dimer interface study by Periole and co-workers, which supports TM12 involvement in oligomeric interfaces [19].

Taken together, our observation that stable dimer configurations frequently involve TM12 and scaffold-domain helices is broadly compatible with the existing MAT literature. The precise helix partners and relative abundances, however, appear to be context-dependent.

Membrane composition as a determinant of interface selection. A key outcome of this study is that interface populations and their stability depend on the membrane environment. Across the NET systems, changing from a simple POPC/CHOL membrane (Simp) to complex asymmetric membranes shifted both the localization of protein-density hotspots and the dominant TM contact patterns, indicating that membrane composition modulates the stability of specific interfaces. Consistent with this view, lipid density maps suggest that PIP₂ and PI accumulate near the protein at regions that partially overlap with preferred protomer configurations. While this does not establish a direct causal role, it supports the idea that local lipid enrichment can bias which protomer surfaces are

most likely to engage in dimer interfaces.

Regarding the Simp model with complete PIP₂ depletion, our observations are in line with experimental work by Lüethi et al. [55], where PIP₂ depletion reduced the average oligomeric state of NET. Similarly, studies on SERT reported a direct contribution of PIP₂ to dimer stabilization [53]. In contrast, no PIP₂ dependence of dimer formation was observed for DAT [54], which is consistent with our DAT simulations where PIP₂ does not preferentially localize to the detected interface regions.

Interestingly, we also observe differences in protomer density hotspot-strength across systems with different PIP₂ levels. The Avg membrane condition with the highest PIP₂ fraction exhibits lower apparent dimer stability than conditions with more moderate PIP₂ content (Avg without interface PI and the Neuron system). At present, we interpret this trend cautiously. One possible explanation is that there is an optimum of PIP₂ concentration in the membrane for dimer formation. Such an effect could arise if elevated PIP₂ promotes self-clustering, potentially reducing the fraction of PIP₂ that is available for persistent interactions with the transporter. Electrostatics-driven PIP₂ clustering has been reported and can be influenced by cations such as Na⁺ [93]. However, this interpretation remains speculative and a dedicated follow-up analysis quantifying PIP₂ clustering and residence near relevant protein surfaces would be required to evaluate this mechanism in our systems.

5.3. Palmitoylation effects on interface preferences

In this work, palmitoylation did not act as a generic stabilizer of MAT dimers. Instead, the primary effect observed was a shift in *interface preference*, and this shift depended on both the membrane composition and the investigated transporter. For NET, palmitoylation tended to increase the relative prevalence of TM12-involving interfaces in several membrane models with decreased replica-to-replica variability, whereas for DAT the corresponding palmitoylated systems showed reduced TM12 contact frequencies with higher replica-to-replica variability. Thus, within our model, palmitoylation modulates which interface families are populated rather than enforcing a single, more stable dimer state.

Membrane dependence of palmitoylation effects. A key observation is that palmitoylation-dependent shifts were not uniform across membrane models. In the pure POPC/CHOL system (Simp), differences between non-palmitoylated and palmitoylated conditions were minor, whereas in complex membrane environments

the TM-TM contact matrices and the Welch-test statistics indicated clearer shifts in specific helix-pair contacts.

Opposite trends for NET and DAT. The opposite direction of TM12-associated contact changes in NET versus DAT suggests that palmitoylation does not impose a universal interface rule across MATs, even though these transporters share a conserved fold. One explanation is that the same modification can couple differently to the interface landscape depending on sequence- and structure-specific features and, critically, on the baseline interface preferences favored in each system. In DAT, prior coarse-grained self-assembly work reported that palmitoylation has only modest effects on interhelical contact patterns in simple membranes, and that TM12-associated interfaces can be shifted in abundance rather than being stabilized [20]. This aligns with the qualitative picture emerging from our Simp systems and supports the interpretation that palmitoylation can be an interface modulator.

5.4. General limitations in the study design and analysis methods

Palmitoylation site selection and physiological interpretation. A critical limitation for interpreting NET-specific palmitoylation effects is the palmitoylation site used in this study. NET was palmitoylated at residue 578 (Leu to Cys substitution followed by palmitoylation) to mirror the major DAT palmitoylation site at Cys581 [9]. More recent evidence suggests that NET is predominantly palmitoylated at a different site (Cys44) [8]. Therefore, while the simulations provide insight into how a palmitoylation event in proximity to TM12 may modulate dimer interface preferences, the results cannot be directly interpreted as the physiological effect of NET palmitoylation on dimerization. Nevertheless, the observed trends remain informative for understanding how palmitoylation near TM12 can reshape the interface landscape, which may be more directly relevant to DAT.

Potential artefacts from extracellular leaflet PI. Another limitation concerns the physiological plausibility of PI in the extracellular leaflet. While early work in red blood cells reported a substantial fraction of PI in the outer leaflet [94], more recent studies have argued that PI can be unexpectedly rare in the plasma membrane overall [95], making an extracellular PI pool unlikely, especially in MAT-relevant cell types such as neurons. In systems that included cryo-EM-derived PI, density maps suggested PI occupancy in regions overlapping with PIP₂ binding hotspots. For intracellular PI, such overlap is not inherently problematic; however,

if PI is effectively present in the extracellular leaflet in the model, it could bias protein-lipid interactions and thereby influence which dimer interfaces are favored. This concern is particularly relevant because the Avg (no interface-PI) system exhibited distinct interface preferences, suggesting that the presence or absence of these interface-associated lipids can reshape the interface landscape. Further analysis should explicitly quantify whether any PI molecules reside in the extracellular leaflet and whether they participate in the dimer interface, and subsequent studies should consider restricting PI placement to the intracellular leaflet.

Limitations of interface characterization methods. In addition to limitations of the study design, the analysis methods used here impose constraints on how interfaces can be identified and compared. For the 2D density maps, a single interface can give rise to multiple apparent hotspots because the dimer geometries are not symmetric. For example, an interface involving TM12 of the fixed protomer contacting TM4 of the mobile protomer is equivalent to the swapped assignment (TM4 of the fixed protomer contacting TM12 of the mobile protomer), yet these cases can produce distinct hotspots in the current representation. As a result, density-based occupancy patterns may project one interface into several hotspot regions.

A second limitation concerns the use of pairwise TM-TM contact matrices to characterize interfaces. Due to the geometry of the transporter, the interfaces can involve multiple helices simultaneously and may shift subtly over time, such that reducing the interaction to single helix pairs can yield a comparatively noisy or fragmented description. Moreover, the contact matrices report absolute contact occupancies, which do not necessarily capture the full interface geometry or distinguish between closely related interface variants that share the same dominant TM contacts.

A more direct approach is to cluster dimer conformations based on structural similarity of the entire complex. For example, Zeppelin et al. [20] complemented contact-based analysis with GROMOS clustering [96], which groups conformations by RMSD using a defined cutoff. This enables objectively similar dimer arrangements to be assigned to the same structural cluster, facilitating a clearer classification of interface populations. Applying such clustering-based analysis to the present trajectories could provide a more time-resolved characterization of interface dynamics and support more robust comparisons between interface populations.

Need for atomistic validation and the role of CG constraints. Finally, resolving the mechanistic basis of palmitoylation-induced interface shifts will likely require atomistic validation. In the present CG setup, the elastic network stabilizes tertiary structure, which hinders conformational adjustments that may accompany

palmitoylation as helix tilt changes or rearrangements near the modified cysteine.

If palmitoylation employs part of its effect through local structural adaptation, the rigidity of the proteins tertiary structure could bias the response toward alternative global motions (such as changes in relative protomer orientation) rather than local accommodation. For this reason, complementary all-atom simulations would be valuable to test the persistence and lipid mediation of representative high-occupancy CG interface states (e.g., TM3/4-TM12 or TM4-TM4 associated interfaces) and to identify local structural signatures that could rationalize the interface shifts observed here. Together, such validation would help to eliminate the concern whether the membrane- and transporter-dependent palmitoylation trends observed in MARTINI3 arise primarily from CG force-field limitations.

6. Conclusion

This thesis investigated whether palmitoylation can modulate dimerization of monoamine transporters in a membrane- and transporter-dependent manner. For this purpose, coarse-grained MARTINI3 dimer simulations of NET and DAT were performed in palmitoylated and non-palmitoylated states across multiple membrane models, and dimer occupancy and interface properties were quantified using RMSD, 2D density maps, and helix-helix and lipid contact analyses.

Across all membrane environments, the cryo-EM-derived NET dimer arrangement did not remain stable once restraints were released. The relative position of the two protomers departed from the initial geometry within the first microseconds, accompanied by loss of the initial interface-lipid arrangement. Importantly, this observation reflects stability within the present coarse-grained model and simulation protocol. It remains plausible that limitations of the MARTINI3 representation and/or the applied CG constraints contribute to this behavior. At the same time, the result is consistent with the possibility that the experimental nanodisc environment stabilizes the interface captured by cryo-EM. Despite the instability of the cryo-EM geometry, the simulations consistently reached alternative, metastable dimer configurations. These interfaces were not uniformly distributed across the transporter surface, as contacts involving bundle-domain helices were rare, whereas interface patterns preferentially involved scaffold-domain helices and, most prominently, TM12, with helix preferences depending on membrane composition and transporter identity. A key outcome is that membrane composition modulates interface selection, as transitions from a simple POPC/CHOL membrane to complex asymmetric membranes altered both protomer occupancy hotspots and the dominant TM-TM contact patterns. With respect to palmitoylation, the data does not support a role as a generic dimer stabilizer. Instead, palmitoylation primarily acted as an interface modulator, shifting the relative prevalence of interface families. In NET, palmitoylation tended to increase the prevalence of TM12-involving interfaces and often reduced replica-to-replica variability, whereas in DAT the direction of TM12-associated changes was frequently opposite and variability increased. Notably, interfaces involving TM3 and TM4 with TM12 were enhanced upon palmitoylation. Given the proximity of the palmitoylation site to TM12, these findings are consistent with a correlation between palmitoylation and TM12-associated interface formation, although the atomistic mechanisms underlying this effect cannot be resolved at coarse-grained resolution. Several

limitations constrain the physiological interpretation of these conclusions. Most importantly, the NET palmitoylation modeled here was introduced near TM12 to mirror the major DAT palmitoylation site, whereas experimental evidence suggests that NET is predominantly palmitoylated at Cys44. NET-specific palmitoylation results should therefore be interpreted as the effect of a TM12-proximal palmitoylation event rather than direct NET physiology. Additional caveats include potential artefacts from PI leaflet placement and the limited structural adaptability imposed by elastic-network CG models.

Future work could test the cryo-EM dimer in a nanodisc-like simulation context under comparable CG conditions and perform atomistic validation by backmapping representative high-occupancy CG interface states (and/or the restrained cryo-EM arrangement prior to release) to assess persistence and lipid mediation at higher resolution.

Overall, this work supports a picture in which MAT dimerization is best described as an ensemble of membrane-dependent interface populations, and in which palmitoylation reshapes this ensemble rather than enforcing a single universally stabilized dimer state.

Bibliography

- [1] Shaili Aggarwal and Ole V Mortensen. “Overview of monoamine transporters”. In: *Current Protocols in Pharmacology* 79.1 (2017), 12.16.1–12.16.17.
- [2] Akula Bala Pramod et al. “SLC6 transporters: structure, function, regulation, disease association and therapeutics”. In: *Molecular Aspects of Medicine* 34.2-3 (2013), 197–219.
- [3] Lindsay C Czuba, Kathleen M Hillgren, and Peter W Swaan. “Post-translational modifications of transporters”. In: *Pharmacology & Therapeutics* 192 (2018), 88–99.
- [4] Yuan Yuan et al. “Protein lipidation in health and disease: molecular basis, physiological function and pathological implication”. In: *Signal Transduction and Targeted Therapy* 9.1 (2024), 60.
- [5] Francisco S. Mesquita et al. “Mechanisms and functions of protein S-acylation”. In: *Nature Reviews Molecular Cell Biology* 25.6 (2024), 488–509.
- [6] James D Foster and Roxanne A Vaughan. “Palmitoylation controls dopamine transporter kinetics, degradation, and protein kinase C-dependent regulation”. In: *Journal of Biological Chemistry* 286.7 (2011), 5175–5186.
- [7] Christopher R Brown and James D Foster. “Palmitoylation regulates human serotonin transporter activity, trafficking, and expression and is modulated by escitalopram”. In: *ACS Chemical Neuroscience* 14.18 (2023), 3431–3443.
- [8] Christopher R Brown, Madhur Shetty, and James D Foster. “Palmitoylation regulates norepinephrine transporter uptake, surface localization, and total expression with pathogenic implications in postural orthostatic tachycardia syndrome”. In: *Journal of Neurochemistry* 169.2 (2025), e16241.
- [9] Danielle E Bolland et al. “Palmitoylation by multiple DHHC enzymes enhances dopamine transporter function and stability”. In: *ACS Chemical Neuroscience* 10.6 (2019), 2707–2717.
- [10] Arnav Paul and Diwakar Shukla. “Oligomerization of Monoamine Transporters”. In: *Macromolecular Protein Complexes V: Structure and Function* (2024), 119–137.

- [11] Cody A Siciliano et al. “Amphetamine reverses escalated cocaine intake via restoration of dopamine transporter conformation”. In: *Journal of Neuroscience* 38.2 (2018), 484–497.
- [12] Cristina Cecchetti, Euan Pyle, and Bernadette Byrne. “Transporter oligomerisation: roles in structure and function”. In: *Biochemical Society Transactions* 47.1 (2019), 433–440.
- [13] Heng Zhang et al. “Dimerization and antidepressant recognition at norepinephrine transporter”. In: *Nature* 630.8015 (2024), 247–254.
- [14] Jacob Andersen et al. “Binding site residues control inhibitor selectivity in the human norepinephrine transporter but not in the human dopamine transporter”. In: *Scientific Reports* 5.1 (2015), 15650.
- [15] Carolyn G Sweeney et al. “Dopamine transporter amino and carboxyl termini synergistically contribute to substrate and inhibitor affinities”. In: *Journal of Biological Chemistry* 292.4 (2017), 1302–1309.
- [16] Kumaresan Jayaraman et al. “SLC6 transporter oligomerization”. In: *Journal of Neurochemistry* 157.4 (2021), 919–929.
- [17] Kumaresan Jayaraman et al. “Dopamine transporter oligomerization involves the scaffold domain, but spares the bundle domain”. In: *PLoS Computational Biology* 14.6 (2018), e1006229.
- [18] Satinder K Singh et al. “A competitive inhibitor traps LeuT in an open-to-out conformation”. In: *Science* 322.5908 (2008), 1655–1661.
- [19] Xavier Periole, Talia Zeppelin, and Birgit Schiøtt. “Dimer interface of the human serotonin transporter and effect of the membrane composition”. In: *Scientific Reports* 8.1 (2018), 5080.
- [20] Talia Zeppelin et al. “Effect of palmitoylation on the dimer formation of the human dopamine transporter”. In: *Scientific Reports* 11.1 (2021), 4164.
- [21] Marilyn D Resh. “Lipid modification of proteins”. In: *Biochemistry of Lipids, Lipoproteins and Membranes*. Elsevier, 2021, pp. 429–456.
- [22] Mingli Li, Leisi Zhang, and Chun-Wei Chen. “Diverse roles of protein palmitoylation in cancer progression, immunity, stemness, and beyond”. In: *Cells* 12.18 (2023), 2209.
- [23] Benjamin C Jennings and Maurine E Linder. “DHHC protein S-acyltransferases use similar ping-pong kinetic mechanisms but display different acyl-CoA specificities”. In: *Journal of Biological Chemistry* 287.10 (2012), 7236–7245.
- [24] Ruth Zeidman, Caroline S Jackson, and Anthony I Magee. “Protein acyl thioesterases”. In: *Molecular Membrane Biology* 26.1-2 (2009), 32–41.

- [25] Yan-Ran Qian, Yu-Jia Zhao, and Feng Zhang. “Protein palmitoylation: biological functions, disease, and therapeutic targets”. In: *MedComm* 6.3 (2025), e70096.
- [26] Justyna Korycka et al. “Human DHHC proteins: a spotlight on the hidden player of palmitoylation”. In: *European Journal of Cell Biology* 91.2 (2012), 107–117.
- [27] Colin D Gottlieb and Maurine E Linder. “Structure and function of DHHC protein S-acyltransferases”. In: *Biochemical Society Transactions* 45.4 (2017), 923–928.
- [28] Ayelén González Montoro, Rodrigo Quiroga, and Javier Valdez Taubas. “Zinc co-ordination by the DHHC cysteine-rich domain of the palmitoyltransferase Swf1”. In: *Biochemical Journal* 454.3 (2013), 427–435.
- [29] Dahvid Davda and Brent R Martin. “Acyl protein thioesterase inhibitors as probes of dynamic S-palmitoylation”. In: *MedChemComm* 5.3 (2014), 268–276.
- [30] Hanqing Li et al. “Role of S-palmitoylation in digestive system diseases”. In: *Cell Death Discovery* 11.1 (2025), 331.
- [31] Dan Liao et al. “The role of s-palmitoylation in neurological diseases: implication for zDHHC family”. In: *Frontiers in Pharmacology* 14 (2024), 1342830.
- [32] Matthew H Bailey et al. “Comprehensive characterization of cancer driver genes and mutations”. In: *Cell* 173.2 (2018), 371–385.
- [33] Peisu Zhang et al. “Senolytic therapy alleviates A β -associated oligodendrocyte progenitor cell senescence and cognitive deficits in an Alzheimer’s disease model”. In: *Nature Neuroscience* 22.5 (2019), 719–728.
- [34] Douglas M Lopes, Sophie K Llewellyn, and Ian F Harrison. “Propagation of tau and α -synuclein in the brain: therapeutic potential of the glymphatic system”. In: *Translational Neurodegeneration* 11.1 (2022), 19.
- [35] Fanny L Lemarié et al. “Rescue of aberrant huntingtin palmitoylation ameliorates mutant huntingtin-induced toxicity”. In: *Neurobiology of Disease* 158 (2021), 105479.
- [36] Anita L Pinner et al. “Protein expression of prenyltransferase subunits in postmortem schizophrenia dorsolateral prefrontal cortex”. In: *Translational Psychiatry* 10.1 (2020), 3.
- [37] Vanessa K Ota et al. “ZDHHC8 gene may play a role in cortical volumes of patients with schizophrenia”. In: *Schizophrenia Research* 145.1-3 (2013), 33–35.

- [38] Danielle E Rastedt, Roxanne A Vaughan, and James D Foster. “Palmitoylation mechanisms in dopamine transporter regulation”. In: *Journal of Chemical Neuroanatomy* 83 (2017), 3–9.
- [39] Rebeca Mejias et al. “Increased novelty-induced locomotion, sensitivity to amphetamine, and extracellular dopamine in striatum of *Zdhhc 15*-deficient mice”. In: *Translational Psychiatry* 11.1 (2021), 65.
- [40] Francisco S Mesquita et al. “S-acylation controls SARS-CoV-2 membrane lipid organization and enhances infectivity”. In: *Developmental Cell* 56.20 (2021), 2790–2807.
- [41] Shaili Aggarwal and Ole Valente Mortensen. “Discovery and development of monoamine transporter ligands”. In: *Drug Development in Psychiatry* (2023), 101–129.
- [42] Mary Hongying Cheng and Ivet Bahar. “Monoamine transporters: structure, intrinsic dynamics and allosteric regulation”. In: *Nature Structural & Molecular Biology* 26.7 (2019), 545–556.
- [43] Tianyu Wang et al. “SLC6 transporters as pharmacological targets in depression: Molecular mechanisms and therapeutic strategies”. In: *Biochemical Pharmacology* (2025), 117210.
- [44] H. Zhang, E. H. Xu, and Y. Jiang. *Structure of NET-Nisoxetine in outward-open state*. PDB ID: 8YR2, accessed 2025-12-17. 2024. URL: <https://doi.org/10.2210/pdb8YR2/pdb>.
- [45] Jacob A Licht et al. “They all rock: A systematic comparison of conformational movements in LeuT-fold transporters”. In: *Structure* 32.9 (2024), 1528–1543.
- [46] Gary Rudnick et al. “The SLC6 transporters: perspectives on structure, functions, regulation, and models for transporter dysfunction”. In: *Pflügers Archiv-European Journal of Physiology* 466.1 (2014), 25–42.
- [47] Nadia Ayala-Lopez and Stephanie W Watts. “Physiology and pharmacology of neurotransmitter transporters”. In: *Comprehensive Physiology* 11.3 (2021), 2279–2295.
- [48] Kana Harada et al. “S-Palmitoylation of the serotonin transporter promotes its cell surface expression and serotonin uptake”. In: *Biochemical and Biophysical Research Communications* 662 (2023), 58–65.
- [49] Isaiah T Arkin. “Structural aspects of oligomerization taking place between the transmembrane α -helices of bitopic membrane proteins”. In: *Biochimica et Biophysica Acta (BBA)-Biomembranes* 1565.2 (2002), 347–363.

- [50] Urda Jess, Heinrich Betz, and Patrick Schloss. “The membrane-bound rat serotonin transporter, SERT1, is an oligomeric protein”. In: *FEBS Letters* 394.1 (1996), 44–46.
- [51] S Paul Berger et al. “Radiation inactivation studies of the dopamine reuptake transporter protein.” In: *Molecular Pharmacology* 46.4 (1994), 726–731.
- [52] Manuel Moertelmaier et al. “Thinning out clusters while conserving stoichiometry of labeling”. In: *Applied Physics Letters* 87.26 (2005), 263903.
- [53] Andreas Anderluh et al. “Direct PIP2 binding mediates stable oligomer formation of the serotonin transporter”. In: *Nature Communications* 8.1 (2017), 14089.
- [54] Anand Kant Das et al. “Dopamine transporter forms stable dimers in the live cell plasma membrane in a phosphatidylinositol 4, 5-bisphosphate-independent manner”. In: *Journal of Biological Chemistry* 294.14 (2019), 5632–5642.
- [55] Dino Luethi et al. “Phosphatidylinositol 4, 5-bisphosphate (PIP2) facilitates norepinephrine transporter dimerization and modulates substrate efflux”. In: *Communications Biology* 5.1 (2022), 1259.
- [56] Mohammad Sufian Badar et al. “Molecular dynamics simulations: concept, methods, and applications”. In: *Transdisciplinarity*. Springer, 2022, pp. 131–151.
- [57] M. Born and R. Oppenheimer. “Zur Quantentheorie der Molekeln”. In: *Annalen der Physik* 389.20 (1927), 457–484.
- [58] Andrew R Leach. *Molecular modelling: principles and applications*. Pearson education, 2001.
- [59] Diego Milardovich. “Bridging molecular dynamics and neuroscience: Machine learning for efficient simulations and biomedical signal processing”. PhD thesis. Technische Universität Wien, 2024.
- [60] Sachin Patodia, Ashima Bagaria, and Deepak Chopra. “Molecular dynamics simulation of proteins: a brief overview”. In: *Journal of Physical Chemistry & Biophysics* 4.6 (2014), 1–4.
- [61] Outi MH Salo-Ahen et al. “Molecular dynamics simulations in drug discovery and pharmaceutical development”. In: *Processes* 9.1 (2020), 71.
- [62] Helen M Berman et al. “The protein data bank”. In: *Nucleic Acids Research* 28.1 (2000), 235–242.
- [63] Haoran Yu and Paul A Dalby. “A beginner’s guide to molecular dynamics simulations and the identification of cross-correlation networks for enzyme engineering”. In: *Methods in Enzymology*. Vol. 643. Elsevier, 2020, pp. 15–49.

- [64] Kenneth Goossens and Hans De Winter. “Molecular dynamics simulations of membrane proteins: An overview”. In: *Journal of Chemical Information and Modeling* 58.11 (2018), 2193–2202.
- [65] Soumil Y Joshi and Sanket A Deshmukh. “A review of advancements in coarse-grained molecular dynamics simulations”. In: *Molecular Simulation* 47.10-11 (2021), 786–803.
- [66] Adam Liwo et al. “Theory and practice of coarse-grained molecular dynamics of biologically important systems”. In: *Biomolecules* 11.9 (2021), 1347.
- [67] Siewert J Marrink et al. “The MARTINI force field: coarse grained model for biomolecular simulations”. In: *The Journal of Physical Chemistry B* 111.27 (2007), 7812–7824.
- [68] Paulo CT Souza et al. “Martini 3: a general purpose force field for coarse-grained molecular dynamics”. In: *Nature Methods* 18.4 (2021), 382–388.
- [69] Luís Borges-Araújo et al. “Martini 3 coarse-grained force field for cholesterol”. In: *Journal of Chemical Theory and Computation* 19.20 (2023), 7387–7404.
- [70] Xavier Periole et al. “Combining an elastic network with a coarse-grained molecular force field: structure, dynamics, and intermolecular recognition”. In: *Journal of Chemical Theory and Computation* 5.9 (2009), 2531–2543.
- [71] Jeppe C Nielsen et al. “Structure of the human dopamine transporter in complex with cocaine”. In: *Nature* 632.8025 (2024), 678–685.
- [72] J. C. Nielsen et al. *Outward-open structure of human dopamine transporter bound to cocaine*. PDB ID: 9EO4, accessed 2025-12-17. 2024. URL: <https://doi.org/10.2210/pdb9eo4/pdb>.
- [73] Andrei L Lomize, Spencer C Todd, and Irina D Pogozheva. “Spatial arrangement of proteins in planar and curved membranes by PPM 3.0”. In: *Protein Science* 31.1 (2022), 209–220.
- [74] Peter C Kroon et al. “Martinize2 and Vermouth provide a unified framework for molecular topology generation”. In: *eLife* 12 (2025), RP90627.
- [75] Robert T McGibbon et al. “MDTraj: a modern open library for the analysis of molecular dynamics trajectories”. In: *Biophysical Journal* 109.8 (2015), 1528–1532.
- [76] Tsjerk A Wassenaar et al. “Computational lipidomics with insane: a versatile tool for generating custom membranes for molecular simulations”. In: *Journal of Chemical Theory and Computation* 11.5 (2015), 2144–2155.
- [77] Helgi I Ingólfsson et al. “Capturing biologically complex tissue-specific membranes at different levels of compositional complexity”. In: *The Journal of Physical Chemistry B* 124.36 (2020), 7819–7829.

- [78] Helgi I Ingólfsson. *M3-Lipid-Parameters*. GitHub repository. Commit 2121527; accessed 2025-12-17. 2025. URL: <https://github.com/Martini-Force-Field-Initiative/M3-Lipid-Parameters/tree/2121527045696345069deb4d3df754724888a4f9>.
- [79] Schrödinger, LLC. “The PyMOL Molecular Graphics System, Version 1.8”. Nov. 2015.
- [80] Luís Borges-Araújo et al. “Improved parameterization of phosphatidylinositol lipid headgroups for the martini 3 coarse-grain force field”. In: *Journal of Chemical Theory and Computation* 18.1 (2021), 357–373.
- [81] Sunhwan Jo et al. “CHARMM-GUI: a web-based graphical user interface for CHARMM”. In: *Journal of Computational Chemistry* 29.11 (2008), 1859–1865.
- [82] Sang-Jun Park et al. “CHARMM-GUI PDB manipulator: various PDB structural modifications for biomolecular modeling and simulation”. In: *Journal of Molecular Biology* 435.14 (2023), 167995.
- [83] Panagiotis I Koukos et al. “Martini 3 force field parameters for protein lipitation post-translational modifications”. In: *Journal of Chemical Theory and Computation* 19.23 (2023), 8901–8918.
- [84] Benjamin Webb and Andrej Sali. “Comparative protein structure modeling using MODELLER”. In: *Current Protocols in Bioinformatics* 54.1 (2016), 5.6.1–5.6.37.
- [85] Mark Abraham et al. *GROMACS 2024.4 Source code*. Version 2024.4. accessed 2025-12-17. 2024. DOI: 10.5281/zenodo.14016590. URL: <https://doi.org/10.5281/zenodo.14016590>.
- [86] Mark James Abraham et al. “GROMACS: High performance molecular simulations through multi-level parallelism from laptops to supercomputers”. In: *SoftwareX* 1 (2015), 19–25.
- [87] Kasper B Pedersen et al. “The Martini 3 lipidome: expanded and refined parameters improve lipid phase behavior”. In: *ACS Central Science* 11.9 (2025), 1598–1610.
- [88] Naveen Michaud-Agrawal et al. “MDAnalysis: a toolkit for the analysis of molecular dynamics simulations”. In: *Journal of Computational Chemistry* 32.10 (2011), 2319–2327.
- [89] Bernard L Welch. “The generalization of ‘Student’s’ problem when several different population variances are involved”. In: *Biometrika* 34.1-2 (1947), 28–35.

- [90] Riccardo Alessandri et al. “Pitfalls of the Martini model”. In: *Journal of Chemical Theory and Computation* 15.10 (2019), 5448–5460.
- [91] Jonas Binder et al. “Enhancing Martini 3 for protein self-interaction simulations”. In: *European Journal of Pharmaceutical Sciences* 209 (2025), 107068.
- [92] Lisbeth R Kjølbye et al. “General protocol for constructing molecular models of nanodiscs”. In: *Journal of Chemical Information and Modeling* 61.6 (2021), 2869–2883.
- [93] Kyungreem Han, Arne Gericke, and Richard W Pastor. “Characterization of specific ion effects on PI (4, 5) P2 clustering: molecular dynamics simulations and graph-theoretic analysis”. In: *The Journal of Physical Chemistry B* 124.7 (2020), 1183–1196.
- [94] P Bütikofer et al. “Transbilayer distribution and mobility of phosphatidylinositol in human red blood cells.” In: *Journal of Biological Chemistry* 265.27 (1990), 16035–16038.
- [95] James P Zewe et al. “Probing the subcellular distribution of phosphatidylinositol reveals a surprising lack at the plasma membrane”. In: *Journal of Cell Biology* 219.3 (2020).
- [96] Xavier Daura et al. “Peptide folding: when simulation meets experiment”. In: *Angewandte Chemie International Edition* 38.1-2 (1999), 236–240.

List of Abbreviations

ABHD	α/β -hydrolase domain
ADHD	attention deficit hyperactivity disorder
APT	acyl-protein thioesterases
ATP	adenosine triphosphate
CG	coarse-graining
cryo-EM	cryo electron microscopy
DAT	dopamine transporter
LeuT	leucine transporter
MAT	monoamine transporter
MD	molecular dynamics
MDMA	3,4-methylenedioxymethamphetamine
NET	norepinephrine transporter
nonpalm	non-palmitoylated
NPT	isothermal-isobaric
palm	palmitoylated
PAT	protein acyltransferases
PBC	periodic boundary condition
PDB	Protein Data Bank
PI	phosphatidylinositol
PIP ₂	phosphatidylinositol 4,5-bisphosphate
POPC	1-Palmitoyl-2-oleoyl-glycero-3-phosphocholine
PPT	palmitoyl-protein thioesterase
RMSD	root mean square deviation
SERT	serotonin transporter
SLC6	solute carrier 6

TM	transmembrane helix
TOCCSL	thinning out clusters while conserving stoichiometry of labeling
V_{\max}	maximal uptake velocity

List of Figures

2.1.	The reversible palmitoylation cycle	3
2.2.	Two-step ping-pong mechanism of DHHC-mediated palmitoylation .	4
2.3.	Consequences of palmitoylation (three tiers)	6
2.4.	Topology and structure of monoamine transporters	9
2.5.	Oligomerization interfaces and MAT transport	13
2.6.	Basic MD simulation algorithm	15
2.7.	MARTINI3 mapping illustrated for cholesterol	17
3.1.	MD simulation protocol	22
4.1.	RMSD of the flexible protomer relative to the first production frame for all systems	28
4.2.	RMSD of cryo-EM-derived cholesterol molecules in Neuron-nonpalm	29
4.3.	RMSD of cryo-EM-derived PIP ₂ molecules in Avg-nonpalm	30
4.4.	RMSD of cryo-EM-derived PI molecules in Neuron-nonpalm	30
4.5.	Density map of the flexible protomer in the x - y plane (extracellular top view) for each system, averaged over all repeats	32
4.6.	Density map of all PIP ₂ molecules in the x - y plane (extracellular top view) for each system containing PIP ₂ , averaged over all repeats	33
4.7.	Density map of PI molecules in the x - y plane (extracellular top view) for each system containing PI, averaged over all repeats	34
4.8.	TM contact matrix of the initial NET dimer configuration	35
4.9.	TM contact matrices for all systems (contacts per frame)	36
4.10.	Difference of TM contact matrices (palm - nonpalm) for each system (Contacts per frame)	36
4.11.	Box-whisker plots comparing nonpalm and palm replica-wise con- tact frequencies for selected TM interfaces	37
4.12.	Scaled lipid headgroup contacts at the palmitoylation site shown as violin plots across replicas for each system and condition	38
A.1.	Cholesterol RMSD traces (1)	64
A.2.	Cholesterol RMSD traces (2)	65
A.3.	PIP ₂ RMSD traces	66
A.4.	PI RMSD traces	67

A.5. Density map of cholesterol molecules in the x - y plane (extracellular top view) for each system, averaged over all repeats	72
A.6. Simp nonpalm	73
A.7. Simp palm	73

List of Tables

3.1. Membrane leaflet compositions	20
3.2. Overview of simulated systems	21
A.1. Key GROMACS simulation parameters per stage	62
A.2. Martini3 lipid names, tail composition, headgroup class, and full lipid names.	63
A.3. TM-TM contact frequencies (mean(SD)) for Simp non-palmitoylated.	68
A.4. TM-TM contact frequencies (mean(SD)) for Simp palmitoylated. . .	68
A.5. TM-TM contact frequencies (mean(SD)) for Avg non-palmitoylated.	68
A.6. TM-TM contact frequencies (mean(SD)) for Avg palmitoylated. . .	68
A.7. TM-TM contact frequencies (mean(SD)) for Avg (no interface-PI) non-palmitoylated.	69
A.8. TM-TM contact frequencies (mean(SD)) for Avg (no interface-PI) palmitoylated.	69
A.9. TM-TM contact frequencies (mean(SD)) for Neuron non-palmitoylated.	69
A.10. TM-TM contact frequencies (mean(SD)) for Neuron palmitoylated.	69
A.11. TM-TM contact frequencies (mean(SD)) for Avg (DAT) non-palmitoylated.	70
A.12. TM-TM contact frequencies (mean(SD)) for Avg (DAT) palmitoy- lated.	70
A.13. Welch test results per system (sorted by p). t and p are rounded to 3 decimals, and interfaces with $t > 0$ are reported.	71

A. Appendix

A.1. GROMACS parameters

Table A.1.: Key GROMACS simulation parameters per stage, including output and velocity initialization. *Note that EQ0 was only applied for the Avg (DAT) systems.

Stage	Integrator	dt (ps)	Length	POSRES ($\frac{kJ}{molnm^2}$)	Thermostat	Barostat	τ_P (ps)	Δt_{traj}	Gen. vel.
EM	steepest descent (steep)	0.001	75 steps	1000	–	–	–	–	–
*EQ0	leap-frog (md)	0.001	5 ps	1000	Berendsen	Berendsen	10.0	1 ps	no
EQ1	leap-frog (md)	0.005	10 ns	1000	Berendsen	Berendsen	3.0	5 ps	no
EQ2	leap-frog (md)	0.010	10 ns	1000	Berendsen	Berendsen	3.0	10 ps	no
EQ3	leap-frog (md)	0.020	10 ns	1000	v-rescale	c-rescale	4.0	20 ps	no
prePROD	leap-frog (md)	0.020	1 μs	100	v-rescale	c-rescale	4.0	100 ps	yes (310 K)
PROD	leap-frog (md)	0.020	25 μs	–	v-rescale	c-rescale	4.0	100 ps	yes (310 K)

For all MD stages (EQ0-PROD), the temperature coupling time constant was $\tau_T = 1.0$ ps with $T = 310$ K. The pressure was set to $P = 1.0$ bar with semi-isotropic coupling, using a compressibility of $\kappa = 3 \times 10^{-4}$ bar $^{-1}$. Temperature coupling groups were **protein/membrane/solvent**.

Position restraints were applied to all molecules derived from the cryo-EM model, i.e. both protomers, the bound ions (2 Na and 1 Cl per protomer), as well as the bound PIP₂/PI and cholesterol molecules (restraint force constants as indicated in Table A.1).

A.2. Lipid naming conventions

Table A.2.: Martini3 lipid names, tail composition, headgroup class, and full lipid names.

Name	Tails	Headgroup	Full lipid name
POPC	C16:0/18:1	phosphatidylcholine	1-palmitoyl-2-oleoyl-glycero-3-phosphocholine
SSM	C(d18:1/18:0)	sphingomyelin	N-stearoyl-sphingosylphosphorylcholine
SAPI (PI)	C18:0/20:4	phosphatidylinositol	1-stearoyl-2-arachidonoyl-glycero-3-phosphoinositol
PAPC	C16:0/20:4	phosphatidylcholine	1-palmitoyl-2-arachidonoyl-glycero-3-phosphocholine
PAPS	C16:0/20:4	phosphatidylserine	1-palmitoyl-2-arachidonoyl-glycero-3-phosphoserine
DLPE	C18:2/18:2	phosphatidylethanolamine	1,2-dilinoleoyl-glycero-3-phosphoethanolamine
POPE	C16:0/18:1	phosphatidylethanolamine	1-palmitoyl-2-oleoyl-glycero-3-phosphoethanolamine
PAPE	C16:0/20:4	phosphatidylethanolamine	1-palmitoyl-2-arachidonoyl-glycero-3-phosphoethanolamine
SAP6 (PIP2)	C18:0/20:4	phosphatidylinositol-bisphosphate	1-stearoyl-2-arachidonoyl-glycero-3-phosphoinositol-4',5'-bisphosphate
PNPI*	C(d18:1/24:1)	phosphoinositol-(sphingolipid)	N-nervonoyl-sphingosylphosphoryl-inositol

*note that PNPI is not a standard lipid in the Martini 3 force field. It was generated with the script `lipid-ntp-generator-Martini3-01.py` [78] to mimic the glycolipid PNGS, which is not yet parameterized in Martini 3, as described in Section 3.

A.3. RMSD plots

The following figures show RMSD traces relative to the first production frame for the indicated systems and conditions. Individual molecules are shown as separate traces in different colors. A moving average with a window size of 500 frames was applied.

A.3.1. Internal cholesterol

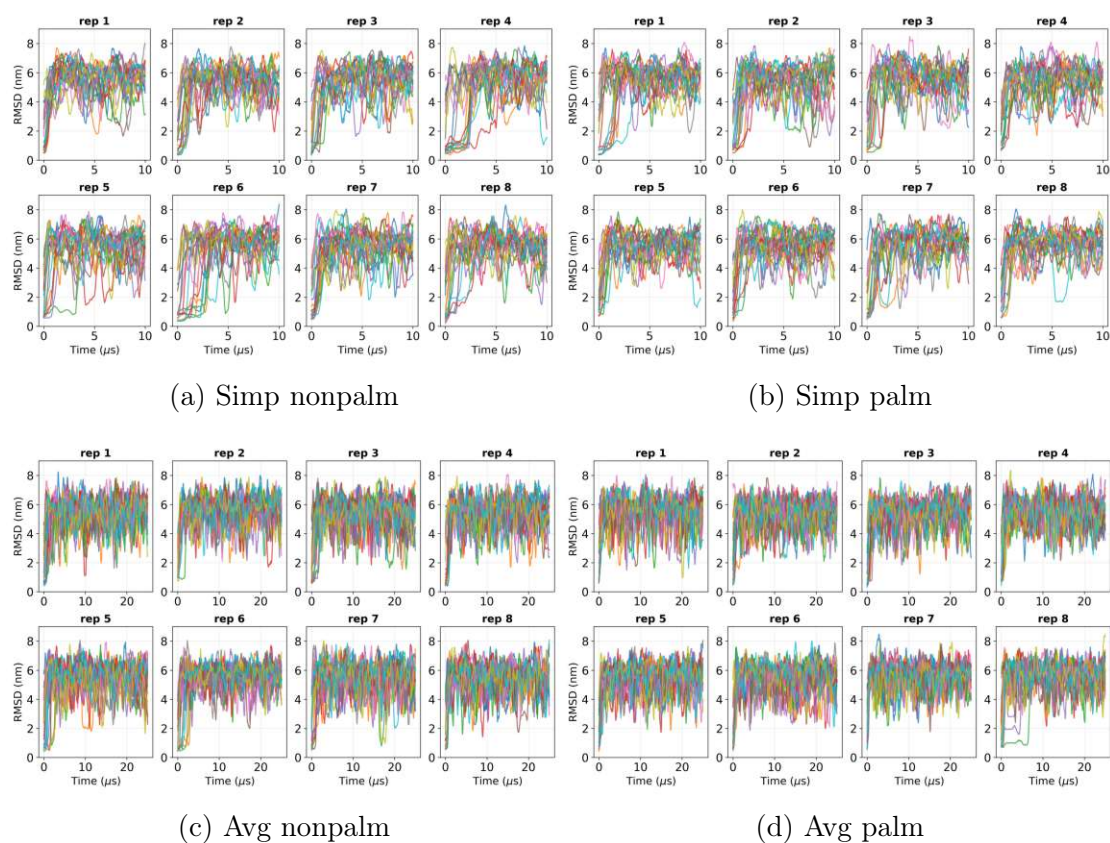
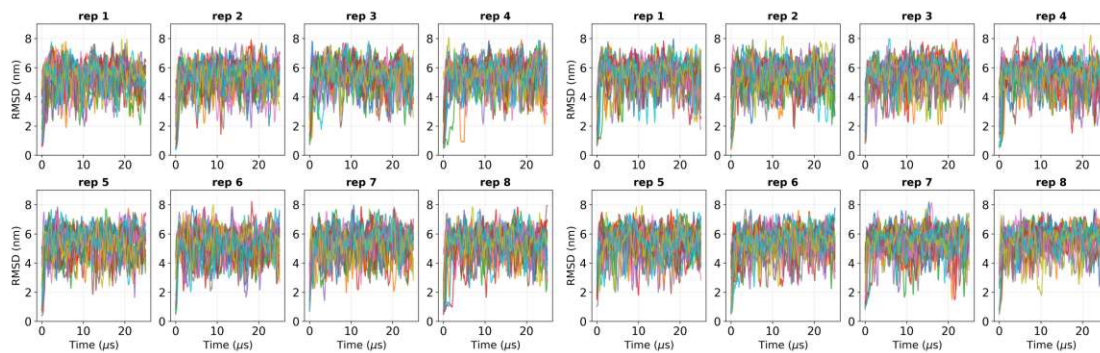
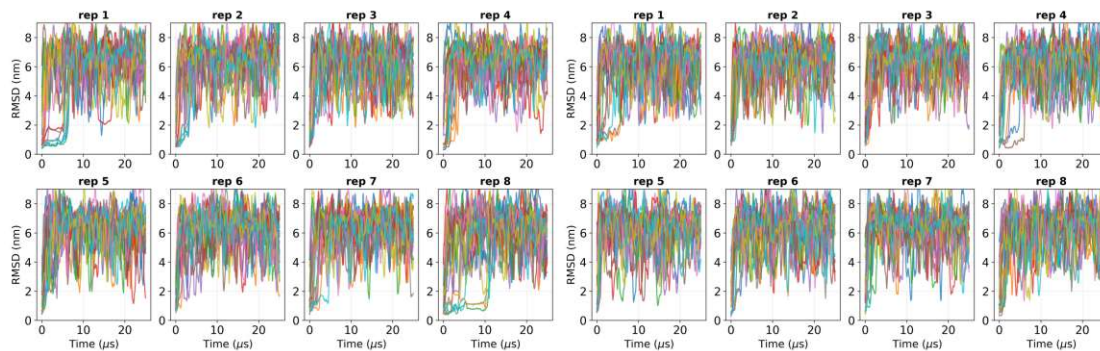


Figure A.1.: RMSD of cryo-EM-derived interface cholesterol molecules (Simp and Avg systems).



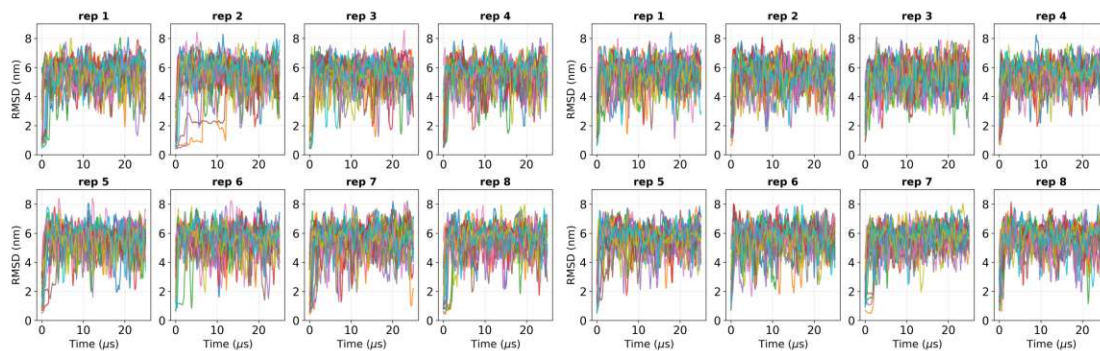
(a) Avg (no interface-PI) nonpalm

(b) Avg (no interface-PI) palm



(c) Neuron nonpalm

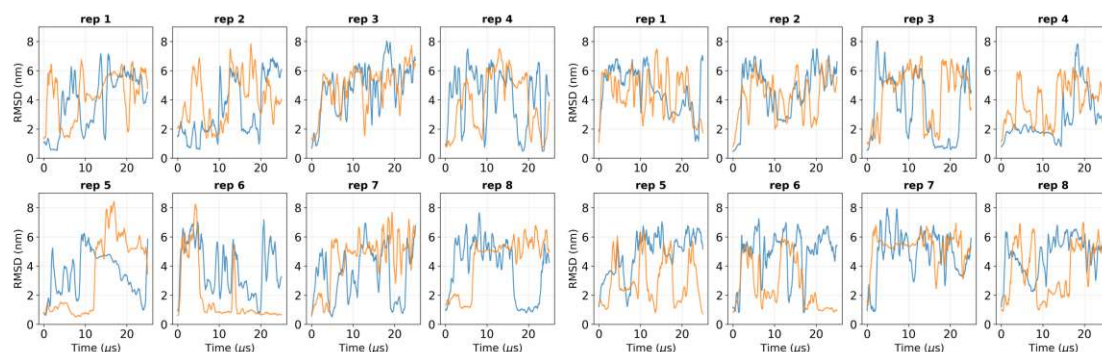
(d) Neuron palm



(e) Avg (DAT) nonpalm

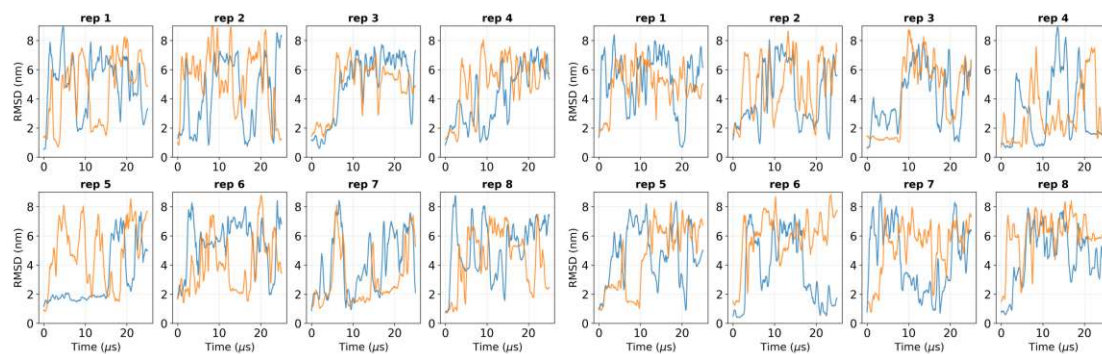
(f) Avg (DAT) palm

Figure A.2.: RMSD of cryo-EM-derived interface cholesterol molecules (remaining systems).

A.3.2. Internal PIP₂

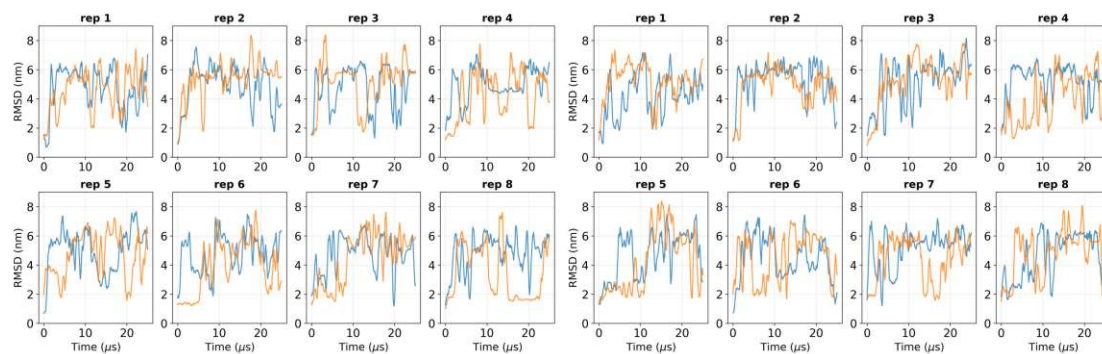
(a) Avg nonpalm

(b) Avg palm



(c) Neuron nonpalm

(d) Neuron palm



(e) Avg (DAT) nonpalm

(f) Avg (DAT) palm

Figure A.3.: RMSD of cryo-EM-derived interface PIP₂ molecules across systems and conditions.

A.3.3. Internal PI

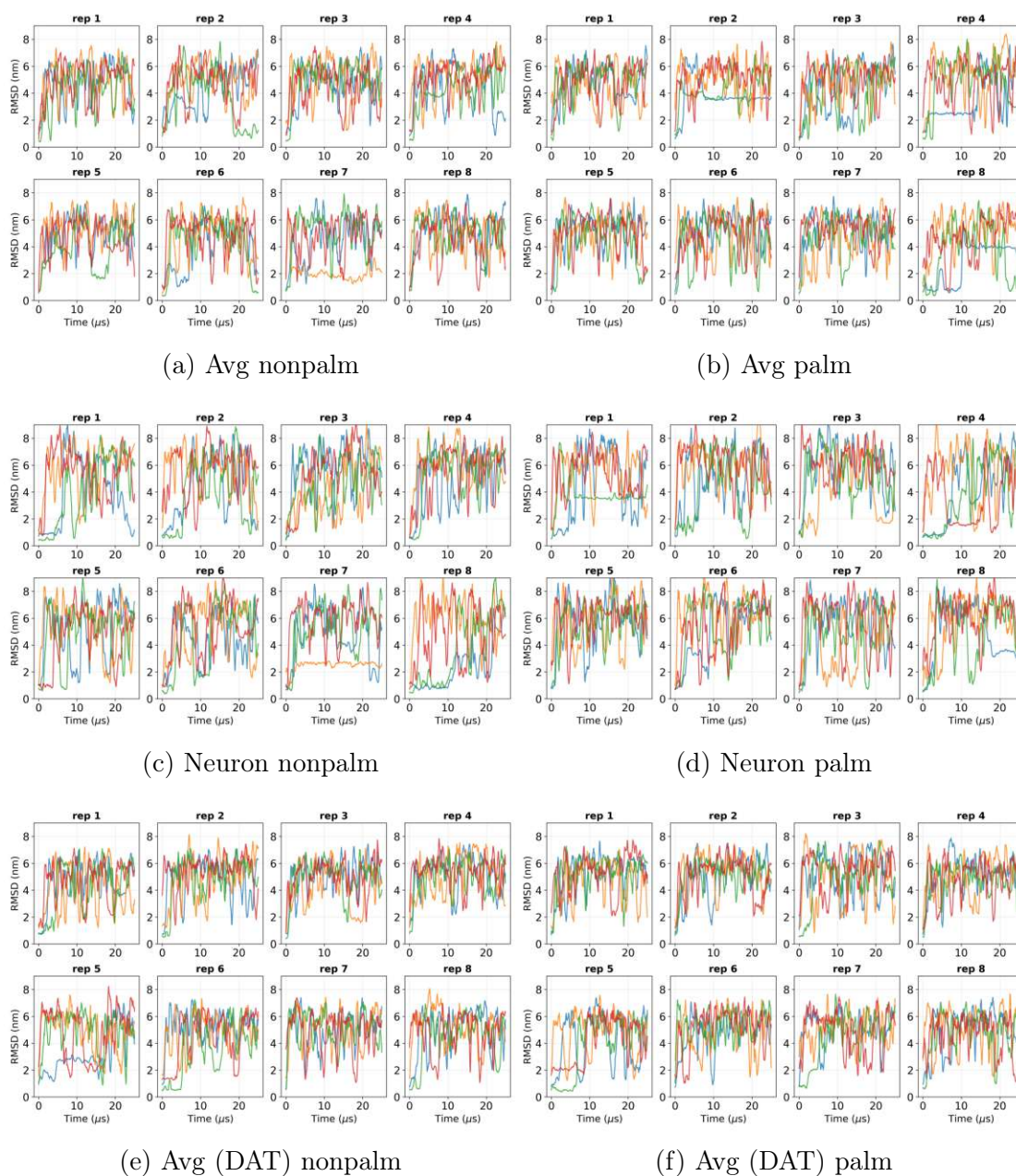


Figure A.4.: RMSD of cryo-EM-derived interface PI molecules across systems and conditions.

A.4. TM-TM contact matrices (mean(SD))

Table A.3.: TM-TM contact frequencies (mean(SD)) for Simp non-palmitoylated.

TM	TM1	TM2	TM3	TM4	TM5	TM6	TM7	TM8	TM9	TM10	TM11	TM12
TM1	0.00(0.00)	0.00(0.00)	0.00(0.00)	0.00(0.00)	0.00(0.00)	0.00(0.00)	0.00(0.00)	0.00(0.00)	0.00(0.00)	0.00(0.00)	0.00(0.00)	0.00(0.00)
TM2	0.00(0.00)	0.00(0.00)	0.00(0.00)	0.00(0.01)	0.00(0.00)	0.00(0.00)	0.00(0.00)	0.00(0.00)	0.00(0.00)	0.00(0.00)	0.00(0.00)	0.00(0.00)
TM3	0.00(0.00)	0.00(0.00)	0.11(0.27)	0.14(0.14)	0.01(0.01)	0.00(0.00)	0.00(0.00)	0.01(0.02)	0.11(0.10)	0.04(0.06)	0.00(0.00)	0.18(0.16)
TM4	0.00(0.00)	0.00(0.01)	0.14(0.14)	0.26(0.29)	0.08(0.22)	0.00(0.01)	0.00(0.00)	0.09(0.24)	0.21(0.23)	0.12(0.11)	0.01(0.01)	0.26(0.17)
TM5	0.00(0.00)	0.00(0.00)	0.01(0.01)	0.08(0.22)	0.00(0.01)	0.00(0.00)	0.00(0.00)	0.00(0.00)	0.02(0.06)	0.00(0.00)	0.00(0.00)	0.01(0.01)
TM6	0.00(0.00)	0.00(0.00)	0.00(0.00)	0.00(0.01)	0.00(0.00)	0.00(0.00)	0.00(0.00)	0.00(0.00)	0.00(0.01)	0.00(0.00)	0.00(0.00)	0.00(0.00)
TM7	0.00(0.00)	0.00(0.00)	0.00(0.01)	0.12(0.14)	0.01(0.01)	0.00(0.00)	0.00(0.00)	0.00(0.00)	0.00(0.00)	0.00(0.00)	0.00(0.00)	0.00(0.00)
TM8	0.00(0.00)	0.00(0.00)	0.01(0.02)	0.09(0.24)	0.00(0.00)	0.00(0.00)	0.00(0.00)	0.00(0.00)	0.00(0.01)	0.00(0.00)	0.00(0.01)	0.09(0.10)
TM9	0.00(0.00)	0.00(0.00)	0.11(0.10)	0.21(0.23)	0.02(0.06)	0.00(0.01)	0.00(0.00)	0.00(0.01)	0.36(0.31)	0.03(0.04)	0.01(0.02)	0.15(0.08)
TM10	0.00(0.00)	0.00(0.00)	0.04(0.06)	0.12(0.11)	0.00(0.00)	0.00(0.00)	0.00(0.00)	0.00(0.00)	0.03(0.04)	0.00(0.00)	0.00(0.01)	0.04(0.09)
TM11	0.00(0.00)	0.00(0.00)	0.00(0.00)	0.01(0.01)	0.00(0.00)	0.00(0.00)	0.00(0.00)	0.00(0.01)	0.01(0.02)	0.00(0.01)	0.00(0.00)	0.03(0.06)
TM12	0.00(0.00)	0.00(0.00)	0.18(0.16)	0.26(0.17)	0.01(0.01)	0.00(0.00)	0.00(0.00)	0.09(0.10)	0.15(0.08)	0.04(0.09)	0.03(0.06)	0.12(0.20)

Table A.4.: TM-TM contact frequencies (mean(SD)) for Simp palmitoylated.

TM	TM1	TM2	TM3	TM4	TM5	TM6	TM7	TM8	TM9	TM10	TM11	TM12
TM1	0.00(0.00)	0.00(0.00)	0.00(0.00)	0.00(0.00)	0.00(0.00)	0.00(0.00)	0.00(0.00)	0.00(0.00)	0.00(0.00)	0.00(0.00)	0.00(0.01)	0.00(0.00)
TM2	0.00(0.00)	0.00(0.00)	0.00(0.00)	0.00(0.00)	0.01(0.01)	0.00(0.00)	0.00(0.00)	0.01(0.01)	0.00(0.00)	0.00(0.00)	0.00(0.00)	0.00(0.00)
TM3	0.00(0.00)	0.00(0.00)	0.00(0.00)	0.12(0.14)	0.01(0.01)	0.00(0.00)	0.00(0.00)	0.00(0.00)	0.12(0.15)	0.05(0.09)	0.01(0.02)	0.20(0.17)
TM4	0.00(0.00)	0.00(0.00)	0.12(0.14)	0.22(0.38)	0.00(0.00)	0.00(0.00)	0.00(0.00)	0.00(0.00)	0.28(0.36)	0.11(0.10)	0.01(0.02)	0.23(0.16)
TM5	0.00(0.00)	0.01(0.01)	0.01(0.01)	0.00(0.00)	0.00(0.00)	0.01(0.01)	0.00(0.00)	0.00(0.00)	0.01(0.03)	0.00(0.00)	0.01(0.02)	0.01(0.01)
TM6	0.00(0.00)	0.00(0.00)	0.00(0.00)	0.00(0.00)	0.01(0.01)	0.00(0.00)	0.00(0.00)	0.01(0.02)	0.00(0.00)	0.00(0.00)	0.00(0.00)	0.00(0.00)
TM7	0.00(0.00)	0.00(0.00)	0.00(0.00)	0.00(0.00)	0.00(0.00)	0.00(0.00)	0.00(0.00)	0.00(0.00)	0.00(0.00)	0.00(0.00)	0.00(0.00)	0.00(0.00)
TM8	0.00(0.00)	0.01(0.01)	0.00(0.00)	0.00(0.00)	0.00(0.00)	0.01(0.02)	0.00(0.00)	0.00(0.00)	0.01(0.02)	0.00(0.00)	0.01(0.01)	0.11(0.11)
TM9	0.00(0.00)	0.00(0.00)	0.12(0.15)	0.28(0.36)	0.01(0.03)	0.00(0.00)	0.00(0.00)	0.01(0.02)	0.34(0.37)	0.04(0.04)	0.01(0.01)	0.11(0.08)
TM10	0.00(0.00)	0.00(0.00)	0.05(0.09)	0.11(0.10)	0.00(0.00)	0.00(0.00)	0.00(0.00)	0.00(0.00)	0.04(0.04)	0.00(0.00)	0.00(0.01)	0.07(0.13)
TM11	0.00(0.01)	0.00(0.00)	0.01(0.02)	0.01(0.02)	0.01(0.02)	0.00(0.00)	0.00(0.00)	0.01(0.01)	0.01(0.01)	0.00(0.01)	0.00(0.00)	0.06(0.14)
TM12	0.00(0.00)	0.00(0.00)	0.20(0.17)	0.23(0.16)	0.01(0.01)	0.00(0.00)	0.00(0.00)	0.11(0.11)	0.11(0.08)	0.07(0.13)	0.06(0.14)	0.15(0.23)

Table A.5.: TM-TM contact frequencies (mean(SD)) for Avg non-palmitoylated.

TM	TM1	TM2	TM3	TM4	TM5	TM6	TM7	TM8	TM9	TM10	TM11	TM12
TM1	0.00(0.00)	0.00(0.00)	0.00(0.00)	0.00(0.00)	0.00(0.00)	0.00(0.00)	0.00(0.00)	0.00(0.00)	0.01(0.01)	0.00(0.00)	0.00(0.00)	0.00(0.00)
TM2	0.00(0.00)	0.00(0.00)	0.00(0.00)	0.00(0.00)	0.00(0.01)	0.00(0.00)	0.00(0.00)	0.00(0.00)	0.00(0.00)	0.00(0.00)	0.00(0.00)	0.00(0.00)
TM3	0.00(0.00)	0.00(0.00)	0.08(0.22)	0.16(0.19)	0.00(0.00)	0.00(0.00)	0.00(0.00)	0.02(0.05)	0.14(0.19)	0.05(0.09)	0.00(0.01)	0.21(0.17)
TM4	0.00(0.00)	0.00(0.00)	0.16(0.19)	0.22(0.23)	0.07(0.20)	0.01(0.02)	0.00(0.00)	0.07(0.20)	0.18(0.22)	0.14(0.18)	0.03(0.04)	0.20(0.19)
TM5	0.00(0.00)	0.00(0.01)	0.00(0.00)	0.07(0.20)	0.00(0.01)	0.00(0.01)	0.00(0.00)	0.00(0.00)	0.02(0.06)	0.00(0.00)	0.00(0.01)	0.01(0.02)
TM6	0.00(0.00)	0.00(0.00)	0.00(0.00)	0.01(0.02)	0.00(0.01)	0.00(0.00)	0.00(0.00)	0.00(0.00)	0.00(0.00)	0.00(0.00)	0.00(0.00)	0.00(0.00)
TM7	0.00(0.00)	0.00(0.00)	0.00(0.00)	0.00(0.00)	0.00(0.00)	0.00(0.00)	0.00(0.00)	0.00(0.00)	0.00(0.00)	0.00(0.00)	0.00(0.00)	0.00(0.00)
TM8	0.00(0.00)	0.00(0.00)	0.02(0.05)	0.07(0.20)	0.00(0.00)	0.00(0.00)	0.00(0.00)	0.00(0.00)	0.01(0.02)	0.00(0.00)	0.02(0.02)	0.16(0.12)
TM9	0.01(0.01)	0.00(0.00)	0.14(0.19)	0.18(0.22)	0.02(0.06)	0.00(0.00)	0.00(0.00)	0.01(0.02)	0.32(0.42)	0.02(0.03)	0.04(0.10)	0.12(0.09)
TM10	0.00(0.00)	0.00(0.00)	0.05(0.09)	0.14(0.18)	0.00(0.00)	0.00(0.00)	0.00(0.00)	0.00(0.00)	0.02(0.03)	0.00(0.00)	0.03(0.09)	0.13(0.23)
TM11	0.00(0.00)	0.00(0.00)	0.00(0.01)	0.03(0.04)	0.00(0.01)	0.00(0.00)	0.00(0.00)	0.02(0.02)	0.04(0.10)	0.03(0.09)	0.00(0.00)	0.08(0.15)
TM12	0.00(0.00)	0.00(0.00)	0.21(0.17)	0.20(0.19)	0.01(0.02)	0.00(0.00)	0.00(0.00)	0.16(0.12)	0.12(0.09)	0.13(0.23)	0.08(0.15)	0.21(0.33)

Table A.6.: TM-TM contact frequencies (mean(SD)) for Avg palmitoylated.

TM	TM1	TM2	TM3	TM4	TM5	TM6	TM7	TM8	TM9	TM10	TM11	TM12
TM1	0.00(0.00)	0.00(0.00)	0.00(0.00)	0.00(0.00)	0.00(0.00)	0.00(0.00)	0.00(0.00)	0.00(0.00)	0.00(0.00)	0.00(0.00)	0.00(0.00)	0.00(0.00)
TM2	0.00(0.00)	0.00(0.00)	0.00(0.00)	0.00(0.00)	0.00(0.00)	0.00(0.00)	0.00(0.00)	0.00(0.00)	0.00(0.00)	0.00(0.00)	0.00(0.00)	0.00(0.00)
TM3	0.00(0.00)	0.00(0.00)	0.02(0.02)	0.19(0.14)	0.04(0.06)	0.00(0.00)	0.00(0.00)	0.00(0.00)	0.21(0.22)	0.11(0.11)	0.08(0.07)	0.39(0.10)
TM4	0.00(0.00)	0.00(0.00)	0.19(0.14)	0.11(0.14)	0.00(0.00)	0.00(0.00)	0.00(0.00)	0.00(0.00)	0.20(0.17)	0.19(0.15)	0.03(0.03)	0.38(0.19)
TM5	0.00(0.00)	0.00(0.00)	0.04(0.06)	0.00(0.00)	0.00(0.00)	0.00(0.00)	0.00(0.00)	0.00(0.00)	0.00(0.00)	0.00(0.00)	0.01(0.01)	0.04(0.04)
TM6	0.00(0.00)	0.00(0.00)	0.00(0.00)	0.00(0.00)	0.00(0.00)	0.00(0.00)	0.00(0.00)	0.00(0.00)	0.00(0.00)	0.00(0.00)	0.00(0.00)	0.00(0.00)
TM7	0.00(0.00)	0.00(0.00)	0.00(0.00)	0.00(0.00)	0.00(0.00)	0.00(0.00)	0.00(0.00)	0.00(0.00)	0.00(0.00)	0.00(0.00)	0.00(0.00)	0.00(0.01)
TM8	0.00(0.00)	0.00(0.00)	0.00(0.00)	0.00(0.00)	0.00(0.00)	0.00(0.00)	0.00(0.00)	0.00(0.00)	0.02(0.03)	0.00(0.00)	0.07(0.06)	0.31(0.14)
TM9	0.00(0.00)	0.00(0.00)	0.21(0.22)	0.20(0.17)	0.00(0.00)	0.00(0.00)	0.00(0.00)	0.02(0.03)	0.32(0.33)	0.06(0.12)	0.01(0.01)	0.15(0.15)
TM10	0.00(0.00)	0.00(0.00)	0.11(0.11)	0.19(0.15)	0.00(0.00)	0.00(0.00)	0.00(0.00)	0.00(0.00)	0.06(0.12)	0.02(0.05)	0.01(0.01)	0.10(0.24)
TM11	0.00(0.00)	0.00(0.00)	0.08(0.07)	0.03(0.03)	0.01(0.01)	0.00(0.00)	0.00(0.00)	0.07(0.06)	0.01(0.01)	0.01(0.01)	0.00(0.00)	0.10(0.28)
TM12	0.00(0.00)	0.00(0.00)	0.39(0.10)	0.38(0.19)	0.04(0.04)	0.00(0.00)	0.00(0.01)	0.31(0.14)	0.15(0.15)	0.10(0.24)	0.10(0.28)	0.12(0.33)

Table A.7.: TM-TM contact frequencies (mean(SD)) for Avg (no interface-PI) non-palmitoylated.

TM	TM1	TM2	TM3	TM4	TM5	TM6	TM7	TM8	TM9	TM10	TM11	TM12
TM1	0.00(0.00)	0.00(0.00)	0.00(0.00)	0.05(0.09)	0.00(0.00)	0.00(0.00)	0.00(0.00)	0.00(0.00)	0.04(0.08)	0.00(0.00)	0.00(0.00)	0.00(0.00)
TM2	0.00(0.00)	0.00(0.00)	0.00(0.00)	0.00(0.00)	0.00(0.00)	0.00(0.00)	0.00(0.00)	0.01(0.01)	0.00(0.00)	0.00(0.00)	0.00(0.00)	0.00(0.00)
TM3	0.00(0.00)	0.00(0.00)	0.35(0.31)	0.17(0.12)	0.06(0.09)	0.00(0.00)	0.00(0.00)	0.16(0.12)	0.06(0.10)	0.04(0.07)	0.01(0.02)	0.10(0.16)
TM4	0.05(0.09)	0.00(0.00)	0.17(0.12)	0.41(0.27)	0.43(0.31)	0.00(0.00)	0.01(0.02)	0.36(0.27)	0.11(0.19)	0.06(0.12)	0.01(0.01)	0.09(0.14)
TM5	0.00(0.00)	0.00(0.00)	0.06(0.09)	0.43(0.31)	0.09(0.08)	0.00(0.00)	0.00(0.00)	0.01(0.01)	0.12(0.09)	0.00(0.01)	0.01(0.02)	0.02(0.04)
TM6	0.00(0.00)	0.00(0.00)	0.00(0.00)	0.00(0.00)	0.00(0.00)	0.00(0.00)	0.00(0.00)	0.00(0.01)	0.00(0.00)	0.00(0.00)	0.00(0.00)	0.00(0.00)
TM7	0.00(0.00)	0.00(0.00)	0.00(0.00)	0.01(0.02)	0.00(0.00)	0.00(0.00)	0.00(0.00)	0.00(0.00)	0.02(0.04)	0.00(0.00)	0.00(0.00)	0.00(0.00)
TM8	0.00(0.00)	0.01(0.01)	0.16(0.12)	0.36(0.27)	0.01(0.01)	0.00(0.01)	0.00(0.00)	0.08(0.15)	0.04(0.07)	0.01(0.01)	0.01(0.01)	0.07(0.13)
TM9	0.04(0.08)	0.00(0.00)	0.06(0.10)	0.11(0.19)	0.12(0.09)	0.00(0.00)	0.02(0.04)	0.04(0.07)	0.15(0.23)	0.00(0.00)	0.00(0.00)	0.03(0.04)
TM10	0.00(0.00)	0.00(0.00)	0.04(0.07)	0.06(0.12)	0.00(0.01)	0.00(0.00)	0.00(0.00)	0.01(0.01)	0.00(0.00)	0.00(0.00)	0.00(0.00)	0.00(0.01)
TM11	0.00(0.00)	0.00(0.00)	0.01(0.02)	0.01(0.01)	0.01(0.02)	0.00(0.00)	0.00(0.00)	0.01(0.01)	0.00(0.00)	0.00(0.00)	0.00(0.00)	0.00(0.01)
TM12	0.00(0.00)	0.00(0.00)	0.10(0.16)	0.09(0.14)	0.02(0.04)	0.00(0.00)	0.00(0.00)	0.07(0.13)	0.03(0.04)	0.00(0.01)	0.00(0.01)	0.01(0.02)

Table A.8.: TM-TM contact frequencies (mean(SD)) for Avg (no interface-PI) palmitoylated.

TM	TM1	TM2	TM3	TM4	TM5	TM6	TM7	TM8	TM9	TM10	TM11	TM12
TM1	0.00(0.00)	0.00(0.00)	0.00(0.00)	0.00(0.00)	0.00(0.00)	0.00(0.00)	0.00(0.00)	0.00(0.00)	0.00(0.00)	0.00(0.00)	0.00(0.00)	0.00(0.00)
TM2	0.00(0.00)	0.00(0.00)	0.00(0.00)	0.00(0.00)	0.00(0.00)	0.00(0.00)	0.00(0.00)	0.00(0.01)	0.00(0.00)	0.00(0.00)	0.00(0.00)	0.00(0.00)
TM3	0.00(0.00)	0.00(0.00)	0.04(0.03)	0.25(0.12)	0.05(0.06)	0.00(0.00)	0.00(0.00)	0.00(0.01)	0.20(0.20)	0.14(0.10)	0.09(0.07)	0.43(0.06)
TM4	0.00(0.00)	0.00(0.00)	0.25(0.12)	0.15(0.12)	0.01(0.03)	0.00(0.00)	0.00(0.00)	0.01(0.03)	0.28(0.15)	0.25(0.13)	0.03(0.03)	0.42(0.06)
TM5	0.00(0.00)	0.00(0.00)	0.05(0.06)	0.01(0.03)	0.00(0.01)	0.00(0.00)	0.00(0.00)	0.00(0.00)	0.00(0.00)	0.00(0.00)	0.00(0.01)	0.04(0.04)
TM6	0.00(0.00)	0.00(0.00)	0.00(0.00)	0.00(0.00)	0.00(0.00)	0.00(0.00)	0.00(0.00)	0.00(0.00)	0.00(0.00)	0.00(0.00)	0.00(0.00)	0.00(0.00)
TM7	0.00(0.00)	0.00(0.00)	0.00(0.00)	0.00(0.00)	0.00(0.00)	0.00(0.00)	0.00(0.00)	0.00(0.00)	0.00(0.00)	0.00(0.00)	0.00(0.00)	0.00(0.00)
TM8	0.00(0.00)	0.00(0.01)	0.00(0.01)	0.01(0.03)	0.00(0.00)	0.00(0.00)	0.00(0.00)	0.00(0.00)	0.01(0.01)	0.00(0.00)	0.08(0.05)	0.35(0.06)
TM9	0.00(0.00)	0.00(0.00)	0.20(0.20)	0.28(0.15)	0.00(0.00)	0.00(0.00)	0.00(0.00)	0.01(0.01)	0.35(0.34)	0.01(0.01)	0.00(0.00)	0.10(0.04)
TM10	0.00(0.00)	0.00(0.00)	0.14(0.10)	0.25(0.13)	0.00(0.00)	0.00(0.00)	0.00(0.00)	0.00(0.00)	0.01(0.01)	0.00(0.00)	0.00(0.00)	0.00(0.01)
TM11	0.00(0.00)	0.00(0.00)	0.09(0.07)	0.03(0.03)	0.00(0.01)	0.00(0.00)	0.00(0.00)	0.08(0.05)	0.00(0.00)	0.00(0.00)	0.00(0.00)	0.00(0.00)
TM12	0.00(0.00)	0.00(0.00)	0.43(0.06)	0.42(0.06)	0.04(0.04)	0.00(0.00)	0.00(0.00)	0.35(0.06)	0.10(0.04)	0.00(0.01)	0.00(0.00)	0.00(0.00)

Table A.9.: TM-TM contact frequencies (mean(SD)) for Neuron non-palmitoylated.

TM	TM1	TM2	TM3	TM4	TM5	TM6	TM7	TM8	TM9	TM10	TM11	TM12
TM1	0.00(0.00)	0.00(0.00)	0.00(0.00)	0.00(0.01)	0.00(0.00)	0.00(0.00)	0.00(0.00)	0.00(0.00)	0.00(0.00)	0.00(0.00)	0.00(0.00)	0.00(0.00)
TM2	0.00(0.00)	0.00(0.00)	0.00(0.00)	0.00(0.00)	0.00(0.00)	0.00(0.00)	0.00(0.00)	0.00(0.00)	0.00(0.00)	0.00(0.00)	0.00(0.00)	0.00(0.00)
TM3	0.00(0.00)	0.00(0.00)	0.01(0.01)	0.13(0.11)	0.01(0.01)	0.00(0.00)	0.00(0.00)	0.01(0.01)	0.15(0.15)	0.12(0.13)	0.10(0.17)	0.39(0.10)
TM4	0.00(0.01)	0.00(0.00)	0.13(0.11)	0.17(0.23)	0.01(0.02)	0.00(0.00)	0.00(0.01)	0.01(0.02)	0.26(0.20)	0.20(0.16)	0.01(0.01)	0.41(0.17)
TM5	0.00(0.00)	0.00(0.00)	0.01(0.01)	0.01(0.02)	0.00(0.01)	0.00(0.00)	0.00(0.00)	0.00(0.00)	0.00(0.01)	0.00(0.00)	0.00(0.01)	0.06(0.06)
TM6	0.00(0.00)	0.00(0.00)	0.00(0.00)	0.00(0.00)	0.00(0.00)	0.00(0.00)	0.00(0.00)	0.00(0.00)	0.00(0.00)	0.00(0.00)	0.00(0.00)	0.00(0.00)
TM7	0.00(0.00)	0.00(0.00)	0.00(0.00)	0.00(0.01)	0.00(0.00)	0.00(0.00)	0.00(0.00)	0.00(0.00)	0.00(0.00)	0.00(0.00)	0.00(0.00)	0.00(0.00)
TM8	0.00(0.00)	0.00(0.00)	0.01(0.01)	0.01(0.02)	0.00(0.00)	0.00(0.00)	0.00(0.00)	0.00(0.01)	0.00(0.01)	0.00(0.01)	0.13(0.14)	0.29(0.13)
TM9	0.00(0.00)	0.00(0.00)	0.15(0.15)	0.26(0.20)	0.00(0.01)	0.00(0.00)	0.00(0.00)	0.00(0.01)	0.34(0.30)	0.05(0.07)	0.00(0.00)	0.20(0.15)
TM10	0.00(0.00)	0.00(0.00)	0.12(0.13)	0.20(0.16)	0.00(0.00)	0.00(0.00)	0.00(0.00)	0.00(0.01)	0.05(0.07)	0.00(0.00)	0.00(0.00)	0.01(0.03)
TM11	0.00(0.00)	0.00(0.00)	0.10(0.17)	0.01(0.01)	0.00(0.01)	0.00(0.00)	0.00(0.00)	0.13(0.14)	0.00(0.00)	0.00(0.00)	0.00(0.00)	0.00(0.00)
TM12	0.00(0.00)	0.00(0.00)	0.39(0.10)	0.41(0.17)	0.06(0.06)	0.00(0.00)	0.00(0.00)	0.29(0.13)	0.20(0.15)	0.01(0.03)	0.00(0.00)	0.01(0.02)

Table A.10.: TM-TM contact frequencies (mean(SD)) for Neuron palmitoylated.

TM	TM1	TM2	TM3	TM4	TM5	TM6	TM7	TM8	TM9	TM10	TM11	TM12
TM1	0.00(0.00)	0.00(0.00)	0.00(0.00)	0.00(0.00)	0.00(0.00)	0.00(0.00)	0.00(0.00)	0.00(0.00)	0.00(0.00)	0.00(0.00)	0.00(0.00)	0.00(0.00)
TM2	0.00(0.00)	0.00(0.00)	0.00(0.00)	0.00(0.00)	0.00(0.00)	0.00(0.00)	0.00(0.00)	0.00(0.00)	0.00(0.00)	0.00(0.00)	0.00(0.00)	0.00(0.00)
TM3	0.00(0.00)	0.00(0.00)	0.01(0.01)	0.22(0.06)	0.01(0.01)	0.00(0.00)	0.00(0.00)	0.00(0.00)	0.11(0.14)	0.10(0.06)	0.17(0.07)	0.46(0.02)
TM4	0.00(0.00)	0.00(0.00)	0.22(0.06)	0.01(0.01)	0.00(0.00)	0.00(0.00)	0.00(0.00)	0.00(0.00)	0.22(0.06)	0.23(0.06)	0.04(0.05)	0.51(0.05)
TM5	0.00(0.00)	0.00(0.00)	0.01(0.01)	0.00(0.00)	0.00(0.00)	0.00(0.00)	0.00(0.00)	0.00(0.00)	0.00(0.00)	0.00(0.00)	0.00(0.00)	0.03(0.02)
TM6	0.00(0.00)	0.00(0.00)	0.00(0.00)	0.00(0.00)	0.00(0.00)	0.00(0.00)	0.00(0.00)	0.00(0.00)	0.00(0.00)	0.00(0.00)	0.00(0.00)	0.00(0.00)
TM7	0.00(0.00)	0.00(0.00)	0.00(0.00)	0.00(0.00)	0.00(0.00)	0.00(0.00)	0.00(0.00)	0.00(0.00)	0.00(0.00)	0.00(0.00)	0.00(0.00)	0.00(0.00)
TM8	0.00(0.00)	0.00(0.00)	0.00(0.00)	0.00(0.00)	0.00(0.00)	0.00(0.00)	0.00(0.00)	0.00(0.00)	0.00(0.01)	0.00(0.00)	0.13(0.06)	0.35(0.08)
TM9	0.00(0.00)	0.00(0.00)	0.11(0.14)	0.22(0.06)	0.00(0.00)	0.00(0.00)	0.00(0.00)	0.00(0.01)	0.21(0.17)	0.06(0.08)	0.00(0.00)	0.22(0.14)
TM10	0.00(0.00)	0.00(0.00)	0.10(0.06)	0.23(0.06)	0.00(0.00)	0.00(0.00)	0.00(0.00)	0.00(0.00)	0.06(0.08)	0.01(0.02)	0.00(0.00)	0.02(0.03)
TM11	0.00(0.00)	0.00(0.00)	0.17(0.07)	0.04(0.05)	0.00(0.00)	0.00(0.00)	0.00(0.00)	0.13(0.06)	0.00(0.00)	0.00(0.00)	0.00(0.00)	0.00(0.00)
TM12	0.00(0.00)	0.00(0.00)	0.46(0.02)	0.51(0.05)	0.03(0.02)	0.00(0.00)	0.00(0.00)	0.35(0.08)	0.22(0.14)	0.02(0.03)	0.00(0.00)	0.01(0.03)

Table A.11.: TM-TM contact frequencies (mean(SD)) for Avg (DAT) non-palmitoylated.

TM	TM1	TM2	TM3	TM4	TM5	TM6	TM7	TM8	TM9	TM10	TM11	TM12
TM1	0.00(0.00)	0.00(0.00)	0.00(0.00)	0.00(0.00)	0.00(0.00)	0.00(0.00)	0.00(0.00)	0.00(0.00)	0.00(0.00)	0.00(0.00)	0.00(0.00)	0.00(0.00)
TM2	0.00(0.00)	0.00(0.00)	0.00(0.00)	0.00(0.00)	0.00(0.00)	0.00(0.00)	0.00(0.00)	0.00(0.00)	0.00(0.00)	0.00(0.00)	0.00(0.00)	0.00(0.00)
TM3	0.00(0.00)	0.00(0.00)	0.00(0.00)	0.33(0.05)	0.00(0.00)	0.00(0.00)	0.00(0.00)	0.00(0.00)	0.16(0.08)	0.00(0.00)	0.00(0.00)	0.35(0.08)
TM4	0.00(0.00)	0.00(0.00)	0.33(0.05)	0.18(0.12)	0.00(0.00)	0.00(0.00)	0.00(0.00)	0.00(0.00)	0.47(0.05)	0.45(0.02)	0.01(0.01)	0.56(0.08)
TM5	0.00(0.00)	0.00(0.00)	0.00(0.00)	0.00(0.00)	0.00(0.00)	0.00(0.00)	0.00(0.00)	0.00(0.00)	0.00(0.00)	0.00(0.00)	0.00(0.00)	0.03(0.03)
TM6	0.00(0.00)	0.00(0.00)	0.00(0.00)	0.00(0.00)	0.00(0.00)	0.00(0.00)	0.00(0.00)	0.00(0.00)	0.00(0.00)	0.00(0.00)	0.00(0.00)	0.00(0.00)
TM7	0.00(0.00)	0.00(0.00)	0.00(0.00)	0.00(0.00)	0.00(0.00)	0.00(0.00)	0.00(0.00)	0.00(0.00)	0.00(0.00)	0.00(0.00)	0.00(0.00)	0.00(0.00)
TM8	0.00(0.00)	0.00(0.00)	0.00(0.00)	0.00(0.00)	0.00(0.00)	0.00(0.00)	0.00(0.00)	0.00(0.00)	0.00(0.00)	0.00(0.00)	0.00(0.00)	0.14(0.07)
TM9	0.00(0.00)	0.00(0.00)	0.16(0.08)	0.47(0.05)	0.00(0.00)	0.00(0.00)	0.00(0.00)	0.00(0.00)	0.35(0.17)	0.01(0.01)	0.00(0.00)	0.48(0.04)
TM10	0.00(0.00)	0.00(0.00)	0.00(0.00)	0.45(0.02)	0.00(0.00)	0.00(0.00)	0.00(0.00)	0.00(0.00)	0.01(0.01)	0.00(0.00)	0.00(0.00)	0.00(0.00)
TM11	0.00(0.00)	0.00(0.00)	0.00(0.00)	0.01(0.01)	0.00(0.00)	0.00(0.00)	0.00(0.00)	0.00(0.00)	0.00(0.00)	0.00(0.00)	0.00(0.00)	0.00(0.00)
TM12	0.00(0.00)	0.00(0.00)	0.35(0.08)	0.56(0.08)	0.03(0.03)	0.00(0.00)	0.00(0.00)	0.14(0.07)	0.48(0.04)	0.00(0.00)	0.00(0.00)	0.02(0.02)

Table A.12.: TM-TM contact frequencies (mean(SD)) for Avg (DAT) palmitoylated.

TM	TM1	TM2	TM3	TM4	TM5	TM6	TM7	TM8	TM9	TM10	TM11	TM12
TM1	0.00(0.00)	0.00(0.00)	0.00(0.00)	0.00(0.00)	0.00(0.00)	0.00(0.00)	0.00(0.00)	0.00(0.00)	0.00(0.00)	0.00(0.00)	0.00(0.00)	0.02(0.05)
TM2	0.00(0.00)	0.00(0.00)	0.00(0.00)	0.00(0.00)	0.00(0.00)	0.00(0.00)	0.00(0.00)	0.00(0.00)	0.00(0.00)	0.00(0.00)	0.00(0.00)	0.00(0.00)
TM3	0.00(0.00)	0.00(0.00)	0.00(0.00)	0.30(0.18)	0.00(0.01)	0.00(0.00)	0.00(0.00)	0.00(0.00)	0.22(0.15)	0.00(0.00)	0.00(0.00)	0.32(0.17)
TM4	0.00(0.00)	0.00(0.00)	0.30(0.18)	0.37(0.29)	0.00(0.00)	0.00(0.00)	0.00(0.00)	0.00(0.00)	0.33(0.20)	0.33(0.20)	0.01(0.01)	0.41(0.18)
TM5	0.00(0.00)	0.00(0.00)	0.00(0.01)	0.00(0.00)	0.00(0.00)	0.00(0.00)	0.00(0.00)	0.00(0.00)	0.00(0.00)	0.00(0.00)	0.01(0.02)	0.07(0.13)
TM6	0.00(0.00)	0.00(0.00)	0.00(0.00)	0.00(0.00)	0.00(0.00)	0.00(0.00)	0.00(0.00)	0.00(0.00)	0.00(0.00)	0.00(0.00)	0.00(0.00)	0.00(0.00)
TM7	0.00(0.00)	0.00(0.00)	0.00(0.00)	0.00(0.00)	0.00(0.00)	0.00(0.00)	0.00(0.00)	0.00(0.00)	0.00(0.00)	0.00(0.00)	0.00(0.00)	0.00(0.00)
TM8	0.00(0.00)	0.00(0.00)	0.00(0.00)	0.00(0.00)	0.00(0.00)	0.00(0.00)	0.00(0.00)	0.00(0.00)	0.01(0.01)	0.00(0.00)	0.00(0.00)	0.18(0.14)
TM9	0.00(0.00)	0.00(0.00)	0.22(0.15)	0.33(0.20)	0.00(0.00)	0.00(0.00)	0.00(0.00)	0.01(0.01)	0.46(0.32)	0.01(0.02)	0.00(0.01)	0.29(0.15)
TM10	0.00(0.00)	0.00(0.00)	0.00(0.00)	0.33(0.20)	0.00(0.00)	0.00(0.00)	0.00(0.00)	0.00(0.00)	0.01(0.02)	0.00(0.00)	0.00(0.00)	0.09(0.26)
TM11	0.00(0.00)	0.00(0.00)	0.00(0.00)	0.01(0.01)	0.01(0.02)	0.00(0.00)	0.00(0.00)	0.00(0.00)	0.00(0.01)	0.00(0.00)	0.00(0.00)	0.06(0.16)
TM12	0.02(0.05)	0.00(0.00)	0.32(0.17)	0.41(0.18)	0.07(0.13)	0.00(0.00)	0.00(0.00)	0.18(0.14)	0.29(0.15)	0.09(0.26)	0.06(0.16)	0.14(0.33)

A.5. Welch test: test statistics

Table A.13.: Welch test results per system (sorted by p). t and p are rounded to 3 decimals, and interfaces with $t > 0$ are reported.

Simp			Avg			Avg (no interface PI)			Neuron			Avg (DAT)		
Interface	t	p	Interface	t	p	Interface	t	p	Interface	t	p	Interface	t	p
TM10-TM10	-2.088	0.075	TM3-TM12	-2.540	0.027	TM4-TM12	-6.417	0.000	TM3-TM12	-2.024	0.080	TM9-TM12	3.604	0.007
TM2-TM3	-1.528	0.170	TM3-TM11	-2.762	0.028	TM8-TM12	-5.788	0.000	TM3-TM4	-1.923	0.082	TM8-TM9	-2.203	0.062
TM2-TM4	1.482	0.182	TM8-TM12	-2.310	0.037	TM3-TM12	-5.519	0.000	TM4-TM4	1.971	0.089	TM4-TM12	2.038	0.069
TM5-TM6	-1.345	0.220	TM8-TM11	-2.180	0.058	TM5-TM9	3.877	0.006	TM9-TM11	-1.964	0.090	TM4-TM9	1.879	0.098
TM4-TM6	1.314	0.230	TM4-TM12	-1.950	0.071	TM4-TM5	3.811	0.006	TM4-TM11	-1.946	0.091	TM4-TM11	1.737	0.107
TM2-TM5	-1.289	0.238	TM3-TM5	-1.909	0.097	TM4-TM8	3.693	0.007	TM8-TM10	1.763	0.121	TM4-TM4	-1.687	0.125
TM7-TM8	-1.245	0.253	TM6-TM8	1.603	0.151	TM3-TM8	3.700	0.008	TM4-TM12	-1.631	0.141	TM3-TM3	-1.708	0.131
TM3-TM11	-1.211	0.263	TM2-TM8	1.393	0.205	TM8-TM11	-3.463	0.009	TM5-TM12	1.617	0.143	TM4-TM10	1.620	0.148
TM2-TM8	-1.172	0.278	TM5-TM12	-1.319	0.217	TM4-TM10	-3.008	0.009	TM10-TM10	-1.482	0.181	TM3-TM5	-1.589	0.156
TM9-TM12	1.115	0.284	TM5-TM6	1.318	0.228	TM3-TM11	-3.334	0.010	TM11-TM12	-1.329	0.225	TM4-TM8	-1.431	0.196
TM5-TM7	-1.158	0.285	TM4-TM4	1.191	0.257	TM9-TM12	-2.805	0.014	TM5-TM11	1.262	0.242	TM3-TM10	-1.148	0.289
TM8-TM11	-1.137	0.285	TM2-TM4	1.189	0.266	TM5-TM5	2.992	0.020	TM8-TM12	-1.172	0.264	TM8-TM11	-1.125	0.298
TM2-TM9	1.113	0.303	TM3-TM10	-1.138	0.275	TM3-TM3	2.794	0.026	TM3-TM11	-1.175	0.269	TM3-TM9	-1.026	0.328
TM3-TM3	1.086	0.313	TM2-TM2	-1.136	0.293	TM3-TM10	-2.384	0.034	TM9-TM9	1.078	0.304	TM12-TM12	-1.012	0.345
TM4-TM8	1.063	0.323	TM7-TM11	-1.039	0.327	TM4-TM4	2.468	0.034	TM5-TM7	1.000	0.351	TM8-TM10	-1.000	0.351
TM6-TM9	1.031	0.337	TM10-TM10	-1.034	0.335	TM4-TM11	-2.561	0.034	TM5-TM8	1.000	0.351	TM6-TM12	-1.000	0.351
TM1-TM11	-1.020	0.342	TM2-TM5	1.024	0.340	TM9-TM10	-2.575	0.036	TM5-TM9	1.000	0.351	TM11-TM12	-1.000	0.351
TM6-TM12	1.005	0.348	TM4-TM6	1.014	0.344	TM4-TM9	-1.891	0.081	TM7-TM11	1.000	0.351	TM3-TM11	-1.000	0.351
TM2-TM12	1.000	0.351	TM5-TM9	1.000	0.351	TM5-TM8	1.852	0.106	TM7-TM9	1.000	0.351	TM5-TM10	-1.000	0.351
TM6-TM7	-1.000	0.351	TM4-TM5	1.000	0.351	TM3-TM9	-1.718	0.116	TM4-TM5	1.000	0.351	TM7-TM12	-1.000	0.351
TM7-TM7	-1.000	0.351	TM4-TM7	1.000	0.351	TM1-TM4	1.729	0.127	TM1-TM5	1.000	0.351	TM10-TM11	-1.000	0.351
TM5-TM10	-1.000	0.351	TM5-TM7	1.000	0.351	TM4-TM7	1.645	0.144	TM1-TM4	1.000	0.351	TM4-TM6	-1.000	0.351
TM6-TM10	1.000	0.351	TM6-TM9	1.000	0.351	TM8-TM8	1.599	0.154	TM7-TM12	1.000	0.351	TM11-TM11	-1.000	0.351
TM4-TM7	-1.000	0.351	TM3-TM7	1.000	0.351	TM5-TM6	1.560	0.161	TM3-TM8	1.000	0.351	TM5-TM11	-1.000	0.351
TM3-TM8	1.000	0.351	TM1-TM9	1.000	0.351	TM2-TM5	1.530	0.169	TM1-TM9	1.000	0.351	TM5-TM9	-1.000	0.351
TM1-TM9	1.000	0.351	TM1-TM4	1.000	0.351	TM1-TM9	1.531	0.170	TM3-TM7	1.000	0.351	TM1-TM12	-1.000	0.351
TM2-TM7	-1.000	0.351	TM2-TM7	-1.000	0.351	TM9-TM9	-1.373	0.194	TM8-TM8	1.000	0.351	TM7-TM11	-1.000	0.351
TM1-TM4	1.000	0.351	TM1-TM3	-1.000	0.351	TM8-TM9	1.332	0.223	TM5-TM5	1.000	0.351	TM9-TM11	-0.998	0.351
TM5-TM11	-0.995	0.351	TM1-TM12	-1.000	0.351	TM12-TM12	1.318	0.228	TM4-TM7	1.000	0.351	TM10-TM12	-0.982	0.359
TM4-TM5	0.989	0.356	TM7-TM9	1.000	0.351	TM7-TM12	1.297	0.233	TM4-TM8	0.993	0.354	TM5-TM12	-0.921	0.386
TM6-TM8	-0.966	0.365	TM7-TM7	1.000	0.351	TM5-TM7	1.256	0.249	TM5-TM10	0.891	0.400	TM9-TM9	-0.873	0.401
TM9-TM11	0.923	0.377	TM7-TM8	1.000	0.351	TM3-TM4	-1.149	0.270	TM4-TM10	-0.573	0.581	TM8-TM12	-0.747	0.472
TM5-TM5	0.929	0.383	TM5-TM8	-1.000	0.351	TM8-TM10	1.172	0.279	TM4-TM9	0.530	0.610	TM3-TM12	0.471	0.648
TM7-TM12	-0.749	0.477	TM3-TM8	0.999	0.351	TM10-TM10	-1.171	0.280	TM10-TM12	-0.506	0.621	TM3-TM4	0.441	0.670
TM8-TM8	-0.747	0.478	TM4-TM8	0.994	0.353	TM5-TM12	-1.123	0.280	TM3-TM9	0.491	0.631	TM9-TM10	0.351	0.731
TM3-TM6	-0.608	0.558	TM5-TM10	-0.980	0.360	TM5-TM10	1.153	0.281	TM3-TM10	0.339	0.742			
TM11-TM12	-0.566	0.585	TM5-TM5	0.948	0.374	TM7-TM9	1.144	0.290	TM9-TM10	-0.322	0.752			
TM4-TM11	-0.533	0.607	TM7-TM12	-0.929	0.384	TM1-TM3	1.101	0.307	TM3-TM3	-0.202	0.843			
TM10-TM12	-0.513	0.617	TM9-TM11	0.918	0.388	TM3-TM7	1.071	0.319	TM9-TM12	-0.179	0.860			
TM8-TM10	0.466	0.652	TM2-TM3	-0.868	0.413	TM1-TM5	1.020	0.341	TM8-TM9	-0.174	0.864			
TM8-TM9	-0.463	0.654	TM1-TM11	0.834	0.425	TM11-TM12	1.003	0.349	TM12-TM12	-0.150	0.883			
TM9-TM10	-0.425	0.677	TM10-TM11	0.816	0.440	TM6-TM7	1.000	0.351	TM3-TM5	0.027	0.979			
TM4-TM9	-0.418	0.683	TM3-TM3	0.816	0.441	TM2-TM7	1.000	0.351	TM8-TM11	-0.023	0.982			
TM8-TM12	-0.385	0.706	TM9-TM10	-0.730	0.486	TM2-TM9	1.000	0.351						
TM5-TM8	-0.385	0.707	TM3-TM9	-0.704	0.493	TM7-TM7	1.000	0.351						
TM11-TM11	-0.370	0.719	TM3-TM6	0.651	0.531	TM6-TM6	-1.000	0.351						
TM4-TM12	0.348	0.733	TM4-TM10	-0.619	0.546	TM11-TM11	-1.000	0.351						
TM5-TM9	0.329	0.748	TM5-TM11	-0.623	0.549	TM7-TM8	0.970	0.363						
TM5-TM12	0.328	0.748	TM12-TM12	0.546	0.593	TM1-TM12	0.896	0.400						
TM3-TM4	0.298	0.770	TM8-TM9	-0.542	0.597	TM6-TM9	0.877	0.401						
TM3-TM12	-0.283	0.782	TM8-TM8	-0.529	0.609	TM2-TM4	0.889	0.401						
TM4-TM10	0.264	0.796	TM9-TM12	-0.474	0.645	TM2-TM3	0.796	0.447						
TM12-TM12	-0.230	0.821	TM3-TM4	-0.393	0.701	TM7-TM11	-0.709	0.499						
TM4-TM4	0.213	0.835	TM10-TM12	0.328	0.748	TM3-TM6	0.699	0.501						
TM3-TM10	-0.183	0.858	TM8-TM10	-0.289	0.778	TM2-TM12	-0.702	0.503						
TM3-TM9	-0.152	0.882	TM6-TM7	-0.266	0.796	TM1-TM11	0.667	0.523						
TM9-TM9	0.102	0.920	TM11-TM11	-0.197	0.847	TM6-TM12	-0.661	0.523						
TM10-TM11	0.067	0.947	TM4-TM11	0.188	0.854	TM6-TM8	0.637	0.541						
TM3-TM5	-0.036	0.972	TM11-TM12	-0.188	0.854	TM2-TM8	0.590	0.569						
			TM4-TM9	-0.172	0.866	TM5-TM11	0.573	0.582						
			TM9-TM9	0.021	0.984	TM9-TM11	-0.345	0.737						
						TM10-TM12	0.324	0.752						
						TM3-TM5	0.179	0.861						
						TM4-TM6	-0.069	0.946						

A.6. Cholesterol Densmap

Note that, in this representation every density map is normalised to 1 within each system, due to the significant differences in cholesterol concentration for each distinct membrane composition.

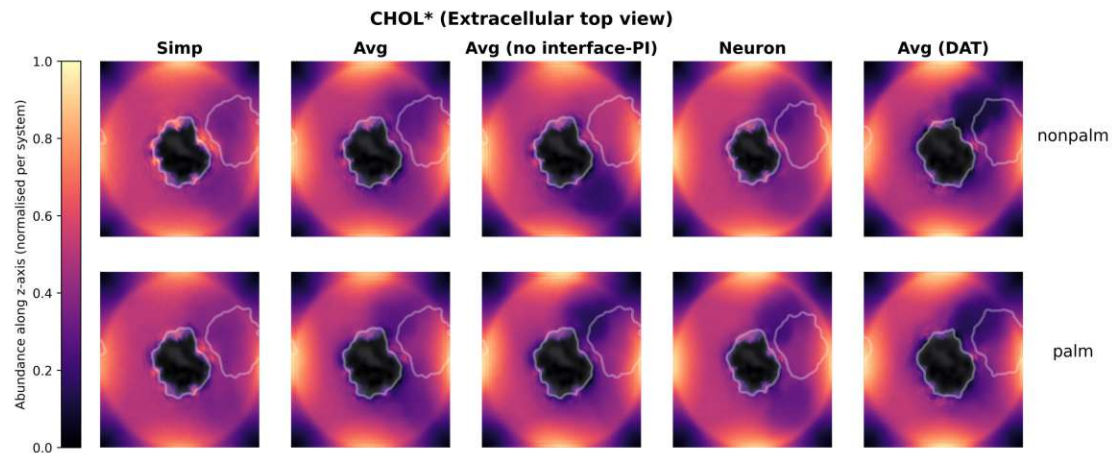


Figure A.5.: Density map of cholesterol molecules in the x - y plane (extracellular top view) for each system, averaged over all repeats. The signal reflects the per-frame-averaged occupancy (bead counts per bin) over time, normalized for every system. The initial cryo-EM configuration is shown as a gray outline. Note that the Neuron systems appear smaller due to the larger simulation box size.

A.7. Lipid Contacts: Simp system

The figures show the scaled lipid headgroup contacts at the palmitoylation site shown as violin plots across replicas for the Simp system (nonpalm and palm). Points indicate the time-averaged, concentration-scaled value per replica as described in 3. Contact cutoff: < 1.2 nm.

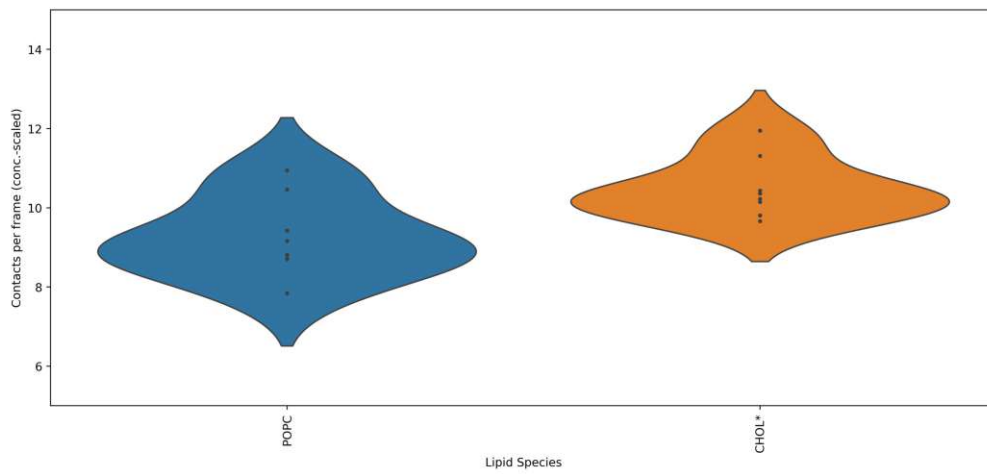


Figure A.6.: Simp nonpalm

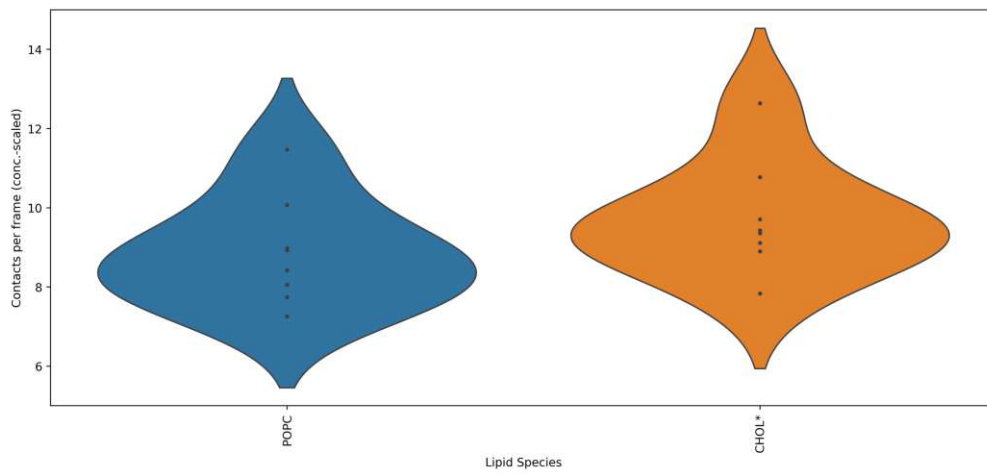


Figure A.7.: Simp palm